UNIVERSITATEA VALAHIA DIN TÂRGOVIȘTE
SAPIENTIA ET VIRTUS
1992

sciendo

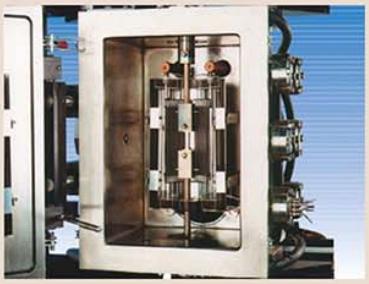

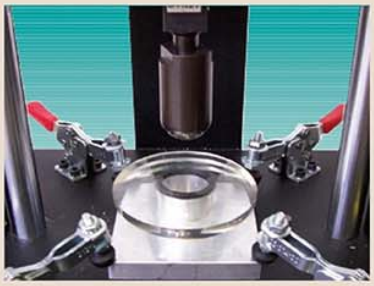

# The Scientific Bulletin of Valahia University MATERIALS and MECHANICS

2019

Vol. 17 No. 16

The Scientific Bulletin of VALAHIA University
MATERIALS and MECHANICS –Vol. 17, No. 16

DOI 10.2478/bsmm-2019-0001

# STUDIES OF ELEMENTAL ANALYSIS AND STRUCTURE ON IMPLANTABLE METAL ALLOYS

**Florina Violeta ANGHELINA, Veronica DESPA*, Carmen POPA, Constantin C. ANGHELINA**

Valahia University of Targoviste, Faculty of Materials Engineering and Mechanics,
13 Aleea Sinaia Street, Targoviste, Romania

E-mail: * dumiver@yahoo.com

**Abstract:** *It is obvious that all the elements in a metallic prosthesis implanted in the human body may have beneficial or detrimental effects on the tissue-prosthesis interference. For this reason, the precise knowledge of the chemical composition and structure of an implantable metallic material becomes a major requirement for estimating the medical prosthesis behavior and minimizing the risk of rejection of the implant by the human body. This paper presents an elemental and structural analysis of some potentially biocompatible materials, such as AISI 316 and Co-Cr-Mo alloys.*

**Keywords:** *AISI 316 alloys, Co-Cr-Mo alloys, the surface roughness, SEM electronic microscopy*

## 1. INTRODUCTION

The Co-Cr-Mo alloy is one of the most used implant alloys for artificial joints and offers a good combination of mechanical properties, corrosion resistance and biocompatibility. There are several types of Co-Cr-Mo materials used in the present. Each material has a different microstructure, as well as different optimized properties for a specific design or function. Stainless steels are a class of metallic materials that mostly have the properties required for materials that are used in the human body: chemical, thermal and mechanical stability, biocompatibility.

Martensitic and ferro-martensitic stainless steels are characterized by a proportion of the chromium and carbon content, so when the steel heats over the transformation temperature, its structure becomes austenitic, which turns to martensite cooling. In order to increase their resistance to hot oxidation, silicon is added, and they are alloyed with 2 ÷ 4% Ni to increase the tenacity. They are used in a recited and evolving state, not in a recoverable state. The martensitic stainless steels are strongly magnetic and can be hardened by heat treatment. Special heat treatment procedures must ensure a good balance between hardness and breakage properties. High hardness provides good wear resistance and sharp edges keep sharp. These alloys retain their mechanical properties and can be used for chisels, pliers, scissors, drills.

Ferrite stainless steels are characterized by an average content of 0.1 ÷ 0.35% C and 15 ÷ 30% Cr.

These are single-phase steels and therefore do not suffer structural changes in heating and cooling. At certain concentrations of carbon and chromium, some martensitic structural transformations may occur. These steels have a corrosion resistance superior to martensitic ones and a lower cost of austenitic.

Ferro-austenitic stainless steels constitute an intermediate family between ferrite and austenitic steels.

Austenitic-ferrite stainless steels are characterized by a content of: C ~ 0.05%, 8% Ni and 20-22% Cr. They have a very good resistance both to corrosion and high temperatures. By molybdenum alloying of these steels (1.5% Mo), good mechanical properties are obtained. Their structure is determined by the equilibrium between alpha elements (Cr, Mo, W, Si, Al, Ti, Nb) and gamma elements (C, Ni, Cu, Mn, N). Depending on the equivalents in Cr and Ni, the austenitic-ferrite domain separates the austenitic domain. At 12% nickel equivalent ($E_{Ni}$) and chromium equivalent ($E_{Cr}$) values of 19%, an austenitic-ferritic structure is obtained, so adjusting the content in alpha- and gamma-elements produces mixed austenite and ferrite structures. These structures present hot processing difficulties, many of which have a sensitivity to intergranular corrosion. Their properties can be modified by structural hardening.

Austenitic stainless steels are characterized by a low carbon content (C <0.1%), a content of 12 ÷ 25% Cr and 8 ÷ 30% Ni, having a certain proportion of alpha and gamma equivalents and a stability of austeniticity to very low temperatures. These steels have excellent mechanical properties, good corrosion resistance, easy

processing by plastic deformation and good welding behavior. Austenitic stainless steel has a lower hardness than martensitic stainless steel but has better corrosion resistance than it does; therefore, in the field of medical devices are used in the manufacture of orthopedic implants and non-surgical instruments (such as drill guides or locating devices).

The representative mark for austenitic stainless steels is the one containing 18% Cr and 8% Ni, the quality that is mainly used. These steels do not have a transformation point, at least above the ambient temperature. They consist of a single phase, which can dissolve relatively large amounts of carbon, keeping it in a state of supersaturation after a sudden cooling. Another notable feature of the 316L steel is plastic deformation inside the grain. This material is usually used in a 30% cold deformation condition because the cold formed metal has a flow limit, breakage limit and fatigue strength that are heavily elevated to the recoating state.

## 2. MATERIALS AND METHODS

The scanning electron microscopy (SEM) study allows obtaining qualitative information on porosity, grain size, particle size, and microstructural and micro-composite information.

In addition, these studies can provide useful information for understanding physical phenomena in the field of micro or nanostructured materials. An advantage of the SEM type analysis is the depth of penetration of the relatively large field.

The microstructural analysis was performed in the microscopy laboratory at the FEMTO-ST Besançon Institute in France using the scanning electron microscope (Figures 1.a,b). For a more accurate presentation of the particle morphology of the analyzed structures, SEM images, obtained for different areas of the analyzed sample, will be presented.

Surface roughness is defined as the set of irregularities that make up the real surface relief and whose pitch is relatively small relative to their depth. The average roughness of the surface (Ra) was determined using the profilometer type IQ Alpha-Step TENCOR, measuring the roughness at random points on the side surface of the piece. Parameters of interest are the average surface roughness (Ra) - which is defined as the arithmetic mean of the deviation from the median profile over the entire length measured, and squareness (Rq) - which is defined as the square root of the same values.

The metal structure of the CoCr alloy was obtained by rapid prototyping on the EOSINT M270 / PSW3.4 laser sintering machine from The National Institute of Research and Development in Mechatronics and Measurement Technique (INCDMTM) – Bucharest.

The compositional (elemental) analysis of conventional metallic materials (alloys based on Fe, Al, Cu, Co, Ni, s.a.) is made almost exclusively by SEOSE spectrometry [1-5]. In the field of spectrochemical tests there are both standards of competence of the laboratories and of the analytical method. Standards SR EN ISO / CEI 17 025, SR EN 13005 and European standards EA 04-16, ILAC 2000, etc. [6, 7] clearly states that the scientific substantiation of measurement is crucial for its proper modeling and for the development of a knowledge-based budget of uncertainty.

The scientific component and test refers to the knowledge of phenomenology involved in the measurement process, including mathematical modeling. For the spectrochemical test of these samples, an optical spark emission spectrometer of the Foundry-Master type is used.

For the spectrochemical analysis of samples from biocompatible material, samples were taken from a stainless steel Ni-Cr AISI 316L batch. In order to evaluate the conformity of the batch bars with Φ 35mm, three probes (C, D, E) as in Figure 2, were tested from the batch bars.

Samples were peeled and machined by milling. Subsequently, they were polished on surfaces, transversally. The results of the spectral tests of samples C, D, and E are presented in Table 2. The samples were subjected to the grinding operation and for this purpose the MLG 11 sanding machine was used.

In addition to other AISI 316L steel samples, two types of bars (with Φ = 10 mm and Φ=6 mm) were tested spectrochimically. A special clamping device was used to investigate these bars. The results of the tests are presented in Table 2. In order to clarify the performance of the method used, a reference material of type AISI 316L, which has the concentration specified by an accredited laboratory of Polytechnic University of Bucharest (UPB-SIM), has been used. The uncertainties of the UPB-SIM determinations on the reference sample are not estimated.

## 3. EXPERIMENTAL RESULTS

As can be seen in the figure in Figure 3, the laser beam transversely scraps the mark during its construction. The appearance of the surface of the piece also suggests a beam passage along its outline (Figure 3 a, b). Figure 4 shows the appearance of the side surface of the workpiece. The image also suggests a passage of the beam along its contour. The upper surface of the workpiece (the one processed by the laser beam) shows small dust or dimples (≈ 20-30 μm), figure 4 [8, 9].

The piece has a rough appearance in the lateral surface, the roughness being more pronounced in the lateral surface than the front surface, as can be seen in Figures 3, 4 and in the data centralized in Table 1.

The front surface roughness is Ra frontal = 0.244 µm, while the side surface roughness has a side Ra = 2.553 µm. The obtained values are centralized in Table 1 [8].

The lateral surface is much more irregular than the front surface.

Practically, the side surface consists of the powder particle profile, which was the origin of the piece manufacturing.

The rough appearance is clearly revealed in Figures 5- 6, which show the side faces of the workpiece.

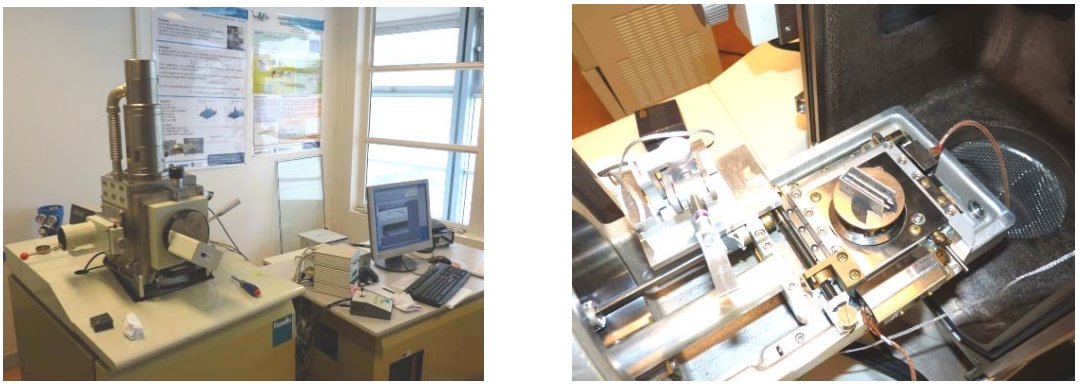

a) b)

**Figure 1. Scanning Electron Microscope - FEMTO Besançon Institute in France**


**Figure 2. The macroscopic appearance of C, D, E samples.**

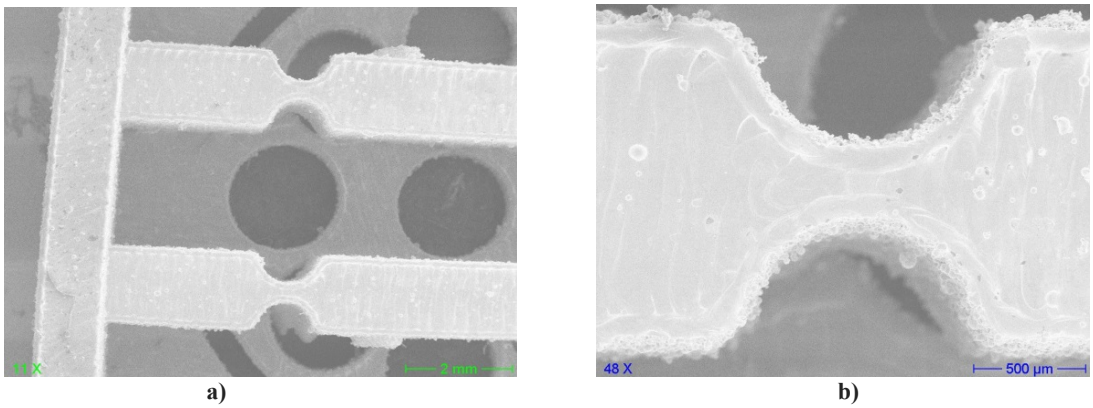


a) b)

**Figure 3. SEM micrograph of the CoCr alloy piece: front (a), detail (b).**

**Table 1. Roughness values for the CoCr piece**

| Surface analyzed | Roughness | Value (µm) |
|---|---|---|
| Front surface (x-y) | $R_a$ | 0.244 |
| Front surface | $R_q$ | 0.305 |
| The side surface (x-z) | $R_a$ | 2.553 |
| The side surface | $R_q$ | 2.924 |

The detail in Figure 5 highlights the lateral area of the manufactured piece where the sintered powder particles can be seen. In the largest proportion, the particles have the dimensions in the range 20-30 μm (Figure 6), although some of the larger ones can be highlighted.

*Experimental results by the Foundry Master emission spectrometer*

From Figure 7.c) it is observed that the concentration values of the Co element are non-homogeneous in the bar, after which the concentration of Co is homogenized. Cobalt has the highest coefficient of variation along the bar, which is 23%. It was found that the chromium element as well as the nickel have a homogeneous distribution along the bar, as can be seen in Figure 7.a), and the carbon element as silicon, phosphorus, titanium, vanadium are almost homogeneous (Figure 7.b).

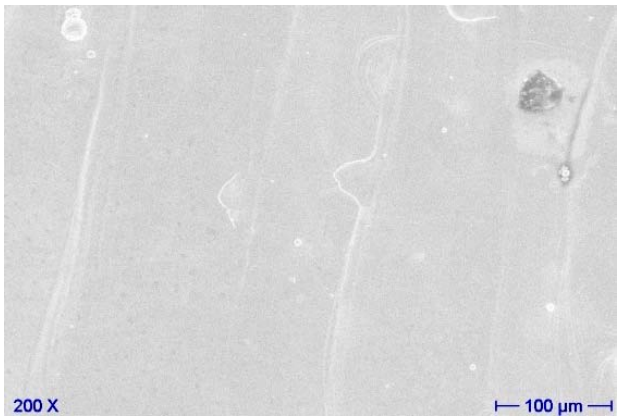


**Figure 4. Electronic side microscopy**

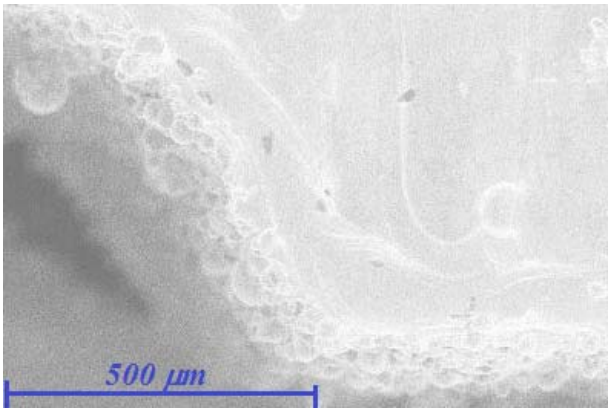


**Figure 5. Part aspect of the piece in the lateral area (top view)**

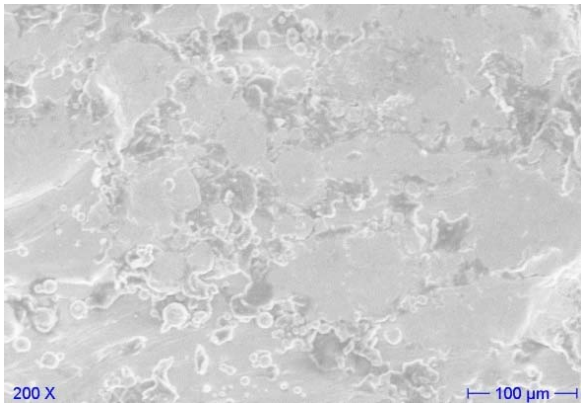


**Figure 6. Electronic microscopy of the side of the piece**

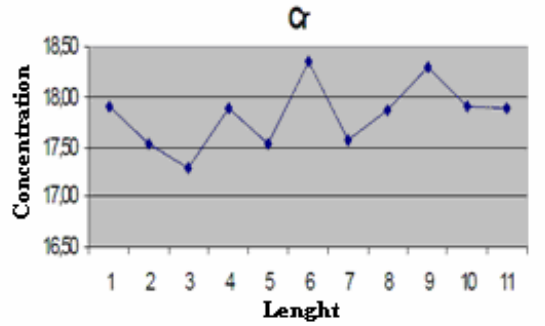


**a)**

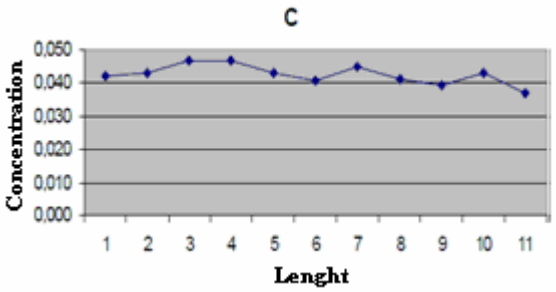


**b)**

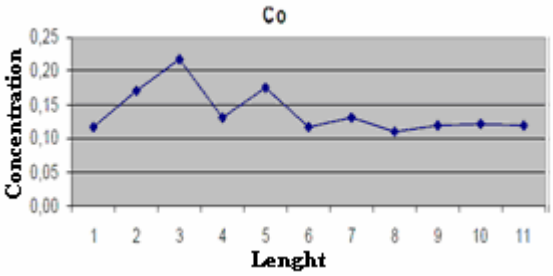


**c)**

**Figure. 7. a), b), c). Distribution of the concentration of Cr, C and Co elements in the AISI 316L steel bar**

**Table 2. Results of spectral tests of samples C, D, and E, bars and reference material type AISI 316L**

| Elemente | C | Si | Mn | P | S | Cr | Mo | Ni | Al | Co | Cu | Nb | Ti | V | W | B | Ca | Fe |
|---|---|---|---|---|---|---|---|---|---|---|---|---|---|---|---|---|---|---|
| PROBA C | 0,041 | 1,46 | 1,95 | 0,015 | 0,002 | 17,77 | 2,31 | 12,71 | 0,07 | 0,11 | 0,03 | 0,04 | 0,021 | 0,09 | 0,26 | 0 | 0 | 63,11 |
| | 0,045 | 1,50 | 1,83 | 0,015 | 0,002 | 17,76 | 2,27 | 12,49 | 0,07 | 0,10 | 0,03 | 0,04 | 0,016 | 0,09 | 0,25 | 0 | 0 | 63,48 |
| | 0,045 | 1,43 | 1,94 | 0,015 | 0,002 | 17,35 | 2,37 | 12,98 | 0,09 | 0,21 | 0,04 | 0,03 | 0,020 | 0,07 | 0,42 | 0 | 0 | 62,99 |
| | 0,045 | 1,43 | 1,94 | 0,015 | 0,002 | 17,35 | 2,37 | 12,96 | 0,09 | 0,21 | 0,03 | 0,03 | 0,020 | 0,07 | 0,42 | 0 | 0 | 63,15 |
| | 0,040 | 1,50 | 1,87 | 0,014 | 0,002 | 18,16 | 2,26 | 12,77 | 0,08 | 0,14 | 0,03 | 0,05 | 0,020 | 0,10 | 0,30 | 0 | 0 | 62,68 |
| Cmed | 0,043 | 1,46 | 1,91 | 0,016 | 0,002 | 17,68 | 2,32 | 12,78 | 0,08 | 0,15 | 0,03 | 0,04 | 0,019 | 0,08 | 0,33 | 0,00 | 0,00 | 63,08 |
| STDEV | 0,002 | 0,035 | 0,053 | 0,000 | 0,000 | 0,340 | 0,053 | 0,201 | 0,010 | 0,053 | 0,004 | 0,008 | 0,002 | 0,013 | 0,084 | 0,000 | 0,000 | 0,289 |
| U95% | 0,006 | 0,070 | 0,106 | 0,003 | 0,003 | 0,680 | 0,105 | 0,402 | 0,020 | 0,106 | 0,009 | 0,017 | 0,005 | 0,027 | 0,169 | 0,003 | 0,003 | 0,578 |
| Elemente | C | Si | Mn | P | S | Cr | Mo | Ni | Al | Co | Cu | Nb | Ti | V | W | B | Ca | Fe |
| PROBA D | 0,042 | 1,49 | 1,86 | 0,015 | 0,002 | 17,75 | 2,32 | 12,82 | 0,08 | 0,14 | 0,04 | 0,04 | 0,018 | 0,09 | 0,32 | 0 | 0,001 | 62,98 |
| | 0,043 | 1,52 | 1,98 | 0,016 | 0,002 | 17,45 | 2,29 | 12,65 | 0,08 | 0,15 | 0,03 | 0,05 | 0,021 | 0,08 | 0,44 | 0 | 0 | 63,09 |
| | 0,043 | 1,52 | 1,98 | 0,016 | 0,002 | 17,45 | 2,29 | 13,09 | 0,08 | 0,15 | 0,04 | 0,05 | 0,021 | 0,08 | 0,32 | 0 | 0 | 62,88 |
| | 0,041 | 1,46 | 1,95 | 0,015 | 0,002 | 17,77 | 2,31 | 12,71 | 0,07 | 0,11 | 0,03 | 0,04 | 0,021 | 0,09 | 0,26 | 0 | 0 | 63,11 |
| | 0,045 | 1,43 | 1,94 | 0,016 | 0,002 | 17,35 | 2,37 | 12,96 | 0,09 | 0,21 | 0,03 | 0,03 | 0,020 | 0,07 | 0,42 | 0 | 0 | 63,16 |
| | 0,043 | 1,48 | 1,94 | 0,015 | 0,002 | 17,55 | 2,32 | 12,84 | 0,08 | 0,15 | 0,03 | 0,04 | 0,020 | 0,08 | 0,35 | 0,00 | 0,00 | 63,04 |
| STDEV | 0,001 | 0,039 | 0,049 | 0,001 | 0,000 | 0,193 | 0,033 | 0,186 | 0,007 | 0,026 | 0,005 | 0,008 | 0,001 | 0,008 | 0,076 | 0,000 | 0,000 | 0,110 |
| U95% | 0,004 | 0,078 | 0,098 | 0,003 | 0,003 | 0,385 | 0,066 | 0,372 | 0,014 | 0,073 | 0,011 | 0,017 | 0,004 | 0,017 | 0,151 | 0,003 | 0,003 | 0,221 |
| Elemente | C | Si | Mn | P | S | Cr | Mo | Ni | Al | Co | Cu | Nb | Ti | V | W | B | Ca | Fe |
| | 0,042 | 1,51 | 1,87 | 0,015 | 0,002 | 17,83 | 2,26 | 12,68 | 0,07 | 0,12 | 0,04 | 0,04 | 0,021 | 0,08 | 0,25 | 0 | 0 | 63,17 |
| | 0,042 | 1,53 | 1,92 | 0,015 | 0,002 | 17,44 | 2,34 | 12,71 | 0,07 | 0,12 | 0,03 | 0,04 | 0,020 | 0,08 | 0,30 | 0,00 | 0,00 | 63,23 |
| PROBA E | 0,051 | 1,46 | 1,88 | 0,015 | 0,002 | 16,99 | 2,35 | 12,65 | 0,10 | 0,23 | 0,04 | 0,03 | 0,020 | 0,07 | 0,45 | 0 | 0 | 63,67 |
| | 0,044 | 1,43 | 1,94 | 0,014 | 0,002 | 17,50 | 2,32 | 12,78 | 0,10 | 0,21 | 0,03 | 0,03 | 0,017 | 0,07 | 0,44 | 0 | 0 | 63,07 |
| | 0,045 | 1,43 | 1,94 | 0,015 | 0,002 | 17,35 | 2,37 | 12,98 | 0,09 | 0,21 | 0,04 | 0,03 | 0,020 | 0,07 | 0,42 | 0 | 0 | 62,99 |
| Cmed | 0,047 | 1,44 | 1,92 | 0,015 | 0,002 | 17,28 | 2,35 | 12,80 | 0,10 | 0,22 | 0,04 | 0,03 | 0,019 | 0,07 | 0,44 | 0,00 | 0,00 | 63,24 |
| STDEV | 0,004 | 0,084 | 0,033 | 0,000 | 0,000 | 0,302 | 0,042 | 0,132 | 0,015 | 0,054 | 0,005 | 0,005 | 0,002 | 0,005 | 0,091 | 0,000 | 0,000 | 0,265 |
| U95% | 0,008 | 0,168 | 0,066 | 0,003 | 0,003 | 0,604 | 0,084 | 0,264 | 0,030 | 0,107 | 0,011 | 0,011 | 0,004 | 0,011 | 0,182 | 0,003 | 0,003 | 0,529 |
| Elemente | C | Si | Mn | P | S | Cr | Mo | Ni | Al | Co | Cu | Nb | Ti | V | W | B | Ca | Fe |
| Bara Dia 10 mm | 0,031 | 1,40 | 1,90 | 0,016 | 0,002 | 17,58 | 2,38 | 12,70 | 0,07 | 0,13 | 0,03 | 0,03 | 0,018 | 0,08 | 0,32 | 0,001 | 0 | 63,29 |
| | 0,028 | 1,52 | 1,97 | 0,017 | 0,002 | 18,68 | 2,36 | 12,92 | 0,07 | 0,13 | 0,03 | 0,04 | 0,022 | 0,08 | 0,30 | 0 | 0 | 61,81 |
| | 0,030 | 1,64 | 1,94 | 0,015 | 0,002 | 17,59 | 2,29 | 12,55 | 0,08 | 0,12 | 0,03 | 0,04 | 0,019 | 0,09 | 0,24 | 0 | 0,001 | 63,31 |
| | 0,034 | 1,54 | 1,90 | 0,020 | 0,002 | 17,57 | 2,27 | 12,61 | 0,08 | 0,13 | 0,03 | 0,05 | 0,017 | 0,09 | 0,27 | 0 | 0 | 63,36 |
| | 0,026 | 1,52 | 1,97 | 0,015 | 0,002 | 17,38 | 2,32 | 12,79 | 0,07 | 0,13 | 0,04 | 0,04 | 0,020 | 0,08 | 0,29 | 0 | 0 | 63,29 |
| Cmed | 0,030 | 1,52 | 1,94 | 0,017 | 0,002 | 17,76 | 2,32 | 12,71 | 0,07 | 0,13 | 0,03 | 0,04 | 0,019 | 0,08 | 0,28 | 0,00 | 0,00 | 63,02 |
| STDEV | 0,003 | 0,085 | 0,035 | 0,002 | 0,000 | 0,522 | 0,046 | 0,147 | 0,005 | 0,004 | 0,004 | 0,007 | 0,002 | 0,005 | 0,030 | 0,000 | 0,000 | 0,675 |
| U95% | 0,007 | 0,171 | 0,070 | 0,005 | 0,003 | 1,043 | 0,092 | 0,293 | 0,011 | 0,009 | 0,009 | 0,014 | 0,005 | 0,011 | 0,061 | 0,003 | 0,003 | 1,350 |
| Elemente | C | Si | Mn | P | S | Cr | Mo | Ni | Al | Co | Cu | Nb | Ti | V | W | B | Ca | Fe |
| Bara Dia 6 mm | 0,038 | 1,44 | 1,92 | 0,016 | 0,002 | 16,62 | 2,34 | 12,54 | 0,10 | 0,23 | 0,04 | 0,04 | 0,022 | 0,08 | 0,47 | 0 | 0 | 64,102 |
| | 0,033 | 1,52 | 1,98 | 0,016 | 0,002 | 17,45 | 2,29 | 13,09 | 0,08 | 0,15 | 0,04 | 0,05 | 0,021 | 0,08 | 0,32 | 0 | 0 | 62,878 |
| | 0,028 | 1,64 | 1,94 | 0,015 | 0,002 | 17,59 | 2,29 | 12,55 | 0,08 | 0,12 | 0,03 | 0,04 | 0,019 | 0,09 | 0,24 | 0 | 0,001 | 63,325 |
| | 0,034 | 1,54 | 1,90 | 0,020 | 0,002 | 17,57 | 2,27 | 12,61 | 0,08 | 0,13 | 0,03 | 0,05 | 0,017 | 0,09 | 0,27 | 0 | 0 | 63,367 |
| | 0,030 | 1,60 | 1,93 | 0,018 | 0,002 | 18,28 | 2,34 | 13,03 | 0,08 | 0,16 | 0,03 | 0,05 | 0,025 | 0,10 | 0,34 | 0 | 0 | 61,985 |
| | 0,031 | 1,51 | 1,98 | 0,016 | 0,002 | 17,76 | 2,32 | 12,91 | 0,08 | 0,16 | 0,04 | 0,05 | 0,020 | 0,08 | 0,34 | 0 | 0 | 62,699 |
| Cmed | 0,032 | 1,54 | 1,94 | 0,017 | 0,002 | 17,55 | 2,31 | 12,79 | 0,08 | 0,16 | 0,04 | 0,05 | 0,021 | 0,09 | 0,33 | 0,00 | 0,00 | 63,063 |
| STDEV | 0,002 | 0,056 | 0,034 | 0,002 | 0,000 | 0,327 | 0,028 | 0,245 | 0,000 | 0,018 | 0,005 | 0,004 | 0,003 | 0,006 | 0,045 | 0,000 | 0,000 | 0,567 |
| U95% | 0,006 | 0,112 | 0,069 | 0,005 | 0,003 | 0,653 | 0,056 | 0,490 | 0,003 | 0,036 | 0,011 | 0,009 | 0,007 | 0,017 | 0,090 | 0,003 | 0,003 | 1,134 |
| Elemente | C | Si | Mn | P | S | Cr | Mo | Ni | Al | Co | Cu | Nb | Ti | V | W | B | Ca | Fe |
| Proba Referinta | 0,028 | 1,69 | 1,90 | 0,015 | 0,002 | 18,48 | 2,31 | 13,00 | 0,08 | 0,12 | 0,04 | 0,04 | 0,020 | 0,08 | 0,30 | 0 | 0 | 61,995 |
| | 0,028 | 1,66 | 1,92 | 0,016 | 0,002 | 18,49 | 2,30 | 12,94 | 0,07 | 0,11 | 0,03 | 0,05 | 0,021 | 0,09 | 0,28 | 0 | 0 | 62,025 |
| | 0,028 | 1,64 | 1,94 | 0,015 | 0,002 | 17,59 | 2,29 | 12,55 | 0,08 | 0,12 | 0,03 | 0,04 | 0,019 | 0,09 | 0,24 | 0 | 0,001 | 63,325 |
| | 0,031 | 1,54 | 1,90 | 0,020 | 0,002 | 17,57 | 2,27 | 12,61 | 0,08 | 0,13 | 0,03 | 0,05 | 0,017 | 0,09 | 0,27 | 0 | 0 | 63,390 |
| | 0,032 | 1,63 | 1,92 | 0,015 | 0,002 | 17,44 | 2,34 | 12,71 | 0,07 | 0,12 | 0,03 | 0,04 | 0,020 | 0,08 | 0,30 | 0,00 | 0,00 | 63,251 |
| | 0,029 | 1,66 | 1,87 | 0,017 | 0,002 | 18,52 | 2,28 | 12,77 | 0,08 | 0,13 | 0,04 | 0,04 | 0,020 | 0,09 | 0,29 | 0 | 0,001 | 62,161 |
| Cmed | 0,030 | 1,63 | 1,91 | 0,017 | 0,002 | 17,92 | 2,30 | 12,72 | 0,08 | 0,12 | 0,03 | 0,04 | 0,019 | 0,09 | 0,27 | 0,00 | 0,00 | 62,830 |
| STDEV | 0,002 | 0,050 | 0,026 | 0,002 | 0,000 | 0,535 | 0,027 | 0,152 | 0,005 | 0,008 | 0,004 | 0,005 | 0,002 | 0,004 | 0,025 | 0,000 | 0,001 | 0,677 |
| U95% | 0,005 | 0,100 | 0,053 | 0,005 | 0,003 | 1,071 | 0,054 | 0,303 | 0,011 | 0,017 | 0,009 | 0,011 | 0,004 | 0,009 | 0,051 | 0,003 | 0,003 | 1,355 |
| Dif e abs | 0,002 | 0,036 | 0,010 | 0,002 | 0,000 | -0,568 | 0,014 | -0,284 | 0,004 | 0,002 | 0,008 | 0,004 | -0,001 | 0,008 | -0,050 | | | |
| Dif e % | 5,7 | 2,3 | 0,6 | 10,7 | 0,0 | -3,0 | -0,6 | -2,2 | -5,0 | 1,7 | -20,0 | 10,0 | -3,0 | 10,0 | -10,0 | | | |

## 4. CONCLUSIONS

The dimensional precision and surface quality of laser selective sintering parts are better than conventional parts, this technology being fast, flexible and allowing for prototype manufacturing. It is noted that the microstructural changes obtained affect the mechanical properties and the wear properties. Therefore, after the analysis, heat treatment is recommended to improve the mechanical properties of the alloy without loss of corrosion resistance.

By comparing the carbon concentrations in the AISI 316L steel samples C, D, E with the values specified in SR ISO 5832-1/1999, they do not satisfy the requirements of the standard. Even if it is considered to fit the carbon at the lower limit of the confidence interval, the samples can not be considered biocompatible. The sample of $\Phi = 10$ mm complies in the terms of SR ISO 5832-1/1999. Make a fit of the sample has $\Phi = 10$ mm as biocompatible is risky because the real Carbon concentration is in the range [0.23 ÷ 0.37] with a probability of 95%.

Therefore, it is very likely that the concentration value of Carbon is greater than 0.03%, in particular, it is risky to consider that the material is biocompatible. By comparing the data obtained from the UPB-SIM laboratory with the spectrochimic data obtained with the Foundry-Master instrument, it results that the concentration deviations are less than 0.01% for most of the dosed elements, and in the worst case they reach 0.56% what is normal for spectrochemical tests.

In this context, it can be considered that the method applied with the Foundry-Master spectrometer is at least at the level of performance of current modern apparatus. Under these circumstances, in order to evaluate the biocompatibility of AISI 316L type steels, it is necessary to improve the performance of the Foundry-Master spectrometer by reducing the impact of the influence factors.

**REFERENCES**:

[1]. V. Andrei, Fundamentarea şi optimizarea strategiilor de realizare a sistemelor de asigurare a calităţii în industria metalurgică, Teza de doctorat, Universitatea Politehnica Bucureşti, Facultatea Ştiinţa şi Ingineria Materialelor, 2006.

[2]. C. Dumitrescu, R. Saban, M.Petrescu, A. Aloman, M. Bane, D. Bojin, I. Ciuca, G. Cosmeleata, S. Gadea, N. Geru, B. Ghiban, St. Mantea, M. Marin, T. Negrescu, M.I. Petrescu, Tratat de stiinta si ingineria materialelor metalice, ISBN: 973-720-064-0, Vol 1, Ed. Agir, 2009.

[3]. E. M. Aldea, Metode fizico-chimice de evaluare şi caracterizare a unor biomateriale metalice utilizate în tehnica dentară, Teza de doctorat, Universitatea Politehnica Bucureşti, Facultatea de Chimie Aplicată şi Ştiinţa Materialelor, 2007.

[4]. V. Panaite, M. O. Popescu, Calitatea Produselor si Fiabilitatea Editura Matrix ROM, 2003.

[5]. I. Ioniţă, Metode Spectrale pentru Analize Medicale, Ed. Univ. Bucureşti, 2002.

[6]. www.standardservice.ro

[7]. SR ISO 5832-1:1999, Implanturi chirurgicale. Produse metalice. Partea 1: Oţel inoxidabil deformabil.

[8]. V. Despa, A. Catangiu, D.N. Ungureanu, I.A. Ivan, Surface structure of CoCrMo and Ti6Al4V parts obtained by selective laser sintering, Journal of Optoelectronics and Advanced Materials (JOAM)/ISSN 1454-4164, Vol.15. ISS.7-8/2013, pag. 858-862.

[9]. V. Despa, A. Catangiu, A. Cirstoiu, Aspects of the Mechanical Properties of CoCrMo Alloy Parts Made by Selective Laser Sintering, The Romanian Review Precision Mechanics, Optics & Mechatronics, 45/2014, pag. 81–83.

The Scientific Bulletin of VALAHIA University
MATERIALS and MECHANICS –Vol. 17, No. 16

DOI 10.2478/bsmm-2019-0002

# SPECIAL REFRACTORY CONCRETE FOR STEEL LADLE EQUALIZATION LAYER

**Nicolae ANGELESCU, Dan Nicolae UNGUREANU*, Vasile BRATU, Florin TOMA**

Valahia University of Targoviste, Faculty of Materials Engineering and Mechanics, 13 Aleea Sinaia Street, Targoviste, Romania

E-mail: * danungureanu2002@yahoo.com

**Abstract:** *This work is an attempt viewing to emphasize the possibility of using waste - as aggregate - from the demolition of silicoaluminuous refractory linings for manufacturing concrete with aluminuous cement. The article shows further on the possibilities of reducing the cement dosage and of using cheap admixtures.*

**Keywords:** *Recycled clay, aluminous cement, potassium fluoride, complex binding, ladle for steelworks, leveling layer.*

## 1. INTRODUCTION

One was previously concerned to equate some refractory concrete grades, which are offered for selling by firms, which are recognized as important producers of this kind of refractories. This is one of the main reasons for using rationally refractory concrete, but not always, functions of their thermo mechanical, structural and compositional properties, of conditions of the application medium and not at last, correlated with expenses determined by the context of reaching identical operation performances.

Another eloquent example is that of using expensive high aluminuous concrete (containing over 80% Al2O3) or magnesitic refractory masses at temperatures ranging from 400 to 12000C (known as critical temperature range for refractory concretes), like, for example, the leveling layer of casting ladles. The composition and mechanical - structural properties of the high-temperature performance refractory concretes recommend that they be used at significantly higher temperatures (this happens usually). However, the use of these refractories often at lower temperatures is due to the lack of a suitable alternative on refractory monolithic that could provide the most efficient solution required by specificity of the place application.

There are also intense preoccupations worldwide as concern the correlation of conditions imposed by as well the application medium or placement with the mechanical, structural and compositional properties as the costs of concrete and especially, concerning those concretes for special placements. As derived from this correlation (which determines, implicitly, the existence of a large range of grades) one applies rigorously refractory concretes having benefic influences on the decrease of materials expenses and finally, increasing the general efficiency.

By knowing the relationships between mechanostructural and thermo technological properties on one side and the composition of refractory concretes on the other side, one can obtain such products, which have to answer efficiently to the conditions of the planned placement.

Under these general circumstances, one should mention also the present preoccupations concerning the obtaining of thermo resistant concretes (having low cost prices and an application range from 400-12000C), by using aluminuous cements and capitalizing cheap refractory aggregates and specific admixtures, able to develop other hardening systems too, which action concomitantly with the hydraulic binding form and having a complementary influence on the hardening process.

The use of admixtures in refractory concrete manufacturing technology is due to the effect they have on the reducing of necessary cement content (which is also an expensive component and a fusion agent, also).
The effect of diminishing the proportion of cement is reflected on the increase of refractority for the new monolithic product. Reducing the cement content by using admixtures does not adversely affect the strength of the new product, but on the contrary, these admixtures will develop a strengthening structures with superior mechanical properties to those similar structures of the concretes with normal cement content, but non-additivated [1- 20]. This can be explained by the fact that the presence of admixtures acts on the growth and distribution of resulting hydrated neoformations that have a much larger specific surface area. At the same time, new binding forms are being developed which

coexist with the hydraulic form and which have a complementary effect on the global strengthening process. In this way there are the structural and morphological changes of the binding matrix - processes with direct and beneficial influence on the cohesion of the system, even using reduced cement content.

The effect of such substances, both associated or not with that of plastifying ceramic admixtures, of admixtures, which condition the chemical and colloidal binding or of high dispersed powders influencing the structural densification and sintering can determine establish superior resistance properties and can contribute to their benefic evolution if temperature is increasing. Thus, the positive consequences of hydraulic cement dosage decrease are better capitalized, due to the fact that, simultaneously, the cohesion tying forces matrix - aggregate are not diminished, and also the rheologic behavior and the workability of concretes being essentially improved.

## 2. RAW MATERIALS AND WORKING METHODS

An aluminuous cement (AC), containing 72% Al2O3 and 24% CaO was used as an agent of hydraulic binding. The proportion of cement ranges between 10 and max. 12%, complying with Low Cement Concretes. The fine powders of condensed silica fume (CSF) and special hydrated alumina (AH) represent the carriers of the coagulation binding system and at the same time, the stabilization agent (see [19]). These mineral powders were used at a ratio amounting to CSF/AH = 0.75. The electrolyte (powder phosphate which is soluble in water), acts as a pH regulator of the aqueous systems, during the hardening process and at the same time, possibly, as an admixture for the chemical binding. Potassium fluoride was used as a compacting agent and accelerator of the hardening process. One used as aggregate the Recycled Clay type D79 (STAS 4915/1976). Table 1 presents the qualitative properties of the materials used for the experimental samples preparation.
Concrete samples were made by casting - vibration. Physical properties (i.e., strength, porosity and density) have been performed on the standardized specimens. After max. 3 days of free hardening (at different times); the samples were dried at $110^0$C. After 2 days of free hardening, the samples were heated to$1200^0$C.

**Table 1. The chemical composition of raw materials**

| Chemical analyse, % | | | | | | |
|---|---|---|---|---|---|---|
| Raw materials | $Al_2O_3$ | $SiO_2$ | $Fe_2O_3$ | Alkali | CaO | Loss of ignition |
| Aluminuous Cement (AC) | 72 | 0.5 | 0.45 | 0.2 | 24 | - |
| Recycled Clay D79 | 55.2 | 36.6 | 1.78 | 0.2 | 1.3 | - |
| Special hydrated alumina(HA) | 64.6 | 0.03 | 0.025 | 0.35 | - | 35.0 |
| Condensed Silica Fume (CSF) | 0.46 | 87.5 | 1.73 | 1.20 | 1.1 | - |
| Potassium fluoride | min. 99% KF | | | | | |
| Aluminium Phosphate | $P_2O_5$ = Minimum 55.7% | | | | | |

## 3. RESULTS AND DISCUSSIONS

The analyze of data from table 2 shows that the new concrete (with 42% Al2O3) prepared with Potassium fluoride, which provides the hardening of the monolithic unit up to values within the critical range of temperature, develops mechanical strengths of great value even to short time hardening. Thus, at a day of free hardening, the sample develops a high compressive strength of 370 daN/cm$^2$ and after two days it reaches 430 daN/cm$^2$. It can be observed, by comparison, that the developed resistance of nonaditivated concrete at the same time is considerably lower (200 daN/cm$^2$ and 270 daN/cm$^2$, respectively).

**Table 2. Mechanostructural and thermo technological properties of free hardening concrete**

| Free hardening period, days | Strength, daN/cm$^2$ | Apparent density, g/cm$^3$ | Porosity, % |
|---|---|---|---|
| 1 day, dried at 110 $^0$ C | 370 (200) | 2.69 (2.54) | 21 (33) |
| 2 days, dried at 110 $^0$ C | 430 (270) | 2.71 (2.55) | 22 (32) |
| 3 days, dried at 110 $^0$ C | 460 (330) | 2.72 (2.57) | 23 (32) |
| Water Necessary, % | 7 (16.5) | | |

x) For comparison, the properties of the concrete with refractory clay aggregate and 20% cement without admixtures are put in brackets.

The increase of strength for the additivated concrete after 3 days of free hardening (460 daN/cm$^2$) is still of little importance as compared with that developed after 2 days (430 daN/cm$^2$) due to the fact that it increases only by 7%; one observes once again the importance of hardening for this concrete after 2 days of free hardening.

At the same time it can be noticed that the structure of the new investigated concrete has a higher density compared to that of a refractory concrete with the normal cement dosage (20%), but without admixtures. The improved compactness of the new studied concrete is the result of a lower porosity and a different pore size distribution – fig. 1, an aspect which was confirmed by investigations performed using electron microscopy, also. Thus, by reducing of the cement dosage, correlated with the use of admixtures, one can observe that the size of the majority pores shifts towards lower values. While the majority pores of nonadmixtured concretes show a radii between 1-10 μ, this category of pores for the additivated concretes shows radii ranging from 0.1 to 1 μ. At the same time, the presence of pores with a radius of less than 0.1 μ is diminished. So, this dimensional pore change determines the development of the more densified structures for the studied monolithic.

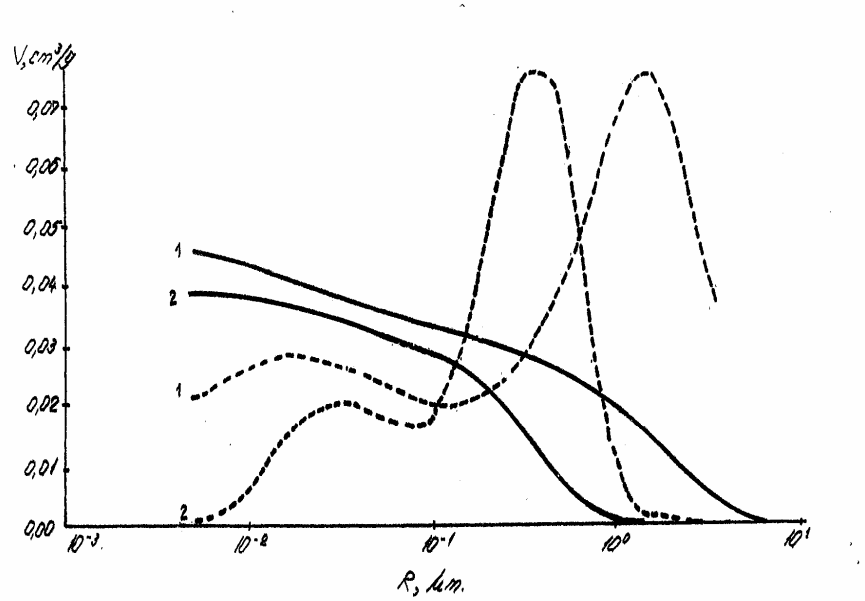


**Figure 1. Distributive porosity (_____integral curves, _ _ _ _ _ differential curves) of concretes after two days of free hardening: 1. Concrete without admixtures; 2. Concrete with admixtures**

On the other hand, this also results from the of the electron microscopy investigations (Figure 2) also, which show that the structure of the new concrete with admixtures is more compact compared to concrete with 20% cement, but nonadditivated.

As resulting from the above mentioned, there is no doubt that the beneficial effect of admixtures used is observed on short hardening terms (1 and 2 days), when, e.g., after 2 days of free structuration, the concrete with admixtures develops, as before said, a mechanical resistance to compression of 430 daN/cm$^2$, which allows the permanent and wear-resistant linings to be applied on the leveling layer of the steel transportation ladle.

The aim pursued was to accelerate the hardening process of concrete, which is used as equalization layer, this one becoming enough mechanically resistant after 2 days of hardening, thus, being able to provide the start-up of the building works of refractory linings for ladle and also, to resist to mechanical stress determined by the refractory brickwork (the permanent and the wear resistant linings) and by the molten steel mass, also.

Thus, it was possible to establish the characteristics of the concrete at 1200$^0$C (the highest temperature for which one supposes the equalization layer operates), after 2 days of free hardening, see table 3.

The performed analysis reveals that for 1200$^0$C the main mechanostructural characteristics of concretes remain the similar as those emphasized in the case of free hardening product.

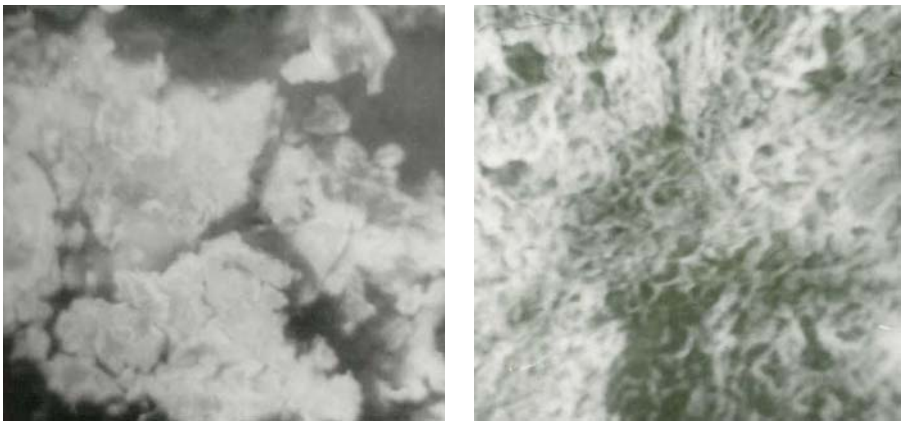

**(a)** **(b)**

**Figure 2. The microstructure of the concrete after two days of free hardening (x 1000): a. Concrete without admixtures; b. Concrete with admixtures**

**Table 3[x]. Mechanostructural properties of thermo resistant concretes heat-treated, after 2 days of free hardening**

| Heat treatment temperature, $^0$C | Strength, daN/cm$^2$ | Apparent density, g/cm$^3$ | Porosity, % | Dimensional variation, % |
|---|---|---|---|---|
| 110 | 430 (270) | 2.71 (2.55) | 22 (32) | - |
| 1200 | 440 (200) | 2.69 (2.40) | 24 (34) | + 0,06 - 0,21 |
| Refractoriness, $^0$C | 1700 (1650) | | | |

x) For comparison, the properties of the concrete with chamotte aggregate and 20% cement, without admixtures, are put in brackets.

This ascertainment is a supplementary reason to believe that the new concrete will appropriately behave under running conditions as leveling layer of the casting ladle having 50t or 180 t steel capacity (see [20]).

It must be emphasized that the refractoriness value of the studied concrete is superior to the temperatures for which it operates as equalization layer.

The fact that the new concrete emphasize a slight expansion to heating (+ 0.06%) - is another reason concerning a good running behavior.

As derives from the above mentioned and encouraging results, obtained previously by using concretes, which are analogous from the viewpoint of conception, for steam power plant coppers, deep furnaces and for the 50 t ladle [20], one can sustain that the investigated thermo resistant concrete prepared with admixtures can be used as leveling layer for the 180 t casting ladle. After 2 days of hardening, it is can be realized the permanent and wear-resistant brickwork structure.

## 4. APPLICATIONS

One used previously a special concrete as equalization layer [21 - 24] for the ladle of 50 t and 180 t steel capacity at SIDEX Galati steelworks, figure. 3.

The very good behavior of the investigated ladles permitted the generalization , in the years 1997-1998, of this solution at SIDEX Galati, thus, being saved 200,000 US$ yearly.

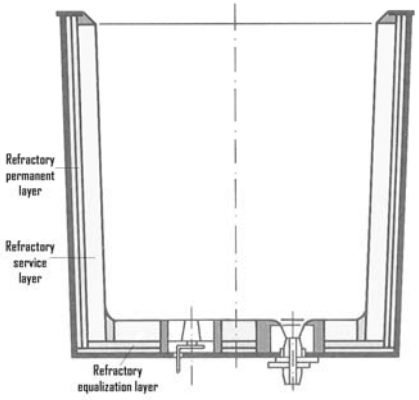


**Figure 3. The ladle used in steelworks**

## 4. CONCLUSIONS

The clay selected from the destruction of resistant to heat linings can be reused for thermo resistant concrete manufacturing. The free strengthening of these concretes takes place by the active contribution of a complex binding system (due to simultaneous existence of the coagulation, chemical and hydraulic binding forms), where the hydraulic one (due to the aluminous cement) is of the first importance.No behavior differences were observed using Potassium fluoride (as a compacting agent and accelerator of the hardening process) instead of Lithium fluoride (experimented in other works on the same subject)

## REFERENCES


[1] Li, Z., Ye, C. – Bonding and Recent Progress for Some Monolithic Refractories. Interceram 41 (3), 169, 1992.

[2] Prost, L. – Les Refractaires Moulables. L'industrie Ceramique (661), 279, 1973.

[3] Rebouillant, L., Rigaud, M., Ildefonse, J. P., Gabis, V., Dubreuil, P., Daniellou. P., Cement-free Castables with Micronized Andalusite. 9th SIMCER, Bologna, Italy, 5-8 October, 1998.

[4] Angelescu, N., Bertalan, V., Mihalache, F., Rădulescu, G., Catone, D., Savin, D. – Realizări şi Perspective privind fabricaţia şi utilizarea refractarelor monolitice speciale – lucrare prezentată la Simpozionul Naţional de Metalurgie, Bucureşti, 1993.

[5] Angelescu, N. - Materialy ogniotrwale do indukcyinych piesow stalowniczych. Materialy Ogniotrwale, 4, 93, 1989.

[6] Lankard, D, R, et al – Refractory Concretes for Steelplant Applications. Refract. Journal, 1, 6, 1986.

[7] Kawasaki, S. – Life Extension by using Unshaped Refractory for Powder Injection Lance. Taikabutsu Overseas, 6, (1), 34, 1986.

[8] Angelescu, N. - Complex Binding Matrix. Special Magazine on Engineering Materials, Jyubliana, 1996, 1, 11-13.

[9] Teoreanu, I., Angelescu, N. – Betoane refractare cu continut redus de ciment. Materiale de Construcţii, 8 (3), 127, 1978.

[10] Teoreanu, I., Angelescu, N. – Influenta $CrO_3$ asupra intaririi si proprietatilor betoanelor refractare cu dozaj redus de ciment. Materiale de Construcţii, 10 (4), 195, 1980.

[11] Chastant, M. – Materiaux coulables pour le revetement refractaire de rigoles de couless du haut fourneau. Rev. de Metallurgie, 83 (10), 719, 1986.

[12] Moreau, I.P. – Development of low Cement and Ultra low Cement Castable in Combustion Chamber and Boilers of Domestic Waste Incinerators. Interceram, 37 (Refractory Special Issue), 1987, 8.

[13] Avis, R., et al – Monolithic Permanent Linings in Tundishes. Interceram 36 (Refractory Special Issue), 33, 1987.

[14] Teoreanu, I., Angelescu, N. - Fundamentals in Developing New Generations of Refractory Concretes. Concretes with Simple and Complex Binding Systems. Rumanian Chemical Quarterly Reviews, 1996, 4 (1-2), 123-147.

[15] Teoreanu, I., Angelescu, N. - Hardening Processes for Some Refractory Binding System - Kinetic Considerations and Mechanisms. The 9th International Congress on Chemistry of Cement, New Delhi, India, vol. 3, pp. 351-357, 1992.

[16] Lapauyade, P., et al – Traite pratique sur l' utilisation des produits refractories. Editura H. Vial Dourdan, 1986.

[17] Pivinskii, Yu, E. – Ogneupornoe betonî novogo pokolenia. Nizkozementnie betonî, nalivnie vibrazionnie tikotropnie ogneupornie massî. Ogneuporî 55 (7), 1-10, 1990.

[18] Teoreanu, I., Angelescu, N. – Noi generatii de betoane refractare aditivate cu continut redus si foarte redus de ciment aluminos - Mecanisme de intarire. Materiale de Construcţii, 21, (2-3), 68, 1991.

[19] Shataff H, Alshamsi A M, - The Effect of Condensed Silica Fume on some Properties of Concrete in Hot Climate. First International Conference on Reinforced Concrete Materials in Hot Climates, Al Ain, United Arab Emirates, April, 24-27, 1994.

[20] Angelescu, N. – Special Monolithics for Steelmaking Ladles. Macarie Publishers, Targoviste, 2002.

[21] Xxx. Technical Report. Metallurgical Research Institute Bucharest, 1997 - 1998.

[22] Xxx. Technical Report. Metallurgical Research Institute Bucharest, 1999.

[23] Angelescu, N., Amziane, S., Ionita C., Ion, I., Stanciu, D. - *Concretes for Special Applications.* Advanced Materials Research, Vols. 479-481, pp 595-600, 2012.

[24] Angelescu, N., Amziane, S., Ionita C., Ion, I., Stanciu, D. - *Special and New Monolithics***.** Advanced Materials Research, Vols. 479-481, pp 362-365, 2012.

The Scientific Bulletin of VALAHIA University
MATERIALS and MECHANICS –Vol. 17, No. 16

DOI 10.2478/bsmm-2019-0003

# MECHANICAL PROPERTIES OF FERRITIC MARTENSTIC STEELS: A REVIEW

**Hiwa Mohammad Qadr[1*], Ari Maghdid Hamad[2]**

[1]Department of Physics, College of Science, University of Raparin, Sulaimanyah, Iraq, [2] Department of Physics, Faculty of Science and Health, KoyaUniversity, Erbil, Iraq

E-mail: * hiwa.physics@uor.edu.krd

**Abstract:** *The word-wide demand for energy is constantly increasing, and therefore ideas around future energy-generation are also on the increase with the aim of meeting this demand. This includes designs for the next generation of nuclear power reactors, such as gas-cooled, liquid-metal-cooled and water-cooled reactors; the goal being to create smarter ways to produce more economical, environmentally-friendly energy. The conditions such reactors would need to meet, present significant design challenges for scientist and engineers, not least around the structural materials and components to use. Depending on the operational conditions, use of elevated- temperature ferritic/martensitic materials such as P91 and P92 steel are favoured by several of the designs for use with out-of-core and in-core applications. The main goal behind this review article is to explain mechanical properties of P91 and P92 steel; these are two types of ferritic/martensitic steels. This reviewer, highlight and discuss the development of ferritic/martenisitc steels for nuclear programmes and to explain the effect of irradiation on mechanical properties of P91 and P92.*

**Keywords:** *Ferritic-martensitic steels, Microstructure, Irradiation hardening, Embrittlement, Swelling*

## 1. INTRODUCTION

Fast reactors can generate capacity by using $U^{238}$ or $Th^{232}$ without losing any net of thermal materials. Whereas, to generate power, a thermal reactor use $U^{235}$ that forms only 0.7% of natural uranium. Thermal reactors can also use some of $U^{238}$ by converting it to $Pu^{239}$ as a result of fission, but only a very small amount of $U^{238}$ can directly be converted. The amount of energy, which can be extracted from natural uranium via a thermal reactor, is 60 to 80 times lower than the energy that can be procured by fast reactors, even allowing for all the losses during fuel recycling necessary in the fast reactor process [1].

The economic situation has had an impact on every fast reactor programme. It was in the early 1940s that the potential concept of the fast reactor as an energy generator was first conceived. Scientists discovered that $U^{235}$ isotopes are very limited on earth, and so it became clear that it would be important to develop a way of using $U^{238}$ as a power source in a fast reactor. At the time, it was also thought that because the fast reactor cores were smaller than thermal reactor the cost of reprocessing plutonium-containing fuel would be lower. The expense turned out later to have been under-estimated. Overall, it was thought that the cost of building fast reactors was lower than building thermal reactors. This explains the rapid development of fast reactors in countries such as USA, USSR and the UK. A number of reactors were built and operated in these locations, providing up to 100MW power [2].

In late 1951, Experimental Breeder Reactor I (EBRI), the world's first reactor, was built to generate electricity. Thereafter, during the 1970s several reactors were built, such as PFR in the UK, PHENIX in France, BN350 in U.S.S.R, and a few years later SNR300 was built in Germany; these each had thermal outputs of 500MW to 1000MW. The first large prototype of a fast reactor was BN600 in the U.S.S.R (600MW (E)) in the 1980s, after which a number of reactors were built across Europe, such as the criticality of Super Phenix (120MW (E)) in 1983 in France, BN1600 (1600MW (E)) in U.S.S.R, CDFR (120MW (E)) in the UK, SNR2 (1300 MW (E)) in Germany, and Super Phenix II (1500MW (E)) in France. Table 1. Shows the list of largest fast reactors power generation in the world [1].

**Table 1. List of largest fast reactors power generation in the world**

| Name | Location | Date critical | Thermal power (MW) | Electrical power(MW) |
|---|---|---|---|---|
| BN350 | U.S.S.R. | 1972 | 1000 | 150a |
| Phenix | France | 1973 | 570 | 250 |

| | | | | |
|---|---|---|---|---|
| PFR | U.K | 1974 | 600 | 250 |
| BN600 | U.S.S.R. | 1980 | 1470 | 600 |
| Super Phenix | France | 1985 | 3000 | 1200b |
| SNR-300 | West Germany | Construction complete | 770 | 325 |
| Monju | Japan | Under construction | 715 | 280 |
| BN800 | U.S.S.R. | Under construction | 2100 | 800 |

## 2. FAST REACTOR CORE COMPONENTS

In the fuel subassemblies of fast reactors, wrapper and clad tubes are used, as the fuel assemblies suffer the most damage during operation, due to an intense combination of high neutron radiation at high temperature. This causes some material problems such as irradiation hardening, irradiation growth, void swelling, irradiation embrittlement, helium embrittlement and irradiation creeps. The choice of materials of subassembly, the dominant core structural component, is governed by any deterioration in the mechanical properties and resistance to void swelling. In early fast reactors, austenitic stainless steel (type 316) was used, which works in less-than-20% cold condition, whereas the 316 austenitic stainless steel has low achievable burn-up, about 50 dpa [3].

Over time, materials for fast reactor core components have evolved and a new type of materials has begun to be used, in the form of ferritic and ferritic/martenisitc steels. Ferritic steel has high void swelling resistance as it consists of a central cubic crystal structure; this is more open compared to austenitic steel that has a face-centered cubic crystal structure. This leads to faster diffusion in ferritic steel. Another reason that ferritic steel has higher void swelling resistance is because the ferritic steel has lower cavity density compared to the higher defect sink strength in ferritic martensitic steel. On the other hand, ignoring void swelling, it is considered that 9-1%Cr ferritic- martenisitc steel offers a more long-term solution for core component material in fast reactors. There are some types of ferritic/martensitic such as 9Cr-1Mo(Gr.91), 9Cr-1Mo (EM10), 12Cr-1MoVW(HT9) and 9Cr-2MoVNB(EM12), which have good resistance to radiation even up to 200 dpa. Despite this advantage, these alloys have low creep resistance at high temperatures, typically those above 823K. Therefore, ferritic martenesitic cannot be used for applications, which require high creep strength. Ferritic/martenesitic steels such as P91 and P92 tend to be used for wrapper material because they can operate at low temperature and at low pressure.

In conclusion, it has been observed that radiation and high temperature have several effects on reactor core components, namely irradiation hardening, irradiation creep, irradiation embrittlement, void swelling, helium embrittlement and irradiation growth. Studies have concentrated on such issues as they put the largest constrain on reactor lifetime. These are discussed in detail later [3].

## 3. FERRITIC 9Cr STEELS

Over the past century, the nuclear community has attempted to extend the lifetime of components and to enhance the development of radiation-resistance materials. Over this timeframe, three ‘generations’ of materials have been developed, increasing burn up fuel 45 dpa to 316 for austenitic stainless steel, and for ferritic steels to above 180 dpa; currently there are efforts to achieve a target burn-up of 250 dpa through use of advanced ferritic steels. The present generation of ferritic and ferritic- martensitic steels has been developed not only for their resistance to high temperatures, but also for their creep-resistance. This started with carbon and C-Mn steels, which had a maximum temperature nearly 523 K, and it improved with various levels of molybdenum and chromium. As a result the temperature has been increased about 873 K with improvement in Cr-Mo steels. Presently, the ferritic and ferritic- martensitic steels not only have a high temperature and creep resistance, but they also provide the best void swelling, embrittlement, and have a microstructure which is relatively simple to manipulate [4].

## 4. FERRITIC/ MARTENSITIC STEELS FOR NUCLEAR REACTORS

### 4.1 Fission reactor

In the 1970s, the main materials for fast reactor in-core applications, such as wrapper, cladding and duct, were (9-12%Cr) ferritic/martensitic steel because they have lower expansion coefficients and higher thermal conductivity compared to austenitic steels. Moreover ferritic/martensitic have extremely good irradiation resistance to prevent swelling [5].

In Europe in the 1960s, the Sandvik HT9 (Fe-12Cr-1Mo-0.5W-0.5 Ni-0.25V-0.2C) was developed for power generation industry. Then in USA the same materials were investigated for their potential within a fast reactor programme, with similar kind of steel being explored simultaneously in Europe; EM-12 ,JFMS, FV448, and DIN1.4914, in France, Japan, United Kingdom,

Germany , respectively. Explorations around HT9 and the above steel materials brought to light a large amount of information about their physical and mechanical properties, both before and after irradiation within nuclear reactors [6].

Coming more up to date, ferritic and martensitic (high chromium 9-12% Cr) steels are now used in Generation IV reactor applications, as there is an extremely high temperature threshold in Generation IV reactor designs. However, in some parts of the reactor which operate at lower temperatures, such as piping, pressure vessels, etc,) low alloy steels are used. In commercial light water reactors, the pressure-boundary component uses low alloy ferritic and bainitic steels, namely A533B, because the pressure-boundary operates at high temperature. It has been observed that steel with lower chromium than 9-12% could probably be used in these applications, negating the use of steels such as A533B [7].

### 4.2 Fusion reactor

Ferritic/martensitic steels were used for early fast reactor programmes in Japan and Europe [8]. Then, similarly in the late 1970s in the USA, the same steels were considered for fusion reactor programmes, with structural materials such as Sandvik HT9 steel, being the primary one considered [6, 9]. In around 1985, the international fusion programme introduced the notion of low-activate materials [5]. The purpose of this was to build fusion reactors using materials which, when irradiated, would not activate, or even if activated, the radioactive decay would be so fast as to maintain only low levels of radiation, thus increasing the safety of operations and hands-on maintenance. In reality, it is virtually impossible to provide “low activation” steels, because the decay of radioactive products from transmutation of the iron atoms limits the low-activation steels. “Reduced-activation” however, did prove a more feasible concept to make into a reality [10].

In the mid 1980s to early 1990s, reduced-activation ferritic/ martensitic steels were developed via fusion reactor materials research programmes in Europe, the USA and Japan. Reduced-activation steels decays a short time after they are irradiated and activated, therefore they require only shallow land burial when disposing of decommissioned plant components. Depending on nuclear calculations, the steel alloying elements Nb, Mo, Cu, N, and Ni require minimizing or eliminating [11].Furthermore, to produce the reduced-activation steels, there must be a process of replacing molybdenum with vanadium or tungsten in conventional Cr-Mo steels. In addition, tantalum needs to be added as a replacement for niobium. Steels with more than 12% chromium were not favoured, because without increasing manganese or carbon for austenite stabilization, it is difficult to eliminate σ-ferritic in these proportions. Because of this steel with 7-9% chromium were favoured. Delta-ferritic can demonstrate lower toughness, and can be suffer from embrittlement [12], because manganese promotes chi-phase precipitation during irradiation. In the end 7-9% Cr steels were borderline, and selected for further investigation, development and study, whereas steels with 2.25%Cr were certain to be considered [13].

Finally, in Europe, Fe-8.5Cr-1.0W-0.05Mn-0.25V-0.08Ta-0.05N-0.005B-0.10C (Eurofer) steels were chosen and investigated [13], and in Japan Fe-7.5Cr-2.0W-0.2V-0.04Ta-0.10C (F82H) steels were chosen for the programme. In the USA, the steel with the most appropriate features and properties was a Fe-9Cr-2W-0.25V-0.07Ta-0.10C steel. Compositions of reduced activation steels currently of interest in international fusion reactor programmes, as shown in the Table 2. [7].

**Table 2. Nominal Composition of Reduced-Activation Steels (wt %)**

| Program | Steels | Cr | Si | Mn | Cr | W | V | Ta | N | B | Others |
|---|---|---|---|---|---|---|---|---|---|---|---|
| USA | ORNL 9Cr-2WVTa | 0.10 | 0.30 | 0.40 | 9.0 | 2.0 | 0.25 | 0.07 | | | |
| Europe | EUROFER | 0.11 | 0.05 | 0.5 | 8.5 | 1.0 | 0.25 | 0.08 | 0.03 | 0.005 | |
| | OPTIFER TWO | 0.125 | 0.04 | 0.5 | 9.40 | | 0.25 | | 0.015 | 0.006 | 1.1Ge |
| Japan | F82H | 0.10 | 0.2 | 0.5 | 8.0 | 2.0 | 0.2 | 0.04 | <0.01 | 0.003 | |
| | JLF-1 | 0.10 | 0.08 | 0.45 | 9.0 | 2.0 | 0.2 | 0.07 | 0.05 | | |
| | OPTIFER 1a | 0.10 | 0.06 | 0.5 | 9.3 | 1.0 | 0.25 | 0.07 | 0.015 | 0.006 | |

## 5. STEEL P91

In 1970, P/T91 steels were developed in the USA for nuclear programme by combustion engineering and Oak Ridge National Laboratories, based on the 9 Cr- 1Mo tube steel. The creep strength of P91/T91 was enhanced by adding small amount of N, Nb, and V with optimization of the alloy composition. Around 1984, it was discovered that P91 steel could be used in the ASME code, and in conventional steam plants. In 1988 the first large application of the P91/T91 steel was used at USC steam conditions in Kawagoe Plants, with steam parameter 31MPa/566 C in Japan [14].

It must be recognised that there are some disadvantages to P91. Whilst there was a demand for ferritic steels with

high creep strength, which led to the improvement in 9-12 chromium martensitic steels, such steels were improved because of the demand for ferritic steels with high creep strength. However, their long-term performance in terms of actual plant functionality is less well known, especially concerning dense section components such as steam pipe and headers. [15] highlights the need for cautious observations to evaluate long-term performance of components made from 9%Cr martensitic steels. He highlights research indicating a number of unexpected premature failures of P91 welding within nuclear plant, but acknowledges the complexity of factors leading to such failures.

## 6. STEEL P92

In the mid 1980s, NF616 steels, which comprise tungsten alloyed 9% Cr steel, were produced for the first time, based on the long-term studies Professor Fujita at the University of Tokyo, on 9-12% Cr steels. The basic concept to create this new steel is to add boron and replace a part of molybdenum with tungsten, approximately 1.8%. This development spread around the globe and was used by boilermakers, steels makers and many in industry. Furthermore, in Denmark, Japan, USA, and the UK, the process was customized for pipe bending, welding procedures and pipe production. This enabled long-term data on creep for this steel, to be collated. Eventually, in 1994, ASME code approval for this steel was given, and it was labelled P92. in 2001, the first large application for P92 steel was in the Danish 400 MW USE nuclear power plant, with steam parameter 30 MPa/580 C/600 C [15].

## 7. BASIC METALLURGY AND CHEMICAL COMPONENTS

In the mid of seventies after a quiet period, development of materials restarted in countries such as USA and Japan. As a result, a new type of steel was created in USA., namely T/P91 that was designed like (X10CrMoVNb9-1). This steel has been used in the refurbishment of high temperature/high pressure piping system and new nuclear power plant throughout the world [16].

The carbon content in T/P91 is lower than X20CrMoNiV11-1, but significantly, the creep rupture strength of T/P91 is higher than X20CrMoNiV11-1. This is because T/P91 contains the alloys vanadium and niobium, which create Nb/V- these carbonitrides, of type MX, bring additional strength. This was important to the balance of compositions, because particle size and an optimum dispersion of MX can only be attained by an optimized Nb/V- ratio, in addition to nitrogen content. On the fundamental principles of T/P91, other new steel grades have been developed, such as T/P911, T/P92 and T/P122; these steel grades represent the latest stage of evolution in creep resistance ferritic steel to date [17, 18].

**Table 3. Outline the typical weight percentage of each alloying element in T/P91 and T/P92 steel**

| | C | Si | Mn | Al | Cr | Ni | Mo | W | V | Nb | B | N |
|---|---|---|---|---|---|---|---|---|---|---|---|---|
| T/P91 | 0.08 - 0.12 | 0.20 - 0.50 | 0.30 - 0.60 | max. 0.040 | 8.00 - 9.50 | max. 0.40 | 0.85 - 1.05 | | 0.18 - 0.25 | 0.06 - 0.10 | | 0.030 - 0.07 |
| T/P92 | 0.07 - 0.13 | max. 0.50 | 0.30 - 0.60 | max. 0.04 | 8.50 - 9.50 | max. 0.40 | 0.30 - 0.60 | 1.50 - 2.00 | 0.15 - 0.25 | 0.04 - 0.09 | 0.001 - 0.006 | 0.030 – 0.070 |

From Table 3. is clear that T/P92 contains extra alloying elements in the form of boron and tungsten, in order to avoid the formation of σ-ferritic in the microstructure, the molybdenum content of these high-tungsten steels decreased to about 0.5 % [19].

## 8. EFFECTS OF COMPONENT ELEMENTS ON PROPERTIES

The terms Ferritic and martenisitc steel refer to a material's crystallographic structure; ferritic is body centered cubic, whereas martensite has a distorted tetragonal that represents a distorted face-centered cubic structure converting into a body-centered structure. Ferritic and ferritic- martensitic materials consist of several alloy elements, each of them bringing a specific feature or property to the material, thus being added into the metal for that purpose. This includes the adaption of mechanical properties, namely strength and toughness.

T/P91 and T/P92 are types of ferritic steel that contain some chemical compositions. A discussion follows as to these compositions' effects on steel P91, 92 [7].

### 8.1 Effect of Chromium

Chromium, which is a ferrite stabilizing element, can be added to steel for corrosion and oxidation resistance. If it is added to iron, it will provide solid-solution strengthening. Furthermore, Carbides such as $M_7C_3$ and $M_{23}C_6$ are formed by carbon chromium reaction in the 2-12% Cr steels $M_7C_3$ Carbide forms in chromium steels (<7% Cr). The $M_{23}C_6$ carbide dominates in the 9-12% chromium steels; it forms during tempering and stays present all through the raised temperature exposure. It has been observed that $M_{23}C_6$ carbide forms in the P91 steels. The creep resistance properties occur as a result of grain boundaries, also a pinning of dislocations by these secondary phase precipitates [20].

### 8.2 Effect of Tungsten and Molybdenum

Tungsten and molybdenum elements, which have been utilized in heat resistance steels, are effective solid-solution strengtheners. Tungsten is present in modified 9Cr-1Mo, and usually contains about 1.8% W and 0.5 wt% Mo, whereas around 1wt% Mo is standard for P91 steels (9Cr 1Mo V Nb) type .It has been observed in the literature [7] that molybdenum is effective in high temperatures with properties of 9% chromium steels, and also that creep rupture and elevated temperature go up when the molybdenum content is raised. Tungsten and molybdenum are ferritic stabilizers, and their presence must be limited to avoid δ-ferritic; in a tempered condition they are divided between the solid-solution and in this way incorporated in the MX and $M_{23}C_6$. Therefore, the solid solution strengthening of iron increases relatively significantly by these elements. Tungsten diffuses more slowly than molybdenum, which slows laves precipitation and recovery processes [7].

Adding tungsten and molybdenum atoms to steels produces a local strain within the matrix lattice, and thus impedes the free movement of dislocations. As a result, creep rupture strengthens and hardness increases within the steel. It also has been observed that the solid-solution strengthening effect of W/Mo reduces dramatically during creep exposure because of laves phase precipitation. However, this can be compensated for by raising the quantity of W/Mo in solid solution in the received steel. This is due to the solid solubility of Mo in P91 steel; this needs to be around 1 wt% at 600C [7].

### 8.3 Effect of Vanadium and Niobium

The vanadium (V) and niobium (Nb) are strong carbide, nitride, and carbonitride formers, they can form MX, in the 9-12% Cr steels, where M refers to vanadium or niobium, whereas X refers to nitrogen, carbon, or a combination of the two. This results in the following combinations; carbides (MC), nitrides (MN), or carbonitrides (M(C, N)). It was believed that the formation of vanadium carbide caused a strengthening of steels. Most recently, research also point outs that the vanadium of MX is rich in nitrogen as well. Niobium forms highly stable carbides, with a requirement to heat steel to temperatures way beyond normal austenitising temperatures in order to completely dissolve niobium carbides. The grain growth is restricted by un-dissolved niobium carbides during austenitization, therefore a refined prior austenite grain size is produced [15].

### 8.4 Effect of Boron and Phosphorus

Boron is a surface-active element with a low solubility in ferrite; it is also sometimes used to increase the ability to harden. Boron is added in several of the 9-12% Cr steels about 0.005-0.01%, because it has been reported that steel which contains boron, observes low coarsening rates and can segregate the surface of the $M_{23}C_6$, which in turn encourages the pinning of the sub grain boundaries. Phosphorus can also segregate to the surface of $M_{23}C_6$, and small quantities can be found in the Laves phase [7].

### 8.5 Effect of Manganese and Nickel

Manganese and nickel are austenite stabilizers, the principle reason for adding them to 9-12% chromium steels is to make sure that 100% austenite deformation occurs during the austenitization resulting in 100% of the steel becoming austenite steels when cooled. Nickel also raises the toughness of the ferritic/martensitic steels. However, nickel has been the most used to avoid δ-ferritic, and precipitate coarsening is accelerated by nickel, leading to a reduction in long-term creep strength. Another benefit of adding nickel is that it promotes the formation of $M_6C$ therefore destabilizing the $M_{23}C_6$, which stabilizes sub grain structure. Additionally, manganese and nickel have been observed to have a strong solid solution strength effect on iron. Manganese has same effect on carbide coarsening, but it is a weaker austenite stabilizer compared with nickel [7].

## 9. MICROSTRUCTURE

The high chromium (9Cr) family steels have a ferritic structure. This is achieved by quenching, austenitising and tempering at an intermediate temperature. After the high chromium (9-12%cr) ferritic steel is normalized (usually at 1040-1100 $^0$C) in an austenite regime, then it needs to be cooled to room temperature. Martensitic steel is transformed by a high chromium concentration (9-12%Cr) during air-cooling, then after a normalizing treatment, the steel has introduced into it, a martensitic lath structure with a high density of dislocations. After this, the steel is tempered to a low temperature. The martensitic lath structure becomes a sub grain structure during this tempering process [4].

Prior austenite grains are split into packets and moreover into blocks, which contains many elongated subgrains, and each has free dislocations at a high density within them. High chromium ferritic steels are tempered at lower temperatures (650-750 $^0$C) in order that the steam turbine maintains a higher yield stress. This high chromium ferritic steel thus comprises subgrains with high density of free dislocations. In contrast, high chromium steel, for pipes and boiler tubes, is tempered at higher temperatures (750-780 $^0$C) and it has a lower density of free dislocations. The precipitation distinguishes between pipe/tube and rotor steels, due to their various tempering temperature [19].

High chromium ferritic steel can be linked to three types of precipitates, MXc carbo-nitride, $M_{23}C_6$ carbide and $Fe_2M$ Laves phase. The MX carbo-nitrides are classified into NbC and VN, part of C atoms in NbC and N atoms in VN are substituted with N and C, respectively. MX particles consist of four types, firstly, primary NbX particles which remain after normalizing. The second

type is VX wings, which are evidenced on fine NbX particles during creep testing. The final two are the fine spherical NbX, and the fine platelet VX formed during the tempering process. All types of MX particles distribute uniformly within sub-boundaries and subgrains, except the primary NbX type.

Carbide $M_{23}C_6$ is the most abundant precipitate in 9-12% Cr ferritic steel. In P/T91 and P/T92 carbide $M_{23}C_6$ mostly appears as chromium rich because of the abundance of alloying elements within the steel matrix. This carbide could in theory form with its structure with Mo, Fe and Mo, however this is not generally observed. It has been found that elongation of $M_{23}C_6$ particles occurs in the former austenite grain boundaries and subgrain. It has also been shown that the 9Cr-1Mo steel creep strength is increased by $M_{23}C_6$ carbide, because the carbide works against martensite recovery, restricting the movement of subgrain boundaries under stress. These carbides have good thermal stability, which enables them to keep their deformation-resistance properties even when exposed to extremely high operating temperature.

The Laves phase ($Fe_2M$) involves an intermetallic compound: $Fe_2Mo$ and $Fe_2W$ in Mo and W containing steels, respectively. After tempering, it appears that it is only precipitates on sub-boundaries and grain boundaries during creep tests [15].

## 10. EFFECTS OF ION IRRADIATION

### 10.1 Irradiation creep

Irradiation creep is governed by different mechanisms as compared to those involved in thermal creep. It is noted that irradiation creep does not strongly depend on temperature. Whilst radiation raises the number of vacancies and self-interstitial, this increase does not lead to an acceleration of thermal creep. Temperature is not the only significant factor, because vacancies and self-interstitial formation is reliant mainly on atomic displacement, whereas thermal creep is more impacted by temperature. The irradiation creep rate at light water reactor cores can exceed over $10^{-6}$ $s^{-1}$ because of the core temperature; thermal creep is negligible.

The potential of interstitial loops nucleating on planes is accentuated by external stress applications. Vacancy loops will be more likely to nucleate on planes parallel to tensile stress - applied to solid material- whereas interstitial loops is more likely to nucleate on planes which are perpendicular to tensile stress. In each case, the preferential nucleation causes an increase in solid length in the direction in which stress is applied. This process is called the stress-induced preferential nucleation, SPIN radiation creep mechanism [21].

It is clear that creep appears in solid under- irradiation and stress as a result of several processes responsible for transferring the atoms from planes which are in parallel to the applied stress, across to a plane which is perpendicular to the applied stress. This process is known as stress-induced preferential absorption, whereby dislocations glide on planes inclined in the direction to which stress applied. The glide and climb dislocation occurs due to interstitial bias of the dislocation, this process being known as preferred absorption glide [21].

#### 10.1.1 Creep curve

Generally, creep properties are determined as described above in a circumstance where a constant stress or load is applied to a sample of metal, and the strain is measured as a function of time. Fig. 1 provides data about the variation of thermal creep with a time and creep curve showing the three stage of deformation; primary, secondary and tertiary. Firstly, the primary stage, which is also referred to as the transient stage, is the shortest lived stage, at the beginning of this stage the creep rate suddenly rises as a result of increasing dislocation density, and then the creep rate declines gradually, until it reaches a constant value and enters into the next regime. In the secondary or steady state stage, creep stays constant with increasing strain and time. Moreover, it is longest-lived time period of the three regimes and is represented by diffusion creep and the mechanism of dislocation. Creep rate during this stage does not depend on strain and time, but it is reliant only upon stress and temperature. The final stage is the tertiary stage, which may also be called the rupture stage. This stage is represented by damaging effects, including cavitations, necking and voiding. Producing void is significant and can lead in turn to crack deformation. As a result strain and stress increase further. This event will continue sufficiently long before the material may finally rupture [15].

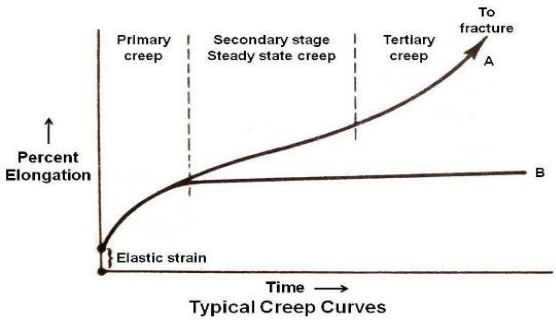


**Figure 1. This graph shows three steps of creep deformation [15]**

#### 10.1.2 Creep properties of P91 and P92 steels

Creep is an essential feature that must be factored into engineering design and applications that involve high temperature, namely piping within power plants, nuclear reactors, steam turbines and rocket engines. Creep can be defined as time-dependent deformation under continually stress or loads. Generally, creep happens at high temperature above about ($T/T_m > 0.3$) where $T/T_m$ ,

which is the melting point in Kelvin. Within this temperature range, atoms of materials gain enough mobility to develop a time-dependent change of the structure.

Creep properties are measured by constant stress creep testing and stress rupture testing. These can be achieved by applying a known formula to a sample of metal held at a fixed temperature. This type of test is simply continued until the sample fails. The stress rupture test can be defined as measuring strain failure (εf) and time fracture (Tf) at a fixed temperature and stress. These values are integral to the the creep test, along with a full creep strain time behaviour. The creep test requires expensive laboratory space, and is highly time consuming, taking up to about 30,000 hours. It provides vital information about creep fracture features of a particular metal and its creep behavior. For long-term predictions of creep life, an extrapolation theory is used [15]. It is important to understand creep properties in order to narrow down the selection of ferritic steels particularly P/T 91, 91 steel, in a fast reactor environment [4].

### 10.2 Void swelling

The high dose rate, typically high-energy neutron radiation, affects materials in fusion reactor or fast reactor, when vacancies and interstitial are produced because of the displacement of atoms from their matrix position by the radiation [7]. The improved conversion of microstructures, with temperature and dose rate, involves the agglomeration of interstitial and vacancies into dislocation loop and voids which causes swelling. Loop number density reduce and loop size also rise with increasing temperature and finally become unstable, Generally void swelling happens at a radiation dose above 10 dpa, and with a temperature range of 0.3-0.6 $T_m$ where $T_m$ is the melting point of materials. Moreover, it have been identified that void swelling relies on matrix structure lattice, in which the dose rate can produce excess defects. For ferritic/martensitic steels, at temperature about $500^0$C, an agglomeration of vacancies can lead to void swelling [6].

Ferritic steels became of interest to physicists in relation to fusion and fast reactors because extensive studies found that the ferritic steels have high void swelling resistance compared to austenitic stainless steels [22].Furthermore, it has been observed that 9Cr-1Mo steels have low swelling rates, even in events of high radiation, about 200dpa. For this reason, the ferritic steels have been chosen for clad and wrapper application within nuclear reactors, whereas for austenitic steels, the radiation threshold is nearer to 80 dpa [6]. Void swelling can be measured by determining the volume conversion of material before radiation and after radiation. From this, the rate of conversion in the volume of material can be identified. Moreover, the radiation-induced transformation of void is observable using a transmission electron microscope (TEM).

### 10.3 Irradiation embrittlement

Radiation embrittlement occurs during irradiation due to increasing the ductile to brittle transition temperature (DBTT). It has been observed that irradiation hardening causes the DBTT temperature to increase thus producing embrittlement.

With ferritic/martensitic steels, body centered materials, a large increase in DBTT temperature can occur at low temperature (<0.3 Tm) and low dose rate about 1dpa (displacement per atom) because of radiation hardening. It has been noted that a minimum working temperature to prevent embrittlement in ferritic-martensitic steels is 473-523 K. That said, the upper limit temperature can be controlled by four deferent mechanisms; void swelling, thermal creep, high temperature helium embrittlement and compatibility. Void swelling and thermal creep have been discussed above; high temperature helium embrittlement will be discussed in 10.4.

Fig. 2 provides information about the evaluation of ferritic steels' embrittlement behaviour, relating to different chemical compositions. It indicates that the shift in DBTT caused by irradiation varies, under radiation the focus on concentration on chemistry is around 9% Chromium is clearly based on a minimum observation shift in DBTT, almost around this chemical composition. Although, corrosion-resistant steels can be improved by increasing chromium and it encourages reprocessing, however the rate of chromium contents need to be chosen with a careful balancing these requirements. It has been found that addition chemical compositions such as copper, vanadium, silicon, aluminum, phosphorous would rise the DBT temperature; by contrast, sulphur decreases the upper shelf energy.

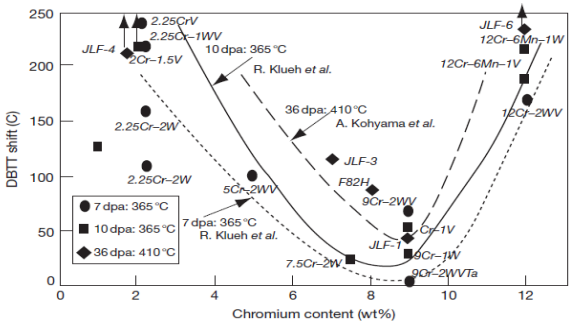


**Figure 2. Shows radiation-induced DBTT shift as a function of chromium content [7]**

It is shown from Fig. 2, that the 9Cr-1Mo steels has a lower shift (nearly 54 K) in DBT temperature as compared to the 12Cr steels (125K).
Hence, the swelling resistance is almost nil for 12Cr steels, and 9Cr steel is less prone to embrittlement in comparison to 12Cr steels [4].

It has been observed that irradiation hardening saturates at around 10 dpa, and it has been seen that the shift in

DBTT because of irradiation saturates at around 10 dpa. In Fig. 3, by conducting Charpy tests, it can be seen that the shift of DBTT at 10 dpa is equivalent to the DBTT shift at 17dpa. It is also important to note that irradiation temperature and the extent of shift inverse to each other [7, 23].

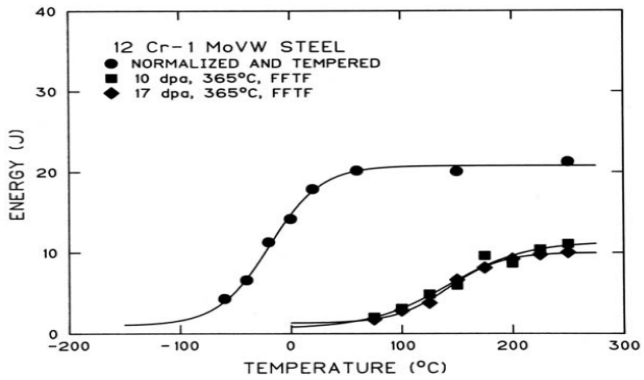


**Figure 3. Charpy curves for Sandvik HT9 steels before and after irradiation to 10 and 17 dpa at 365 c in FFTF [4]**

### 10.4 Helium Embrittlement

Helium embrittlement occurs after nickel undergoes an (n, alpha) reaction at an elevated temperature (close to or above 0.5Tm), and when enough levels of helium are generated by mechanical stress as applicable during irradiation and other nuclear reactions. The transformation of grain boundary bubbles to voids induces intergranular fracture, which in turn leads to breakaway cavity coalescence, rupture and growth in the presence of mechanical stress. During high temperature irradiation, the migration of helium is induced to the grain boundaries by the application of tensile stress, and large cavities may be formed. It has been observed that when the applying stresses are absence, the helium bubbles are divided throughout the metal [24].

The observed tensile ductility, due to helium embrittlement, reduces with decreasing stress and reducing strain rate, which indicates its crucial exposure time at elevated temperature. It has been found that ferritic-martensitic steels demonstrate better resistance to grain boundary helium cavity growth and formation in comparison with austenitic stainless steels. This is because of several factors, firstly, ferritic steels have lower matrix strength compared to austenitic steels, and another factor is that helium bubbles' conversion to voids has a potentially larger critical radius within ferritic steels. Finally, there is an impact from the efficient trapping of helium inside the ferritic steels grain interior, by precipitates and other properties [24].

There is a large volume of published studies discussing the importance of the helium effect for some systems, for example, fusion reactors that produce high-energy neutrons. The 14 MeV neutrons are produced by D-T fusion, and these neutrons will generate an (n, alpha) reaction in nearly all common structural elements namely ferritic steels, but, in the absence of nickel, helium production rates are lower. In the martensitic steels, a number of techniques have been used to produce helium in fusion reactors; one of the most significant ways is doping with natural nickel for 9Cr and 12Cr steels, and another way is the use of isotopically-separated nickel to discriminate against the nickel effect as opposed to the helium effect. For example $Ni^{59}$ has been used to generate helium, whereas, $Ni^{60}$ has been used for control.

The 9-12 Chromium steels have nickel as one of its chemical composition. The helium generated enhances the growth rate of voids and promotes grain boundary crack growth, leading to embrittlement. This phenomenon is significant in fusion reactors. Although in fact this type of embrittlement is of little concern in light water reactors and fast reactors, including the Generation IV designs [25].

### 10.5 Irradiation hardening

The phenomenon, Irradiation hardening happens because an increase in the yield strength of a material which leads to a decrease in ductility. The effect of radiation depends on temperature and usually occurs at radiation temperature ($T_{irr} < 0.3\ T_m$) where $T_m$ is the melting point for materials. Irradiation hardening can be observed over a minimum radiation of 0.1 dpa [4].

A metal irradiation causes strengthening. During irradiation, the number density of defects such as voids precipitates and loops, rises drastically. Therefore the mobile dislocations move in two ways: source hardening and friction hardening. Firstly, source hardening can be defined as the increase in stress required to bring dislocation moving on its glide plane. The required stress that must be applied to launch a dislocation into its slip plan is known as unlock stress or unpinning stress. Secondly, friction hardening refers to obstacles that generate resistance from mobiles to motion. It is essential to recognise that true distinction between friction and source hardening is unclear, because all the characteristics of deformation are produced by lattice hardening, and they have been distributed to source hardening. The source length that produces critical shear stress, is greater than the distance between defect clusters. It leads to a loss of distinctions, and therefore, the source cannot be operated without interference from the lattice clusters [21].

It has been observed that there is a strong link between the extent of irradiation hardening and irradiation temperature as shown in Fig. 4. The figure also shows yield strength as a function of radiation against temperature. It can be seen from the graph [26], that yield strength dips to the lower spectrum at high irradiation temperatures, whereas it reaches a high point at lower irradiation temperatures. The temperature reliance of irradiation temperature exists because temperature dictates the nature of the defects produced

by radiation, which in turn directs the extent of hardening. Irradiation hardening has been observed to saturate at 10 dpa.

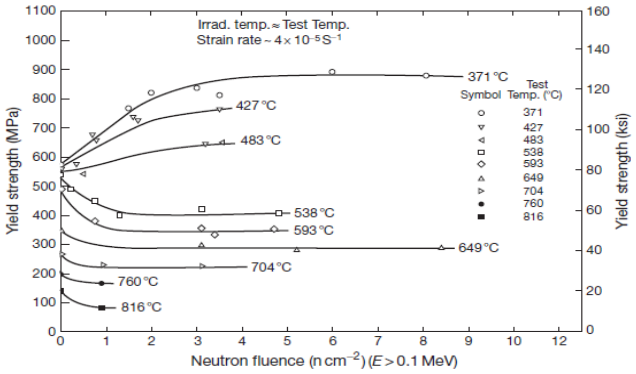


**Figure 4. Yield strength of 20% cold-worked type 316 stainless steel irradiated in the EBR-II [25]**

The radiation effect on the tensile behaviour of the 9-12% Cr ferritic/martensitic steels, namely T/P91 and T/P92 steels, is dependent upon temperature. Irradiation hardening occurs at exposure temperatures above, up to 425-450 C. This is because the high density of tangles and dislocation loops which form from displacement damage, throughout with irradiation- induced precipitates change under these conditions [7]. Therefore ductility decreases and yield strength increases. It has been found that the amount of hardening does not change when T/P91 and T/P92 steels are irradiated at 390C to about 23 dpa. It is observed that hardening varies according to how far there is saturated rising fluence; hardening saturation occurs at about $400^0$ C to 10 dpa, whereas for lower temperature greater fluence are required. However, properties are not generally altered by irradiation temperatures up to 425-450 compared to thermally aged and unirradiated samples, although such temperature may create a softening, depending on fluence. Since irradiation hardening leads to a decrease ductility, this can therefore be translated as causing an increase embrittlement [3].

## 11. CONCLUSION

This review article has looked at the context and background to mechanics and properties of ferritic-martensitic steels, and to highlight the development of ferritic- martensitic steels for nuclear reactors. After that, the focus was the effects of radiation on mechanical properties.

This review article will be important for future work around energy and ion irradiation. It would be important to test at higher levels – or lower levels- energy, to explore additional effects of high and low irradiation on P91 and P92 steel. Also, it may important to perform a creep test for P91 and P92 during irradiation at different temperatures, and at different radiation energy levels.

## REFERENCES

[1] Smith, R., Fast reactor progress—slow but sure, Progress in Nuclear Energy. 1987, vol. 20, 2, pp. 71-88.

[2] Kittel, J., Frost, B., Mustelier, J., Bagley, K., Crittenden, G., and Van Dievoet, J., History of fast reactor fuel development, Journal of nuclear materials. 1993, vol. 204, pp. 1-13.

[3] Klueh, R., and Nelson, A., Ferritic/martensitic steels for next-generation reactors, Journal of Nuclear Materials. 2007, vol. 371, 1-3, pp. 37-52.

[4] Raj, B., and Vijayalakshmi, M., Ferritic steels and advanced ferritic–martensitic steels, Comprehensive Nuclear Materials. 2012, vol. 4, pp. 97-121.

[5] Klueh, R., Gelles, D., and Lechtenberg, T., Development of ferritic steels for reduced activation: the US program, Journal of Nuclear Materials. 1986, vol. 141, pp. 1081-1087.

[6] Klueh, R., and Harries, D., High Chromium Ferritic and Martensitic Steels for Nuclear Applications. West Conshohocken, PA : ASTM International.: 2001; p 221.

[7] Klueh, R., Elevated temperature ferritic and martensitic steels and their application to future nuclear reactors, International Materials Reviews. 2005, vol. 50, 5, pp. 287-310.

[8] Klueh, R., Hashimoto, N., and Maziasz, P., Development of new nano-particle-strengthened martensitic steels, Scripta Materialia. 2005, vol. 53, 3, pp. 275-280.

[9] Klueh, R., Ehrlich, K., and Abe, F., Ferritic/martensitic steels: promises and problems, Journal of nuclear materials. 1992, vol. 191, pp. 116-124.

[10] Conn, R., Bloom, E., Davis, J., Gold, R., Little, R., Schultz, K., Smith, D., and Wiffen, F., Panel report on low activation materials for fusion applications, Journal of Nuclear Materials. 1983, vol. 122, pp. 17–26.

[11] Chen-Yih, H., and Lechtenberg, T. A., Microstructure and mechanical properties of unirradiated low activation ferritic steel, Journal of Nuclear Materials. 1986, vol. 141, pp. 1107-1112.

[12] Dulieu, D., Tupholme, K., and Butterworth, G., Development of low-activation martensitic stainless steels, Journal of Nuclear Materials. 1986, vol. 141, pp. 1097-1101.

[13] Kayano, H., Kimura, A., Narui, M., Kikuchi, T., and Ohta, S., Effects of small changes in alloy composition on the mechanical properties of low activation 9% Cr-2% W steel, Journal of nuclear materials. 1991, vol. 179, pp. 671-674.

[14] Abson, D., Rothwell, J., and Cane, B. In Advances in welded creep resistant 9–12% Cr steels, Proc. 5th Int. EPRI Conf. on 'Advances in materials technology for fossil power plants, 2007; 2007.

[15] Baral, J. Creep characterization of Boron added P91 steel in the temperature range 600-650 degree C. National Metallurgical Laboratory (NML), 2011.

[16] Blum, R., Hald, J., Bendick, W., Rosselet, A., Vaillant, J., Fynsvaerket, O., Elsam, F., and Mannesmann Forschungsinstitut, D., Newly developed high-temperature-resistant ferritic-martensitic steels from the USA, Japan,

and Europe. Neuentwicklungen hochwarmfester ferritisch-martensitischer Staehle aus den USA, Japan und Europa, VGB Kraftwerkstechnik. 1994, vol. 74 (8), pp. 641-652.

[17] Canonico, D., Thick-walled pressure vessels for energy systems, Ferritic Steels for High-Temperature Applications. 1981, vol., pp. 31-41.

[18] Sikka, V., Ward, C., and Thomas, K., Modified 9 Cr--1 Mo Steel--an Improved Alloy for Steam Generator Application, Ferritic Steels for High-Temperature Applications. 1981, vol., pp. 65-84.

[19] Von Hagen, I., and Bendick, W. In Creep resistant ferritic steels for power plants, International Symposium on Niobium 2001, 2001; 2001; pp 753-776.

[20] Viswanathan, R., and Nutting, J., Advanced heat resistant steels for power generation. IOM Communications: 1999.

[21] Was, G. S., Fundamentals of radiation materials science: metals and alloys. Springer: 2016.

[22] Little, E. A., and Stoter, L., Effects of Irradiation on Materials: Eleventh Conference, ASTM STP 782, eds, HR Brager and JS Perrin, American Society for Testing and Materials, Philadelphia. 1982, vol., pp. 207-233.

[23] Kohyama, A., Hishinuma, A., Gelles, D., Klueh, R., Dietz, W., and Ehrlich, K., Low-activation ferritic and martensitic steels for fusion application, Journal of Nuclear Materials. 1996, vol. 233, pp. 138-147.

[24] Zinkle, S., 1.03-Radiation-Induced effects on microstructure, Comprehensive Nuclear Materials. 2012, vol. 1, pp. 65-98.

[25] Grossbeck, M. L., Effect of radiation on strength and ductility of metals and alloys, Comprehensive Nuclear Materials. 2012, vol. 1, pp. 99-122.

[26] Zinkle, S. J., and Was, G., Materials challenges in nuclear energy, Acta Materialia. 2013, vol. 61, 3, pp. 735-758.

The Scientific Bulletin of VALAHIA University
MATERIALS and MECHANICS –Vol. 17, No. 16

DOI 10.2478/bsmm-2019-0004

# SPECIAL REFRACTORIES RESISTANT TO THE MELT METALS AND SLAGS ATTACK

**Nicolae ANGELESCU, Dan Nicolae UNGUREANU*, Florin TOMA**

Valahia University of Targoviste, Faculty of Materials Engineering and Mechanics, 13 Aleea Sinaia Street, Targoviste, Romania

E-mail: * danungureanu2002@yahoo.com

**Abstract:** *The paper is an attempt to present and evaluate of the some monolithic refractory materials, originating from our research activity, with potential to be used as the thermoprotective linings for the nonferrous metals and ferrous alloys manufacturing installations in foundries and steelworks.*

**Keywords:** Spinel, refractory masses, refractory concrete, vacuum and air induction furnaces, iron, steel, non-ferrous metals

## 1. INTRODUCTION

The refractory products used as a hot face lining in the induction furnaces for cast iron, steel or non-ferrous metals melting, holding or pouring are, most of them, unshaped products. Their nature is diverse, depending on the treated alloy composition: quartz-like, silico-aluminous, high-aluminous, spinellic, magnesitic etc. [1-4]. For better fitting to the purpose they are meant for the linings should have some well defined properties; thermal shock resistance, compactness resistance at melt metal and slag attack, strength, low thermal conductibility, refractoriness etc. The present paper intends to describe some products obtained as a result of the research works in the above described realm (Table 1).

## 2. EXPERIMENTAL PROCEDURE

The masses shown are compositions based on corundum or tabular alumina, fused and/or sintered magnesite and spinel (Table 2). It may be seen that both spinel and alumina are characterized by a set of superior properties. Magnesite is also of a high interest from this point of view if we don't take into account its thermal expansion coefficient, since it is characterized by high refractoriness and allows desulphurization during the very making process.

When preparing the lining materials either chemical-ceramical or chemical-hydraulic binders or ceramic hardening agents were used, correlated sometimes with organic substances. There are also shown some data concerning compressive strength (Sc), porosity (P) and apparent density.

**Table 1. Special Monolithic Refractories and their Properties**

| Product name | Grain size [mm] | Type set | Oxide composition | Refractority, [$^0$C] | Application | Utilization |
|---|---|---|---|---|---|---|
| MI90A | 0-5 | Chemical ceramic | 90% $Al_2O_3$<br>6% $SiO_2$<br>2% $P_2O_5$ | 1880 | Wet ramming | Channel induction furnaces for cast iron holding: vessel area in contact with melt iron |
| MI85B | 0-6 | Chemical ceramic | 85% $Al_2O_3$<br>9% $SiO_2$<br>1.5 % $P_2O_5$ | 1850 | Wet ramming | Channel induction furnaces for cast iron holding: vessel area above slag line |
| MI90C | 0-3 | Chemical ceramic | 90% $Al_2O_3$<br>6% $SiO_2$<br>1.5% $P_2O_5$ | 1880 | Wet ramming | Induction furnace for aluminium melting |
| MM95 | 0-5 | Chemical ceramic | 95%MgO<br>1.5% $SiO_2$<br>2.3% $Cr_2O_3$ | > 1880 | Wet ramming | Induction furnace for air steel melting |
| BI97 | 0-6 | Air set chemical hydraulic | 96.5%$Al_2O_3$<br>1.1% CaO<br>2.2% $Cr_2O_3$ | > 1880 | Casting vibration | Channel induction furnaces for cast iron holding or pouring: inductior and vessel – Cu and Cu alloys induction furnace |
| MSU70 | 0-5 | Heat set ceramic | 67-70% MgO<br>26-30% $Al_2O_3$ | > 1880 | Dry ramming | Air or vacuum coreless induction furnaces for carbon and alloy steel |

| | | | | | | |
|---|---|---|---|---|---|---|
| MSU24 | 0-5 | Heat set ceramic | 24% MgO 73% $Al_2O_3$ | > 1880 | Dry ramming | Air or vacuum coreless induction furnaces for carbon and alloy steel |

**Table 2. The Properties of Raw Materials**

| Raw material | Melting temperature [$^0$C] | Thermal expansion coefficient at 20-1000$^0$C x $10^{-6}$ [cm/cm·$^0$C] | Thermal conductibility at 1000°C, [kcal/mh$^0$C ] | Desulphurizaton |
|---|---|---|---|---|
| Alumina $Al_2O_3$ | 2020 | 8.8 | 1.8 | no |
| Magnesite MgO | 2800 | 14.0 | 3.0 | yes |
| Spinel $MgO·Al_2O_3$ | 2110 | 7.6 | 1.7 | yes |

## 3. RESULTS AND DISCUSSIONS

The use of some chemical binders allows the achievement of some compact and high resistance structures as a result of the chemical reactions acid-oxide type between binder and aggregate with the formation of new compounds (for example, aluminium hydrophosphates in gel condition or with crystalline and polycondensate structures in case of MI90A, MI85B and MI90C masses or hydrated magnesium chromates for MM95 mass with chromic anhydride) which binders the system in a monolithic whole. These compounds undergo some transformations under heat treatment conditions: aluminium hydrophosphates dehydration, and variscite ($Al(PO_4)·2H_2O$) formation processes followed by berlinite ($AlPO_4$) formation and of hydrated magnesium chromate ($MgO·Cr_2O_3$) formation processes [5]. $MgO·Cr_2O_3$ is a product characterized by a good resistance to metallic melts and slag attack. Other phenomena may also take place, for example oxygen release from the binder matrix of magnesitic mass: $2CrO_3 \rightarrow Cr_2O_3 + 3/2O_2$ [5]. These processes lead to textural-structural modifications which, correlated with ceramic bindering influence, explain mechano-structural properties variation noticed at the above mentioned products heating (Table 3).

**Table 3. The some important Properties of Refractory Materials[x)]**

| Product name | Temperature, [$^0$C] | 110 | 400 | 600 | 800 | 1000 | 1200 | 1400 | 1500 | 1750 |
|---|---|---|---|---|---|---|---|---|---|---|
| MI90A | Sc, [daN/cm$^2$] | 360 | 470 | 420 | 408 | 440 | 450 | 490 | 500 | - |
| | P, [%] | 17 | 18 | 19 | 20 | 21 | 21 | 20 | 20 | - |
| MI85B | Sc, [daN/cm$^2$] | 342 | 455 | 388 | 396 | 406 | 430 | 470 | 486 | - |
| | P,[%] | 18 | 19 | 21 | 20 | 22 | 23 | 22 | 22 | - |
| MI90C | Sc, [daN/cm$^2$] | 300 | 420 | 360 | 340 | 355 | 360 | 400 | 450 | - |
| | P, [%] | 18 | 19 | 20 | 20 | 21 | 21 | 23 | 23 | - |
| MM95 | Sc, [daN/cm$^2$] | 410 | 332 | 245 | 205 | 188 | 165 | 180 | 200 | 350 |
| | P, [%] | 16 | 18 | 20 | 21 | 21 | 21 | 21 | 20 | 19 |
| BI97 | Sc, [daN/cm$^2$] | 330 | 324 | 320 | 270 | 270 | 300 | 430 | 540 | 650 |
| | P, [%] | 15 | 16 | 17 | 18 | 18 | 18 | 20 | 21 | 22 |

[x)] Sc = Compressive Strength, P = Porosity

The use of chromic anhidride leads - under the conditions of a relatively low aluminous cement content to obtaining some superaluminous products, type BI97, very refractory, having a good compactness and high mechanical strength (Table 3) as a result of binder influence on structure porosity (Fig.1), of modifications implied in the hardening process development, in the morphology of cement hydration neoformations and of the interaction products resulting from its activity as a chemical binder [6 - 21]. The well-known resistance loss within the critical temperature range of refractory concretes which, in case of those with an ordinary cement dosage, may reach to half of the initial value, is much diminished in case of BI97 concrete, under the conditions of keeping a rather low porosity value. The initial mecano-structural characteristics as well as those within the high heat treatment temperature range for HI97 concrete are quite good.

The presence of special sintering agents and of unavoidable impurities, correlated, sometimes, with magnesitic spinel formation leads, at dry MSU70 and MSU24 masses sintering, to a rather thin hard layer formation (Table 4) when getting into contact with the

metal bath. The material will remain in a powder condition near the hardened layer. The sintered layer seal the crucible and will undertake the mechanical stress which this is subject to, while the nonsintered on will solidify the metallic infiltrations which might take place through the hardened layer at the lining repeated cooling and heating, as well as in undertaking the volume fluctuations appearing in the lining during the equipment operation.

The formation of the sintered stratum is the result of a ceramic type hardening taking place during the first heat melting at the highest temperature. During furnace functioning sintering propagates from the hot face to the coil, that is why it is very important to demolish lining before the powder layer will sinter completely.

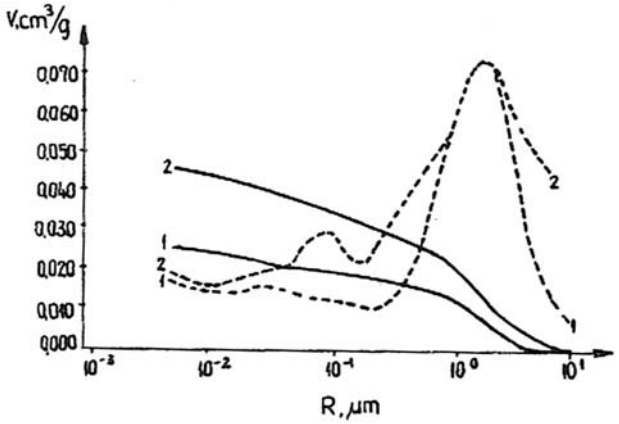


**Figure 1. Distributive porosity ( __ integral curves, _ _ differential curves) of refractory concretes hardened for 3 days: 1 concrete with chromitic binder, 2 concrete without chromitic binder**

**Table 4. Properties of Dry Refractory Masses with Ceramic Hardening**

| Mase type | Impurities, [%] $SiO_2$ CaO $Fe_2O_3$ | Temperature at wich ceramic binding begins [$^0$C] | Apparent density at 1400$^0$C [g/cm$^3$] | Apparent porosity at 1400$^0$C [%] |
|---|---|---|---|---|
| MSU70 | 1.2 1.5 0.9 | 1200 | 2.86 | 19 |
| MSU24 | 1.1 0.7 0.45 | 1000 | 2.94 | 20 |

## 4. PRACTICAL APPLICATIONS

The refractory products described above have been used in channel and coreless induction furnaces with various capacities and building patterns. Masses MI90A and MI85B are used at lining the iron channel furnace vessels type Independenta Sibiu of low and medium capacity, type Otto Yunkers of 9 t, type ASEA of 7 and 21 t and type Brown - Bovery of 55 t whore the lining life may reach 2.5 years.

MI90C sortiment is used for lining aluminum melting induction furnaces with capacities reaching 3 t. BI97 concrete is successfully used at lining some channel furnace components which, because of their more complicated shape, cannot be lined by ramming. It is used for inductors of all capacities of Independent Sibiu furnaces, ASEA furnaces of 5, 7 and 15 t and Elin Union furnaces of 7 t, when the medium life is of 7 months reaching sometimes to 1.5 years. BI97 is also used for lining the vessels of Independenta Sibiu of high capacity, Elin of 7 t and ASEA of 5 t and we obtained lifes of 1-1.2 years.

Very good results were obtained using BI97 concrete as a wear layer at the induction furnaces for Cu and Cu-alloys melting or holding. Magnesitic mass MM95 was used with good results for lining coreless induction furnaces for carbon steel with capacities up to 1t.

The refractory linings for vacuum induction furnaces are subject to very severe functioning conditions imposed both by the necessity of obtaining very homogeneous high purity compositions and by the equipment functioning safety requirements. The use of MSU24 mass at lining such installations, for making highly-alloyed steels at 1650$^0$C, lead to obtaining a very good durability. Good results were also obtained with MSU70 mass, but this one is currently used at lining furnaces for air steel melting. These are also the results of a good behavior at melting attacks as can be seen from the comparative analyses with traditional products used to this purpose - Table 5.

Irrespective of the lining nature, it could be seen that furnaces functioning in the cleanest possible conditions (slag should be removed and unnecessary over-heatings should be avoided) lead to the increase of their functioning life.

**Table 5. Comparative values of the wetting point for two refractory masses used for the same purpose**

| Product | Wetting point in case of a refractory steel at $1550^0$C | Wetting point in case of a stainless steel at $1600^0$C |
|---|---|---|
| MSU70 | $130^0$-$140^0$ | $133^0$-$136^0$ |
| Sofrem AM/BS (France) | $116^0$-$148^0$ | $123^0$-$139^0$ |

## 5. CONCLUSIONS

From what we have already shown the following conclusions may be drawn:

1. There is a wide range of refractory products made for induction furnaces lining (ramming, castable or dry masses) with various compositions: high-aluminous, magnesitic, magnesio-spinellic or alumino-spinellic.
2. The use of various binding system: chemical-ceramic, chemical-hydraulic and ceramic.
5. The products described are used with good results, according to their nature, at coreless and channel induction furnaces for carbon steel and high alloy steels, for cast iron or non-ferrous metals.

## REFERENCES


[1] Angelescu N., Szabo A. - Cercetari Metalurgice. ICEM, Bucharest, 1978, p. 625.

[2] Belon L., Guerin M. - Hommes et Fonderie, No.122, 1982, p. 23.

[3] Chesters J.H. - Refractories for iron and-steelmaking, The Metals Society, London, 1974.

[4] Dragomir C., Angelescu N., Szabo A., Deica N., Dragoman I - Cercetari Metalurgice. ICEM, Bucharest, 1978, p. 619.

[5] Teoreanu I., Ciocea N. - Lianţi, mase şi betoane refractare, Ed. Tehnică, Bucureşti, 1977.

[6] Teoreanu,I., Angelescu N. - Mat.Constr., Vol. 10, No.1, 1980, p. 31.

[7] Angelescu, N., Ionita, C., Bratu, V. - Structural and mechanical characterization of high alumina additivated cement based on high refractory mineralogical compounds. Construction Materials and Structures. Pages 113 – 120. Edited by Ekolu, S,O., Dundu, M., Gao, X., IOS Press, 2014, doi: 10.3233/978-1-61499-466-4-113. Conference: 1st International Conference on Construction Materials and Structures, Johannesburg, South Africa, November 24 – 26, 2014.

[8] Angelescu, N., Amziane, S., Ionita C., Ion, I., Stanciu, D. - Concretes for Special Applications. Advanced Materials Research, Trans. Tech. Publications, Switzerland, Vols. 479-481, pp 595-600, 2012.

[9] Angelescu, N., Amziane, S., Ionita C., Ion, I., Stanciu, D. - Special and New Monolithics. Advanced Materials Research, Trans. Tech. Publications, Switzerland, Vols. 479-481, pp 362-365, 2012.

[10] Angelescu, N., Muntean, M., Ionita, C. - Noi betoane refractare speciale. Revista Romana de Materiale, 40 (3), pag. 193-202, 2010.

[11] Angelescu, N., Barosso, J., Surugiu, G., Paunescu, L. – Considerations Regarding the Possibility of Heat Losses Reducing through Furnace Lining in Accordance with Actual Trends of Refractory Lining Structure Optimization. Metalurgia International, Vol. XV(12), p. 23-28, 2010.

[12] Rebouillant L, Rigaud M, Ildefonse J P, Gabis V, Dubreuil P, and Daniellou P: Cement-free Castables with Micronized Andalusite. 9th SIMCER, 5-8 October, 1998.

[13] Teoreanu, I., Angelescu, N. - Hardening Processes for Some Refractory Binding System - Kinetic Considerations and Mechanisms. The 9th International Congress on Chemistry of Cement, New Delhi, India, vol. III, pp. 351-357, 1992.

[14] Stancu, C., Angelescu, N., Muntean, M - The influence of mineralogical composition of high alumina cement on its physical - mechanical properties. Calcium Aluminate Cements: Proceedings of the Centenary Conference, Avignon, France, 19 May – 21 May 2014, p. 364

[15] Angelescu, N. - A New Binding System for Concrete. Proceed. of 6th International Conference of Concrete Technology, October, Amman, Iordania, Vol.1, 213-222, 2002, ISBN 9957-31-000-3.

[16] Angelescu, N., Muthu, K. U., Ionita, G., Nicolae, A., Nicolae, M. - Theoretical Fundaments and Applications about Special Additivated Concretes, Proceedings of International Conference on Construction and Building Technology, "Emerging Technology in Construction Materials", ICCBT 2008, pg, 165 – 176, Kuala Lumpur, Malaezia, Iunie, 2008.

[17] Teoreanu, I., Angelescu, N. - The Influence of Some Organic Additives on Refractory Aluminous Cement Hydration. Il Cemento (Italia), vol. 83, pp. 191-198, 1986.

[18] Angelescu, N., Muthu, K. U., Ionita, G., Nicolae, A. - Use of Special Refractory Concretes, Proceedings of 8th International Conference on Concrete Technology, pg. 215 – 225, Hammamat, Tunisia, November, 2007.

[19] Angelescu, N., Dobrea, M. - A New Refractory Concrete for Casting Ladles. Proc. of the 7th NCB International Seminar on Cement and Building Materials, November, New Delhi, India, 2000.

[20] Angelescu, N., Ionita, G. - Aluminous Cement Special Concrete. Proceedings of Conference on Applications & Marginal Materials in Construction – ARMICON 2006. Bangalore, India, 2006.

[21] Angelescu, N., Ionita, G., Nicolae, A. - New Special Concretes, World of Coal Ash (WOCA 2007), Covington, Kentucky / The Southern of Cincinnaty, SUA, May 7-10, 2007.

The Scientific Bulletin of VALAHIA University
MATERIALS and MECHANICS –Vol. 17, No. 16

DOI 10.2478/bsmm-2019-0005

# NUMERICAL MODELING OF THE DYNAMICS OF THE DRAWN WHEEL. CASE OF ROLLING WITHOUT SLIDING

**Vladimir Dragoş TĂTARU[1*], Mircea Bogdan TĂTARU [2**]**

[1]Valahia University of Targoviste, Faculty of Materials Engineering and Mechanics, 13 Aleea Sinaia Street, Targoviste, Romania, [2]University of Oradea

E-mail: *vdtataru@gmail.com, **btataru@uoradea.ro

**Abstract:** *When the dynamic study of a solid rigid body subjected to links is wanted to be performed, the main difficulty is that the differential equations of motion contain in their structure the constraint forces which are unknown. Therefore it is necessary to remove them from the differential equations that describe the motion of the rigid body. The case of a wheel climbing on an inclined plane has been presented in this paper. It is considered that the wheel is rolling without sliding on an inclined plane.*

**Keywords:** *numerical modeling, dynamics, drawn wheel, rolling, sliding*

## NOMENCLATURE

$\overline{F}$ -active force acting upon the wheel

$\overline{F_r}$ -viscous damping force

$\overline{M_r}$ -viscous damping couple

$\overline{M_f}$ -torque of the rolling friction

$s$ -rolling friction coefficient

$\overline{T}$ -sliding friction force

$\overline{N}$ -normal reaction force

$\overline{G}$ -force of gravity

$\alpha$ -inclination angle of the plane

$R$ -radius of the wheel

$C_1$ -mass center of the wheel

$m_1$ -mass of the wheel

$J_{z_1}$ -inertia axial moment relative to $O_1z_1$ axis

$v_{O_1x_1}$ -velocity of the $O_1$ point projection on the $O_1x_1$ axis

$v_{O_1y_1}$ -velocity of the $O_1$ point projection on the $O_1y_1$ axis

$\omega_{z_1}$ -angular velocity of the wheel projection on the $O_1z_1$ axis

$T_1(O_1x_1y_1z_1)$-body fixed reference frame

$T(Oxyz)$-fixed reference frame

$O_1x_1, O_1y_1, O_1z_1$-axis of the body fixed reference frame

$Ox, Oy, Oz$ -axis of the fixed reference frame

$\varphi_1$ -self-rotation angle of the wheel

$c_t$ -viscous damping coefficient corresponding to the translational movement

$c_r$ -viscous damping coefficient corresponding to the movement of rotation

$\overline{k}$ -unit vector of the Oz axis

sgn -sign function

$T$ -denotes the transposition matrix operation

## 1. INTRODUCTION

We will consider a wheel supported on an inclined plane and acted upon by a system of forces and couples as it is shown in the figure below (Fig.1). We aim to perform the dynamic survey of this wheel namely its motion under the action of the given system of forces.

$$\overline{M}_f = -s \cdot N \cdot \mathrm{sgn}(\omega_{z_1}) \cdot \overline{k}$$

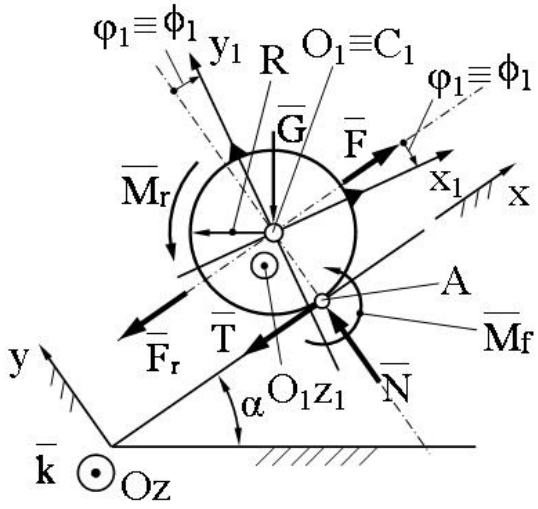


**Figure 1. Drawn wheel**

## 2. EQUATIONS OF MOTION ESTABLISHING

The differential equations of motion of the drawn wheel may be written in projections on the axis of the body fixed reference frame in the following matrix form [1-17]:

$$\mathbf{M}_{O_1} \cdot \dot{\mathbf{v}}_1 = \mathbf{Q}_g + \mathbf{Q}_a + \mathbf{Q}_r + \mathbf{Q}_c \quad (1)$$

$$\dot{\mathbf{x}}_1 = \mathbf{R}_1 \cdot \mathbf{v}_1 \quad (2)$$

$$\dot{\mathbf{v}}_1 = \left[\dot{v}_{O_1x_1} \;\vdots\; \dot{v}_{O_1y_1} \;\vdots\; \dot{\omega}_{z_1}\right]^T \quad (3)$$

$$\mathbf{v}_1 = \left[v_{O_1x_1} \;\vdots\; v_{O_1y_1} \;\vdots\; \omega_{z_1}\right]^T \quad (4)$$

$$\dot{\mathbf{x}}_1 = \left[\dot{x}_{O_1} \;\vdots\; \dot{y}_{O_1} \;\vdots\; \dot{\varphi}_1\right]^T \quad (5)$$

$$\mathbf{M}_{O_1} = \left[\begin{array}{c:c:c} m_1 & 0 & 0 \\ \hdashline 0 & m_1 & 0 \\ \hdashline 0 & 0 & J_{z_1} \end{array}\right] \quad (6)$$

The action of active forces on a solid rigid body can be completely characterized by its torque. In the case under consideration the torque of active forces relative to the point $O_1$, in projections on the axis of the body fixed reference frame $T_1(O_1x_1y_1z_1)$ may be written as follows:

$$\mathbf{Q}_a = \mathbf{R}_1^T \cdot \mathbf{Q}_a^0 \quad (7)$$

In the relationship (7) the quantities involved have the following expressions:

$$\mathbf{R}_1 = \left[\begin{array}{c:c:c} \cos(\varphi_1) & -\sin(\varphi_1) & 0 \\ \hdashline \sin(\varphi_1) & \cos(\varphi_1) & 0 \\ \hdashline 0 & 0 & 1 \end{array}\right] \quad (8)$$

$$\mathbf{Q}_a^0 = \left[-m_1 \cdot g \cdot \sin(\alpha) + F \;\vdots\; -m_1 \cdot g \cdot \cos(\alpha) \;\vdots\; 0\right]^T \quad (9)$$

The torque of the resistant forces relative to the point $O_1$, in projections on the axis of the body fixed reference frame $T_1(O_1x_1y_1z_1)$ may be written as follows:

$$\mathbf{Q}_r = -\mathbf{R}_1^T \cdot \mathbf{C} \cdot \mathbf{R}_1 \cdot \mathbf{v}_1 \quad (10)$$

In the relation (10) the matrix $C$ has the following expression:

$$\mathbf{C} = \left[\begin{array}{c:c:c} c_t & 0 & 0 \\ \hdashline 0 & c_t & 0 \\ \hdashline 0 & 0 & c_r \end{array}\right] \quad (11)$$

In the relationship (10) the following notation will be introduced:

$$\widetilde{\mathbf{C}} = \mathbf{R}_1^T \cdot \mathbf{C} \cdot \mathbf{R}_1 \quad (12)$$

We will replace the relationship (12) into relationship (10) and the following result will be obtained:

$$\mathbf{Q}_r = -\widetilde{\mathbf{C}} \cdot \mathbf{v}_1 \tag{13}$$

The torque of the constraint forces relative to the point $O_1$, in projections on the axis of the body fixed reference frame $T_1(O_1x_1y_1z_1)$, taking into account the moment of rolling friction $\overline{M_f}$, may be written as follows:

$$\mathbf{Q}_c = \mathbf{R}_1^{\mathrm{T}} \cdot \mathbf{L}_{\lambda f} \cdot \boldsymbol{\lambda} \tag{14}$$

In the relation (14) the quantities involved have the followings expressions:

$$\mathbf{L}_{\lambda f} = \left[\begin{array}{c|c|c} 1 & 0 & R \\ \hline 0 & 1 & -s \cdot \mathrm{sgn}(\omega_{z_1}) \end{array}\right]^{\mathrm{T}} \tag{15}$$

$$\boldsymbol{\lambda} = \left[T \;\vdots\; N\right]^{\mathrm{T}} \tag{16}$$

The torque of gyroscopic forces relative to the $O_1$ point, in projections on the axis of the body fixed reference frame $T_1(O_1x_1y_1z_1)$ may be written as follows:

$$\mathbf{Q}_g = -\widetilde{\boldsymbol{\omega}}_1 \cdot \mathbf{M}_{O_1} \cdot \mathbf{v}_1 \tag{17}$$

In the relation (17), the quantities involved have the following expressions:

$$\widetilde{\boldsymbol{\omega}}_1 = \left[\begin{array}{c|c|c} 0 & -\omega_{z_1} & 0 \\ \hline \omega_{z_1} & 0 & 0 \\ \hline 0 & 0 & 0 \end{array}\right] \tag{18}$$

The expressions of the quantities $\mathbf{M}_{O_1}$ and $\mathbf{v}_1$ are given by the relation (4) and (6) respectively.

## 3. EQUATIONS OF KINEMATIC CONSTRAINT

Between kinematical parameters of the solid rigid body in discussion the following relationships may be written:

$$\dot{x}_{O_1} + R \cdot \dot{\varphi}_1 = dx_{O_1}/dt + R \cdot d\varphi_1/dt = 0 \tag{19}$$

$$\dot{y}_{O_1} = dy_{O_1}/dt = 0 \tag{20}$$

Relations (19) and (20) may be written together using matrix formulation as follows:

$$\mathbf{L}_{\lambda 0} \cdot \dot{\mathbf{x}}_1 = \underset{2\times 1}{\underset{\sim}{\mathbf{0}}} = \left[0 \;\vdots\; 0\right]^T \tag{21}$$

In the relation (21) the matrix $\dot{x}_1$ is given by the relation (5) and the matrix $L_{\lambda 0}$ is given by the following relation:

$$\mathbf{L}_{\lambda 0} = \left[\begin{array}{c|c|c} 1 & 0 & R \\ \hline 0 & 1 & 0 \end{array}\right]^T \tag{22}$$

Taking into account the relation (2), the relation (21) will be written as follows:

$$\mathbf{L}_{\lambda 0} \cdot \mathbf{R}_1 \cdot \mathbf{v}_1 = \underset{2\times 1}{\underset{\sim}{\mathbf{0}}} = \left[0 \;\vdots\; 0\right]^T \tag{23}$$

In the relation (23) the following notation will be introduced:

$$\mathbf{L}_{\lambda} = \mathbf{L}_{\lambda 0} \cdot \mathbf{R}_1 \tag{24}$$

Taking into account the notation introduced by the relation (24), the relation (23) becomes:

$$\mathbf{L}_{\lambda} \cdot \mathbf{v}_1 = \underset{2\times 1}{\underset{\sim}{\mathbf{0}}} = \left[0 \;\vdots\; 0\right]^T \tag{25}$$

If we derive the relation (25) with respect to time, we will obtain:

$$\mathbf{L}_{\lambda} \cdot \dot{\mathbf{v}}_1 + \dot{\mathbf{L}}_{\lambda} \cdot \mathbf{v}_1 = \underset{2\times 1}{\underset{\sim}{\mathbf{0}}} = \left[0 \;\vdots\; 0\right]^T \tag{26}$$

In the relation (26) the expression of the matrix $\dot{L}_{\lambda}$ is given by the following relation:

$$\dot{\mathbf{L}}_\lambda = \mathbf{L}_{\lambda 0} \cdot \dot{\mathbf{R}}_1 = \mathbf{L}_{\lambda 0} \cdot \mathbf{R}_1 \cdot \tilde{\boldsymbol{\omega}}_1 \qquad (27)$$

In the relation (27) the expression of the matrix $\tilde{\boldsymbol{\omega}}_1$ is given by the relationship (18). Using the relation (27) the relation (26) becomes:

$$\mathbf{L}_\lambda \cdot \dot{\mathbf{v}}_1 + \mathbf{L}_{\lambda 0} \cdot \mathbf{R}_1 \cdot \tilde{\boldsymbol{\omega}}_1 \cdot \mathbf{v}_1 = \underset{2\times 1}{\mathbf{0}} = [0 \,\vdots\, 0]^T \qquad (28)$$

By replacing the relationship (24) into the relationship (28), it becomes:

$$\mathbf{L}_\lambda \cdot \dot{\mathbf{v}}_1 + \mathbf{L}_\lambda \cdot \tilde{\boldsymbol{\omega}}_1 \cdot \mathbf{v}_1 = \underset{2\times 1}{\mathbf{0}} = [0 \,\vdots\, 0]^T \qquad (29)$$

The relation (29) may be written under the following equivalent form:

$$\mathbf{L}_\lambda \cdot \dot{\mathbf{v}}_1 = -\mathbf{L}_\lambda \cdot \tilde{\boldsymbol{\omega}}_1 \cdot \mathbf{v}_1 \qquad (30)$$

In the next chapter we will present a method of elimination of the constraint forces from the differential equations of motion.

## 4. ELIMINATION OF THE CONSTRAINT FORCES FROM THE DIFFERENTIAL EQUATIONS OF MOTION

Constraint forces are unknown and therefore they must be removed from the differential equations of motion. In this section is described a method of elimination of the constrained forces from the differential equations describing the motion of the motor wheel. The differential equations of motion (1) may be written in the following equivalent form:

$$\mathbf{M}_{O_1} \cdot \dot{\mathbf{v}}_1 = \mathbf{Q} + \mathbf{L}_{\lambda f} \cdot \boldsymbol{\lambda} \qquad (31)$$

In the relation (31) the quantities involved have the following expressions:

$$\mathbf{Q} = \mathbf{Q}_g + \mathbf{Q}_a + \mathbf{Q}_r \qquad (32)$$

$$\mathbf{L}_{\lambda f} = \mathbf{R}_1^T \cdot \mathbf{L}_{\lambda f 0} \qquad (33)$$

We will multiply the differential equation to the left by $\mathbf{M}_{O_1}^{-1}$ and we will obtain:

$$\dot{\mathbf{v}}_1 = \mathbf{M}_{O_1}^{-1} \cdot \mathbf{Q} + \mathbf{M}_{O_1}^{-1} \cdot \mathbf{L}_{\lambda f} \cdot \boldsymbol{\lambda} \qquad (34)$$

We will multiply the differential equation to the left by $L_\lambda$ and we will obtain:

$$\mathbf{L}_\lambda \cdot \dot{\mathbf{v}}_1 = \mathbf{L}_\lambda \cdot \mathbf{M}_{O_1}^{-1} \cdot \mathbf{Q} + \mathbf{L}_\lambda \cdot \mathbf{M}_{O_1}^{-1} \cdot \mathbf{L}_{\lambda f} \cdot \boldsymbol{\lambda} \qquad (35)$$

Taking into account the relation (29) the relation (35) becomes:

$$-\mathbf{L}_\lambda \cdot \tilde{\boldsymbol{\omega}}_1 \cdot \mathbf{v}_1 = \mathbf{L}_\lambda \cdot \mathbf{M}_{O_1}^{-1} \cdot \mathbf{Q} + \mathbf{L}_\lambda \cdot \mathbf{M}_{O_1}^{-1} \cdot \mathbf{L}_{\lambda f} \cdot \boldsymbol{\lambda} \qquad (36)$$

In the relation (36) the following notations will be introduced:

$$\mathbf{L}_\lambda \cdot \tilde{\boldsymbol{\omega}}_1 \cdot \mathbf{v}_1 = \mathbf{A} \qquad (37)$$

$$\mathbf{L}_\lambda \cdot \mathbf{M}_{O_1}^{-1} \cdot \mathbf{Q} = \mathbf{B} \qquad (38)$$

$$\mathbf{L}_\lambda \cdot \mathbf{M}_{O_1}^{-1} \cdot \mathbf{L}_{\lambda f} = \mathbf{D} \qquad (39)$$

Using the notations given by the relations (37-39), the relation (36) may be written as follows:

$$-\mathbf{A} = \mathbf{B} + \mathbf{D} \cdot \boldsymbol{\lambda} \qquad (40)$$

The constraint forces may be determined from relation (40) as follows:

$$\boldsymbol{\lambda} = -\mathbf{D}^{-1} \cdot (\mathbf{A} + \mathbf{B}) \qquad (41)$$

Finally we will obtain a system of six differential equations with six unknowns which may be written as follows:

$$\mathbf{M}_{O_1} \cdot \dot{\mathbf{v}}_1 = \mathbf{Q} + \mathbf{L}_{\lambda f} \cdot \boldsymbol{\lambda} \qquad (42)$$

$$\dot{\mathbf{x}}_1 = \mathbf{R}_1 \cdot \mathbf{v}_1 \tag{43}$$

The differential equations system given by the relations (42) and (43) will be solved using numerical integration methods.

## 5. NUMERICAL APLICATION

Using MATHLAB software a computing program solving the differential equations system was designed. In order to run the computing program the following input data are necessary:

$$m_1 = 1[kg] \tag{44}$$

$$J_{z_1} = 1[kg \cdot m^2] \tag{45}$$

$$R = 1[meter] \tag{46}$$

$$c_t = 1[kg/\sec.] \tag{47}$$

$$c_r = 1[kg \cdot m/\sec.] \tag{48}$$

$$g = 10[m/\sec^2] \tag{49}$$

$$F = 15[N] \tag{50}$$

$$\alpha = \pi/6\ [radians] \tag{51}$$

$$s = 0.5\ [meters] \tag{52}$$

The following initial conditions are also necessary:

$$v^0_{O_1x_1} = 0[meters/\sec.] \tag{53}$$

$$v^0_{O_1y_1} = 0[meters/\sec.] \tag{54}$$

$$\omega^0_{z_1} = 0[radians/\sec.] \tag{55}$$

The initial values of coordinates $x_{O_1}$ and $y_{O_1}$ of the origin $O_1$ relative to the fixed reference frame $T(Oxyz)$ are the followings:

$$x^0_{O_1} = 0[meters] \tag{56}$$

$$y^0_{O_1} = 0[meters] \tag{57}$$

$$\varphi^0_1 = 0[radians] \tag{58}$$

The dynamic study was performed during a period of ten seconds. The results are presented in the figures below (Fig.2-Fig.5). The dynamics of the wheel was performed taking into account two distinct cases. In the first case the rolling friction was taken under consideration by its effect, namely, the rolling friction moment $\overline{M_f}$ .In the second case the rolling friction moment was ignored. Both results are presented in the above mentioned figures (Fig.2-Fig.5).

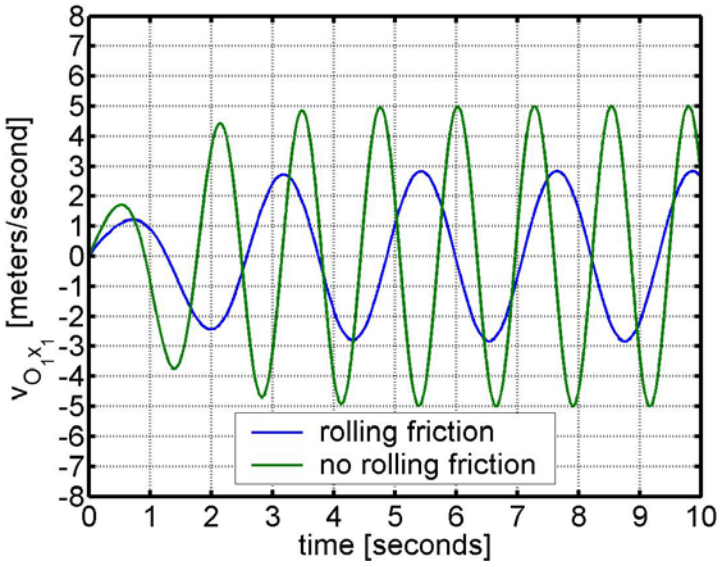


**Figure 2. Variation of the $v_{O_1x_1}$ velocity with respect to time**

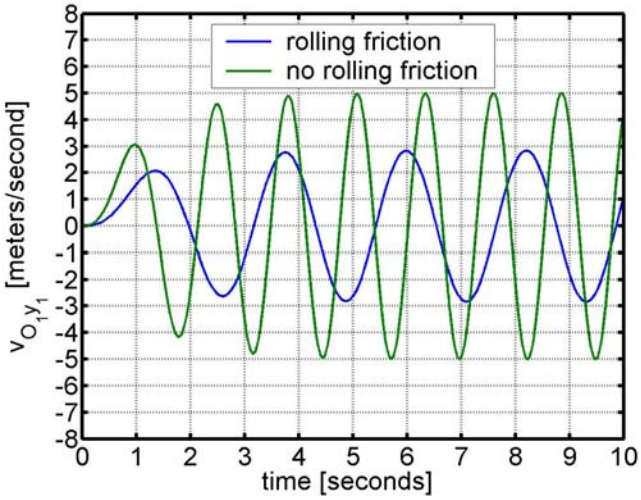


**Figure 3. Variation of the $v_{O_1y_1}$ velocity with respect to time**

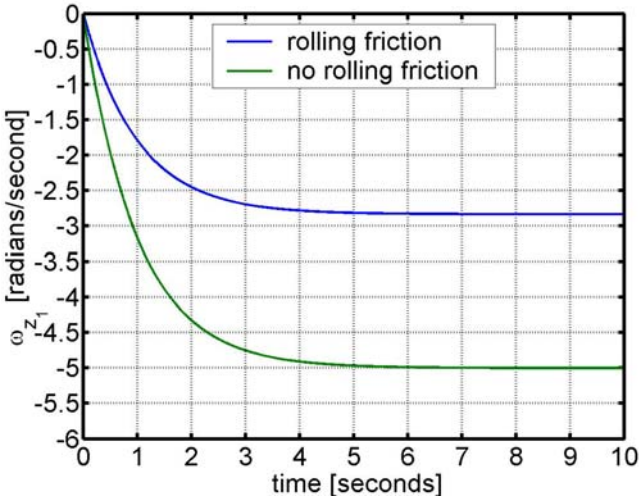


**Figure 4. Variation of the $\omega_{z_1}$ angular velocity with respect to time**

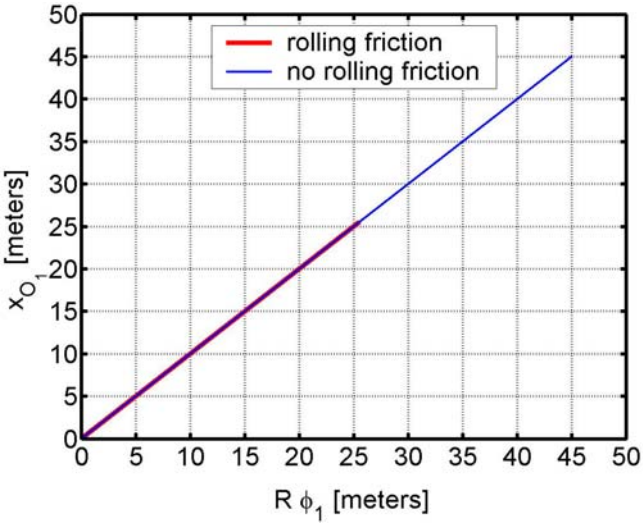


**Figure 5. Variation of the $x_{O_1}$ abscissa with respect of the product $R \cdot \varphi_1$**

## 6. CONCLUSIONS

The paper presents the dynamic study of a wheel acted by a horizontal force parallel with a titled plane. The differential equations describing the movement of the wheel were written in matrix form in projections on the axes of the mobile reference system, namely the reference system moving together with the rigid solid body. This reference frame is considered to be to the rigid solid body. The problem of the dynamics of the drawn wheel was approached in an original manner. The drawn wheel was regarded as a rigid solid body subject to constraints. Therefore, the motion equations was written as an algebraic sum between three torques, namely the torque of the inertial forces, the torque of the active forces and the torque of the link forces.

The mathematical expression of every torque was put into evidence explicitly.

The paper also presents an original method of removing the link forces from the differential equations of motion. Using this method, the determination of the orthogonal complement [6, 7] or the natural orthogonal complement [4] is no longer necessary.

The paper also presents a method of deducting the mathematical relationships between kinematical parameters of the rigid solid body whose dynamics is studied in the paper.

The dynamic study presented in the paper can be continued with the determining of the variation with respect to time of the link forces.

## REFFERENCES


[1] Vâlcovici V., Bălan Şt., Voinea R., Mecanica Teoretică, Bucureşti, Editura Tehnică, 1968

[2] Voinea R., Voiculescu D., Ceauşu V., Mecanica, Bucureşti, Editura Didactică şi Pedagogică, 1983, pp.351-355

[3] Ştefan Staicu, Aplicaţii ale calculului matriceal în mecanica solidelor:Bucureşti, Editura Academiei R.S.R, 1983

[4] Kamman J.V., Houston R.L., Dynamics of Constraint Multibody Systems, 1984, ASME, Journal of Applied Mechanics, volume 51, pp. 899-903

[5] Jorge Angeles, Sang Koo Lee, The Formulation of Dynamical Equations of Holonomic Mechanical Systems Using a Natural Orthogonal Complement, Journal of Applied Mechanics, March 1988, volume 55 pp. 243-244.

[6] Houston R.L., Methods of Analysis of Constrained Multibody Systems, 1989, Mechanics of Structures and Machines, volume 17, No.2, pp. 135-143

[7] Nikraves P.E., Systematic Reduction of Multibody Equations of Motion to a Minimal Set, 1990, International Journal of Non-Linear Mechanics, volume 25, pp. 143-151

[8] Papastravidis J.P., Maggi's Equations of Motion and the determination of Constrained Reactions, 1990, AIAA Journal of Guidance, Control and Dynamics

[9] J.G. Papastavridis, On the Transitivity Equations of Rigid-Body Dynamics, Journal of Applied Mechanics, 1992, volume 59 pp. 955-962

[10] W. Blajer, A Projection Method Approach to Constrained Dynamic Analysis, September 1992, Journal of Applied Mechanics, volume 59 pp. 643-649

[11] W. Blajer, D. Bestle, W. Schiehlen, An Orthogonal Matrix Formulation for Constrained Multibody Systems, June 1994, Journal of Mechanical Design, volume 116 pp. 423-428

[12] S.D. Muşat, Ecuaţii de tip Euler pentru solidul rigid deduse din ecuatiile lui Lagrange, 1995, A XIX-a Conferinţă de Mecanica Solidelor, volume 2 pp. 219-226

[13] Ştefan Staicu, Mecanica Teoretică:Bucureşti, Editura Didactică şi Pedagogică R.A., 1998

[14] Florin Bauşic, Mecanica Teoretică. Dinamica. Mecanica Analitică., Bucureşti, Editura Conspress, 2004

[15] Wojchiech Blajer, On the Determination of Joint Reactions in Multibody Mechanisms, 2004, Journal of Mechanical Design, volume 126, pp. 341-350

[16] Polidor Bratu, Mecanica Teoretică., Bucureşti, Editura Impulse, 2006

[17] Staicu Şt., On the Determination of Joint Reactions in Multibody Mechanisms, September, 2009, Multibody Systems Dynamics, Springer, volume 22, No.2, pp. 115-132

The Scientific Bulletin of VALAHIA University
MATERIALS and MECHANICS –Vol. 17, No. 16

DOI 10.2478/bsmm-2019-0006

# DESIGN OF MICROFLUIDIC DEVICE AND MEASUREMENTS OF MPWM FOR SINGLE CELL /PARTICLE MANIPULATION

**Mihăiţă Nicolae ARDELEANU[1,2], Simona MIHAI[3], Ruxandra VIDU[4]**

**Emil Mihai DIACONU[5] and Ileana Nicoleta POPESCU[1,*]**

[1]Faculty of Materials Engineering and Mechanics, Valahia University of Targoviste, 13 Aleea Sinaia Street, Targoviste, Romania

[2]S.C. Celteh Mezotronic S.R.L. , Calea Câmpulung Street, No. 6A, Targoviste, Romania

[3]The Scientific and Technological Multidisciplinary Research Institute (ICSTM-UVT), Valahia University of Targoviste, Romania

[4] California Solar Energy Collaborative, University of California, Davis, 1, Shields Ave, Davis, USA

[5]Faculty of Electrical Engineering, Electronics and Information Technology, Valahia University of Targoviste, 13 Aleea Sinaia Street , Targoviste, Romania

E-mail: * pinicoleta24@yahoo.com

**Abstract:** *A microfluidic device designated for measurement of fluidic flows with different viscosity, necessary within trapping/realising of cells/particles system has been developed. We use a new concept as Microfluidic Pulse Width Modulation (MPWM) for controlling transport of a single cell/particle. The image processing helped the nano-hydraulic volumes/flow rates measurement, through tracking inovative methods with the purpose to build a flow sensor. The device open an unique opportunitie for single cell study with applications in biomedical devices, tools for biochemistry or analytical systems.*

**Keywords:** *Single-cell/particle manipulation, Microfluidic device, MPWM, Sensor, Video-measurement of volumes rate*

## 1. INTRODUCTION

Microfluidics is increasingly being used in many areas of biotechnology and chemistry [1-5] to achieve reduced consumption of reagents /analytes, improved performance, low costs of fabrications and decrease time of analyses, and also, among other advantages, to obtain miniaturization and integration of fluidic components, developed as well known concept of „lab on a chip" [3, 4, 5].

The device design and selection of materials are important steps for fabrication of microfluidic device for biomedical, chemistry or biochemisry applications [1-3, 5-11].

The elastomeric materials PDMS is the most widely used material in microfluidic device fabrication due to its many advantages in fabrication:

(i) facile and cost-effective production of it at microscale by rapid prototyping [12] and replica molding [5-8 in comparison with etching in glass and silicon [4, 7].

(ii) is inexpensive,

(iii) has high fidelity at micrometric scale and

(iv) is optical transparent.

For controlling transport of fluids or particles/cells through microfluidic channels some researches [13, 14] used "A microfluidic diluter based on pulse width flow modulation [13] or Pulse Width Modulation of Liquid Flows, introducing the concept "Pulse-Width-Modulation" (PWM) with a dynamic duty cycle over time for liquid flows [14].

## 2. MATERIALS AND DEVICE DESIGN

### 2.1 Materials

We used PDMS as material for microfluidic device, commercial name for this product is Sylgard184, produced by DOW CORNING Company (USA).

The device consisted of three layers: One of them is the PDMS layer that was fabricated using two ways: (i) laser ablation; (ii) rapid prototyping, and the other two layers were two transparency plexiglass supports.

### 2.2. Device design

For the device design we took in consideration the following factors:
(i). Field Of View (FOV) -4x, respectively 10x (see Fig. 1);

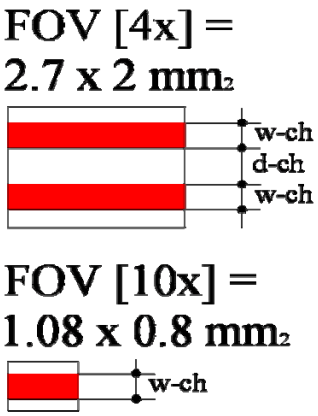


**Figure 1. Device design - Schematic representations of microfluidic channels with Field of View (FOV)**

(ii) Nomber of measurement points - ~ 40 points;
(iii) Minimum estimated volume of MPWM – 10 nl.

The basic concept for obtaining two channels in the same FOV was the needing to prove the positioning accuracy of MPWM for a certain route, in that case one microfluidic loop (see Fig. 2).

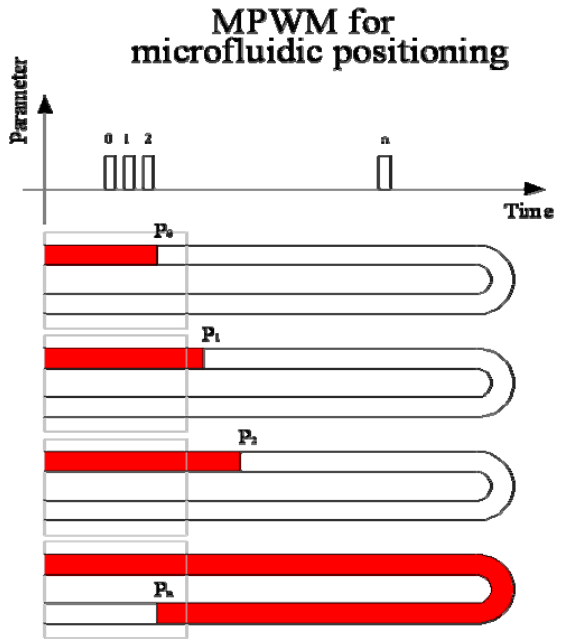


**Figure 2. MPWM for microfluidic positioning**

The resulted cross sectional area of microfluidic channels was 0.25 mm$^2$, with dimensional size 0.5 mm x 0.5 mm and the total channel length is 250 mm. The CAD model is shown in Fig.3a and the replica molding is presented in Fig.3b.

## 3. THE BASIC CONCEPT OF SINGLE CELL MANIPULATION USING THE MICROFLUIDIC DEVICE

The picked cell (by aspiration) is led using the microfluidic route to the separation zone for observation and extraction.

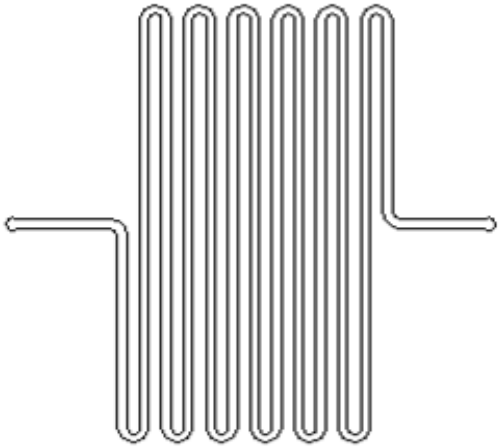

**Figure 3a. The CAD model of the microfluidic device**

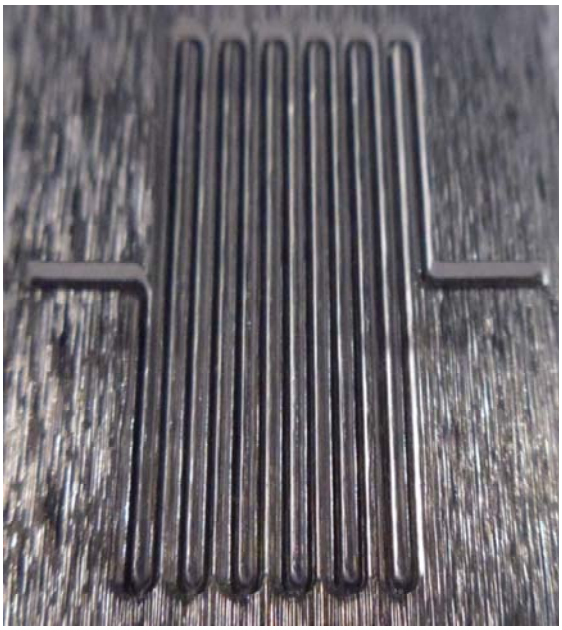

**Figure 3b. The replica molding of the microfluidic device**

In Fig. 4 can be observed the whole microfluidic manipulation system: (a) The extractor generates microfluidc power; (b) The route allows the transportation of cell to the separation zone; (c) The picking function is obtained using a specific tube terminal adapted for cell's size.

To avoid the introduction of hydraulic resistance in route, we use the technical solution presented in Fig. 5.

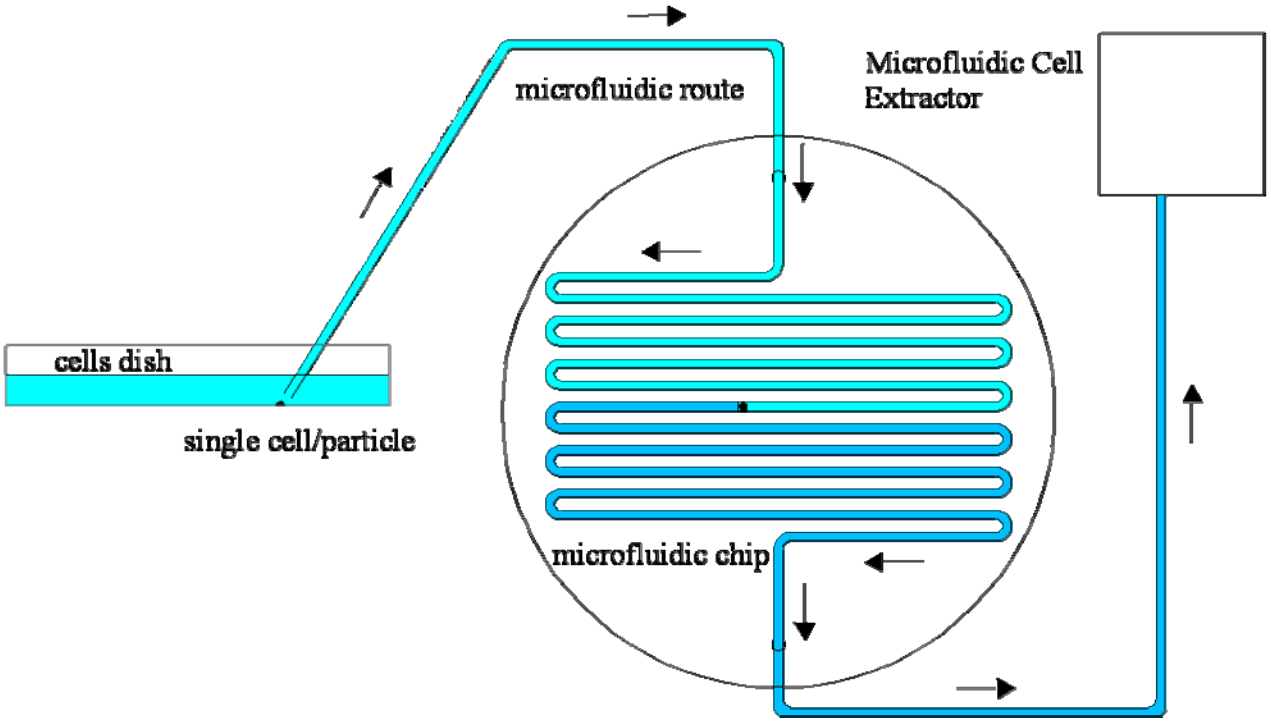


**Figure 4. Schematic representation of the whole microfluidic manipulation system**

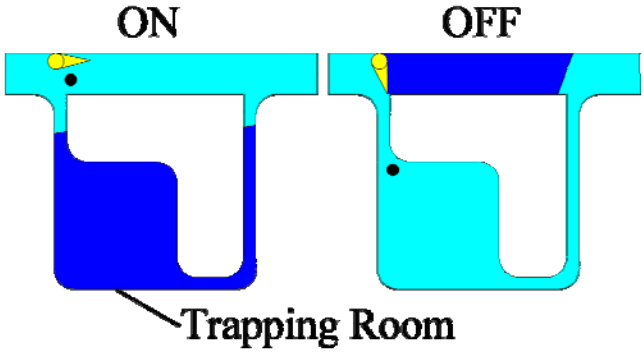


**Figure 5. Details of the trapping room of microfluidic manipulation system (schematic representation)**

It consists of a special selection valve between two ways of advancing with different sections: the large one allows unobstructed advancing of fluid, and the small one is adapted to the cell size and permits the trapping of it.

## 4. VOLUMES/FLOW RATES MEASUREMENTS USING IMAGE PROCESSING

A microscope (AmScope type, United Scope USA) (see fig. 6) equipped with a high speed camera (Raspberry PI) was used to record the experimental events:
(i) volume rate measurement;
(ii) flow rate measurements.

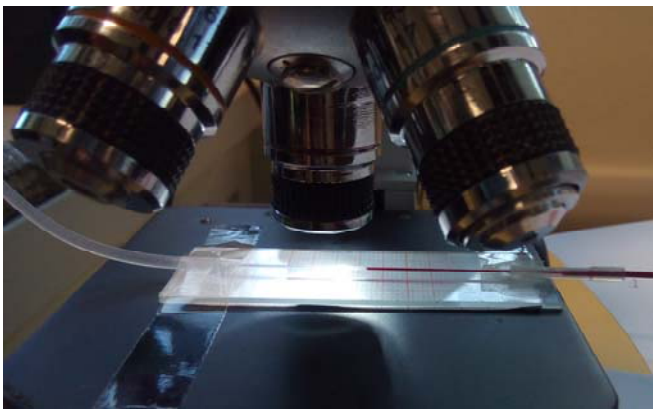

**Figure 6. The microscope (AmScope type) equipped with a high speed camera (Raspberry PI) used for measurements**

In Fig.7 it's presented the MWPM principle. We deduced the formula of flow rate: ***Q=V_total/T_total*** [1]. For volume rate, an essential parameter is the measured displacements of liquid front (see Fig.8).

We used equal values for $t_{on}$.***MPWM***, in consequence we obtained the same volumes rates, respectively vol in Fig.7. The V_total is a multiplier of ***vol***.

The key of MPWM is the correspondence between $t_{on}$ and vol. The channel used for measurements was a glass capillary with interior diameter of 0.42 mm.

The calculus formula for **vol**, in this particularly case, is: ***Y=X x 0.13854. X*** is the displacement of front [µm], 0.13854 represents the cross sectional area of capillary and Y is resulted ***vol***.

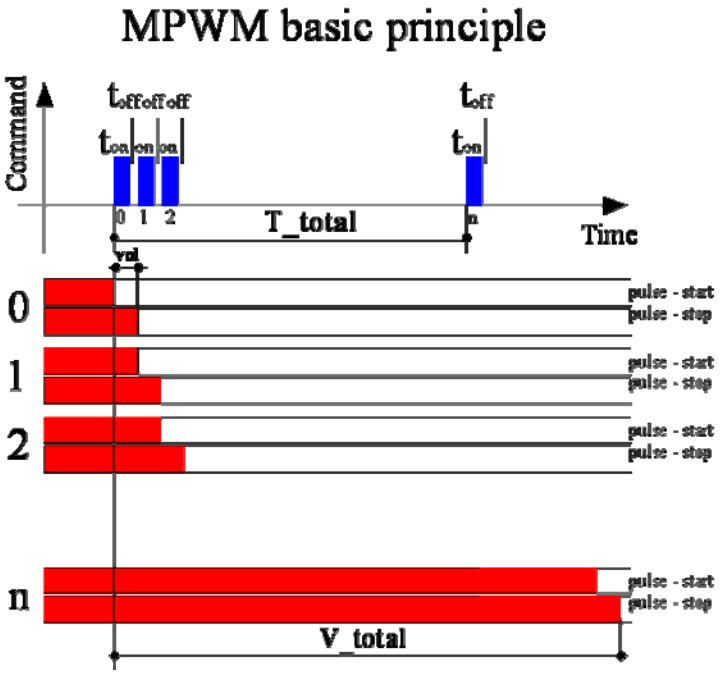


**Figure 7. The MPWM basic principle**

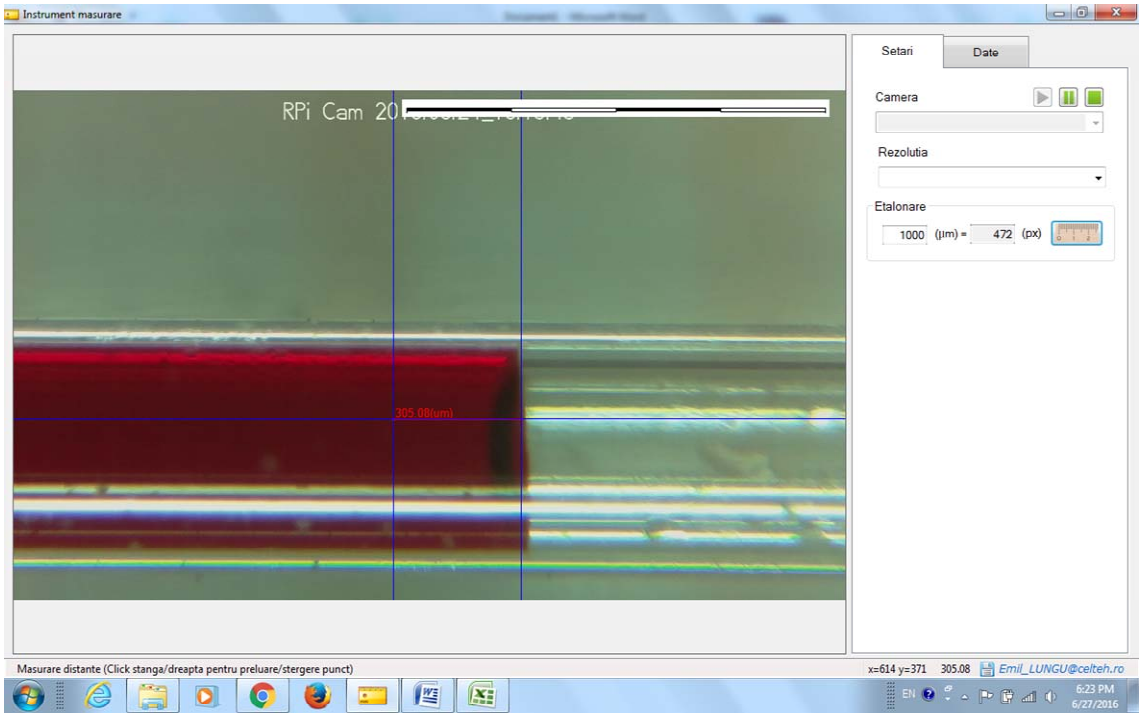


**Figure 8. The measured displacements of liquid front (image capture of microscope camera)**

## 5. RESULTS

The Microfluidic Pulse Width Modulation MPWM parameters for experimental test are presented in Table1.

**Table 1. The MPWM parameters for experimental test**

| No. | X | Y | S | T_on | T_off | T | FU | Freq |
|---|---|---|---|---|---|---|---|---|
| | um | nl | steps | us | us | us | % | Hz |
| 1 | 76 | 10.5 | 1 | 1015 | 3050 | 4065 | 25.0 | 246.0 |
| 2 | 77 | 10.7 | 1 | 1015 | 3050 | 4065 | 25.0 | 246.0 |
| 3 | 75 | 10.4 | 1 | 1015 | 3050 | 4065 | 25.0 | 246.0 |
| 4 | 77 | 10.7 | 1 | 1015 | 3050 | 4065 | 25.0 | 246.0 |
| 5 | 78 | 10.8 | 1 | 1015 | 3050 | 4065 | 25.0 | 246.0 |
| 6 | 76 | 10.5 | 1 | 1015 | 3050 | 4065 | 25.0 | 246.0 |
| 7 | 77 | 10.7 | 1 | 1015 | 3050 | 4065 | 25.0 | 246.0 |
| 8 | 77 | 10.7 | 1 | 1015 | 3050 | 4065 | 25.0 | 246.0 |
| 9 | 78 | 10.8 | 1 | 1015 | 3050 | 4065 | 25.0 | 246.0 |
| 10 | 76 | 10.5 | 1 | 1015 | 3050 | 4065 | 25.0 | 246.0 |
| 11 | 76 | 10.5 | 1 | 1015 | 3050 | 4065 | 25.0 | 246.0 |
| 12 | 77 | 10.7 | 1 | 1015 | 3050 | 4065 | 25.0 | 246.0 |
| 13 | 75 | 10.4 | 1 | 1015 | 3050 | 4065 | 25.0 | 246.0 |
| 14 | 76 | 10.5 | 1 | 1015 | 3050 | 4065 | 25.0 | 246.0 |
| 15 | 77 | 10.7 | 1 | 1015 | 3050 | 4065 | 25.0 | 246.0 |
| 16 | 78 | 10.8 | 1 | 1015 | 3050 | 4065 | 25.0 | 246.0 |
| 17 | 78 | 10.8 | 1 | 1015 | 3050 | 4065 | 25.0 | 246.0 |
| 18 | 76 | 10.5 | 1 | 1015 | 3050 | 4065 | 25.0 | 246.0 |
| 19 | 77 | 10.7 | 1 | 1015 | 3050 | 4065 | 25.0 | 246.0 |
| 20 | 78 | 10.8 | 1 | 1015 | 3050 | 4065 | 25.0 | 246.0 |

We used a normal frequency (246 Hz) and a fill factor of 25%. In the same table (Table 1) is presented a series of measurements for volume rates.

The average value for 20 points of measurements is 10.63 nl. We generated in automative mode this MPWM signal and resulted flow rate was 10.63/4.065 = 2615 [nl/s].

## 6. CONCLUSIONS

We verified experimentally the MPWM concept. In this way we open the research study of microfluidic transport of soft objects (eg cells). In this paper, we measured using image processing the nano-hydraulic volumes/flow rates. By automating calculation of "volume / time" ratio, it will result a transducer flow [15].

The central element of this transducer will be the designed microfluidic chip. Through image processing can be obtained automatically both rates and debit volume, at passing of the liquid within chip's channels.

## REFERENCES:


[1] Zhou, Y., Basu, S., Wohlfahrt, K. J., Lee, S. F., Klenerman, D., Laue, E. D., & Seshia, A. A. , A microfluidic platform for trapping, releasing and super-resolution imaging of single cells. Sensors and Actuators B: Chemical, 232 (2016) 680-691.

[2] Ravetto, A., Hoefer, I. E., den Toonder, J. M., & Bouten, C. V., A membrane-based microfluidic device for mechano-chemical cell manipulation. Biomedical microdevices, 18(2) (2016) 31.

[3] Van Dam, R. Michael , Solvent-resistant elastomeric microfluidic devices and applications. Dissertation (Ph.D.), 2006.

[4] McDonald, J. C., Duffy, D. C., Anderson, et. al.. Fabrication of microfluidic systems in poly (dimethylsiloxane). Electrophoresis, 21(1) (2000) 27-40.

[5] Lee, Cheng-Chung, Chemical synthesis in elastomer-based integrated microfluidics. Dissertation (Ph.D.), 2010.

[6] Carugo D., Lee J.Y., Pora A., Browning R.J., Capretto L, Nastruzzi C, Stride E, Facile and cost-effective production of microscale PDMS architectures using a combined micromilling-replica moulding (μMi-REM) technique, Biomed Microdevices. 18(1) (2016) 4.

[7] James Friend, Leslie Yeo, Fabrication of Microfluidic Systems In Poly(Dimethylsiloxane), Biomicrofluidics. Jun; 4(2)( 2010) https://doi.org/10.1063/1.3259624.

[8] Kai Zhang, Li-Bo Zhao, Shi-Shang , et.al. , A microfluidic system with surface modified piezoelectric sensor for trapping and detection of cancer cell, Biosensors and Bioelectronics, 26 (2)(2010) 935–993.

[9] Ivan, I., Ardeleanu, M., & Laurent, G., High dynamics and precision optical measurement using a position sensitive detector (PSD) in reflection-mode: application to 2D object tracking over a smart surface. Sensors, 12(12) (2012) 16771-16784.

[10] Ardeleau, M., Mihai, S., Gurgu, V., & Olteanu, L. Microscopic Enclosures Modelling Designated For Biomedical Applications of Cellular Manipulation Type In Liquid Environment., Scientific Bulletin of Valahia University-Materials and Mechanics, 10(13)(2015) 199-201

[11] Ivan, I. A., Ardeleanu, M., Laurent, G. J., Tan, N., & Clevy, C.. The metrology and applications of PSD (position sensitive detector) sensors for microrobotics International Symposium on Optomechatronic Technologies (ISOT 2012) IEEE (2012) 1-2.

[12] Ardeleanu, M., Ivan, I. A., & Despa, V.. Rapid prototyping technologies used for a microgripper frameworks fabrication. The Romanian Review Precision Mechanics, Optics & Mechatronics, 44 (2013) 89-91.

[13] Ainla, A., Gözen, I., Orwar, O., & Jesorka, A. A microfluidic diluter based on pulse width flow modulation. Analytical chemistry, 81(13)(2009) 5549.

[14] Unger, M., Lee, S. S., Peter, M., & Koeppl, H. Pulse width modulation of liquid flows: Towards dynamic control of cell microenvironments. In The 15th International Conference on Miniaturized Systems for Chemistry and Life Sciences ((2011)1567-1569.

[15] Ardeleanu, M., Ionita, M., Ivan, A., & Gurgu, V., Innovative Bidimensional Absolute Transducer Based on Video Detection for Positioning into Micro Assembly Processes. In Applied Mechanics and Materials, Trans Tech Publications, 658 (2014). 535-540.

The Scientific Bulletin of VALAHIA University
MATERIALS and MECHANICS –Vol. 17, No. 16

DOI 10.2478/bsmm-2019-0007

# KINEMATICAL ANALYSIS OF THE ARTICULATED QUADRILATERAL MECHANISM USING THE PRINCIPLE OF VIRTULAL MECHANICAL WORK

**Vladimir Dragoş TĂTARU [1*], Mircea Bogdan TĂTARU [2**]**

[1]Valahia University of Targoviste, Faculty of Materials Engineering and Mechanics, 13 Aleea Sinaia Street, Targoviste, Romania, [2]University of Oradea

E-mail: * vdtataru@gmail.com, ** btataru@uoradea.ro

**Abstract:** *The paper presents a numerical method of kinematical analysis of the articulated quadrilateral mechanism, using the principle of virtual mechanical work for establishing the relations of connection between the kinematical parameters describing the movement of its elements.*

**Keywords:** *kinematical analysis, virtual mechanical work, mechanism, element, cylindrical joint, constraint force*

## NOMENCLATURE

$T$ -denotes the transposition matrix operation

$X_{10}, Y_{10}$ -connecting forces in $O_1$ cylindrical joint

$X_{20}, Y_{20}$ -connecting forces in $O_2$ cylindrical joint

$X_{30}, Y_{30}$ -connecting forces in $O_3$ cylindrical joint

$X_{40}, Y_{40}$ -connecting forces in $O_4$ cylindrical joint

$T(Oxyz)$-fixed reference system

$x_{O_1}, y_{O_1}$ -coordinates $O_1$ cylindrical joint

$v_{O_1x}, v_{O_1y}$ -velocities projections $O_1$ cylindrical joint

$a_{O_1x}, a_{O_1y}$ -acceleration projections of $O_1$ point

$x_{O_2}, y_{O_2}$ -coordinates $O_2$ cylindrical joint

$v_{O_2x}, v_{O_2y}$ -velocities projections $O_2$ cylindrical joint

$a_{O_2x}, a_{O_2y}$ -accelerations projections of point $O_2$

$x_{O_3}, y_{O_3}$ -coordinates of point $O_3$

$v_{O_3x}, v_{O_3y}$ -velocities projections of $O_3$ cylindrical joint

$a_{O_3x}, a_{O_3y}$ -acceleration projections of point $O_3$

$x_{O_4}, y_{O_4}$ -coordinates of $O_4$ cylindrical joint

$\varphi_1$ -self rotation angle of element 1

$\omega_{1z}$ -angular velocity projection on $Oz$ axe of element 1

$\varepsilon_{1z}$ -angular acceleration of element 1

$\varphi_2$ -self rotation angle of element 2

$\omega_{2z}$ -angular velocity projection on $Oz$ axe of element 2

$\varepsilon_{2z}$ -angular acceleration of element 2

$\varphi_3$ -self rotation angle of element 3

$\omega_{3z}$ -angular velocity projection on $Oz$ axe of element 3

$\varepsilon_{3z}$ -angular acceleration of element 1

$l_1$ -length of element 1 of the mechanism

$l_2$ -length of element 2 of the mechanism

$l_3$ -length of element 3 of the mechanism

## 1. INTRODUCTION

We will consider the articulated quadrilateral mechanism as it is shown in the figure below (Fig.1). Since the very beginning we will consider that all the points of its elements are in one plane throughout the movement. The kinematics of the articulated quadrilateral mechanism was studied using transfer functions [2]. We propose ourselves to perform the complete kinematical analysis of this mechanism using the principle of virtual work.

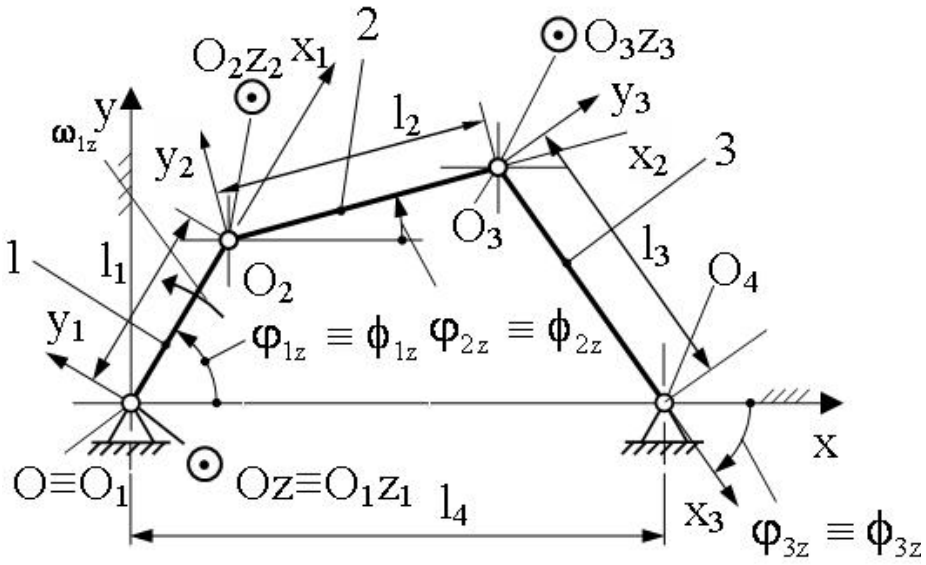


**Figure 1. Articulated quadrilateral mechanism**

The kinematical positional analysis of the articulated quadrilateral mechanism was performed using an analytical method [2]. The paper [8] presents an incremental numerical method used for the positional kinematical analysis of the same mechanism.

## 2. WRITING THE RELATIONSHIPS BETWEEN THE FIRST ORDER KINEMATICAL PARAMETERS USING THE PRINCIPLE OF VIRTUAL MECHANICAL WORK

In order to write the relationships between kinematical parameters of the first order using the principle of the virtual mechanical work, we will have to replace the inner and outer connections of the mechanism will be replaced by their mechanical effect. Since the mechanical effect of a constraint is given by the constraint force, the joints will be considered removed and replaced with the corresponding constraint forces (Fig.2). The joint $O_1$ is replaced by the corresponding forces $\overline{X_{10}}$ and $\overline{Y_{10}}$. The joint $O_2$ is removed and replaced by the corresponding forces $\overline{X_{20}}$ and $\overline{Y_{20}}$. The joint $O_3$ is removed and replaced by the forces $\overline{X_{30}}$ and $\overline{Y_{30}}$. Finally the joint $O_4$ is removed and replace by the forces $\overline{X_{40}}$ and $\overline{Y_{40}}$.

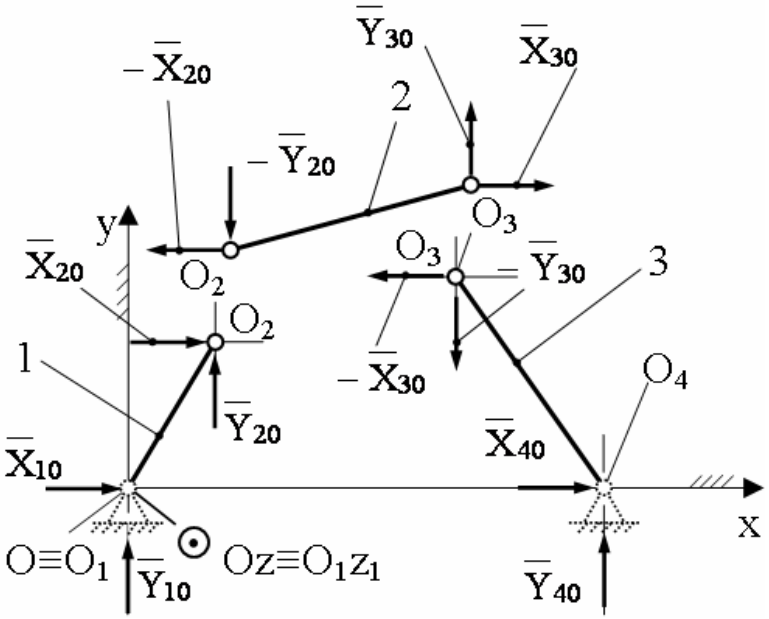


**Figure 2. Articulated quadrilateral mechanism with the links removed and replaced by the corresponding constraint forces**

The mathematical expression of the principle of virtual mechanical work will be written in matrix form as follows:

$$\boldsymbol{\tau}^{cT} \cdot \mathbf{v} = 0 \qquad (1)$$

$$\boldsymbol{\tau}^{c} = \left[ \boldsymbol{\tau}_{O_1}^{c\ T} \mid \boldsymbol{\tau}_{O_2}^{c\ T} \mid \boldsymbol{\tau}_{O_3}^{c\ T} \right]^T \quad (2)$$

$$\mathbf{v} = \left[ \mathbf{v}_1^T \mid \mathbf{v}_2^T \mid \mathbf{v}_3^T \right]^T \quad (3)$$

$$\mathbf{v}_1 = \left[ v_{O_1 x} \mid v_{O_1 y} \mid \omega_{1z} \right]^T \quad (4)$$

$$\mathbf{v}_2 = \left[ v_{O_2 x} \mid v_{O_2 y} \mid \omega_{2z} \right]^T \quad (5)$$

$$\mathbf{v}_3 = \left[ v_{O_3 x} \mid v_{O_3 y} \mid \omega_{3z} \right]^T \quad (6)$$

$$\boldsymbol{\tau}^{cT} \cdot \mathbf{v} = \boldsymbol{\tau}_{O_1}^{c\ T} \cdot \mathbf{v}_1 + \boldsymbol{\tau}_{O_2}^{c\ T} \cdot \mathbf{v}_2 + \boldsymbol{\tau}_{O_3}^{c\ T} \cdot \mathbf{v}_3 \quad (7)$$

$$\boldsymbol{\tau}_{O_1}^{c} = \left[ X_{10} \mid Y_{10} \mid 0 \right]^T + \left[ X_{20} \mid Y_{20} \mid -p_{1y} \cdot X_{20} + p_{1x} \cdot Y_{20} \right]^T \quad (8)$$

The relationship (8) can be written in a concise form as follows:

$$\boldsymbol{\tau}_{O_1}^{c} = \mathbf{A}_{11} \cdot \mathbf{F}_{10} + \mathbf{A}_{12} \cdot \mathbf{F}_{20} \quad (9)$$

$$\mathbf{A}_{11} = \left[ \begin{array}{c|c|c} 1 & 0 & 0 \\ 0 & 1 & 0 \end{array} \right]^T \quad (10)$$

$$\mathbf{F}_{10} = \left[ X_{10} \mid Y_{10} \right]^T \quad (11)$$

$$\mathbf{A}_{12} = \left[ \begin{array}{c|c|c} 1 & 0 & -p_{1y} \\ 0 & 1 & p_{1x} \end{array} \right]^T \quad (12)$$

$$\mathbf{F}_{20} = \left[ X_{20} \mid Y_{20} \right]^T \quad (13)$$

$$p_{1x} = x_{O_2} - x_{O_1} \quad (14)$$

$$p_{1y} = y_{O_2} - y_{O_1} \quad (15)$$

$$\boldsymbol{\tau}_{O_2}^{c} = \left[ -X_{20} \mid -Y_{20} \mid 0 \right]^T + \left[ X_{30} \mid Y_{30} \mid -p_{2y} \cdot X_{30} + p_{2x} \cdot Y_{30} \right]^T \quad (16)$$

$$\boldsymbol{\tau}_{O_2}^{c} = \mathbf{A}_{22} \cdot \mathbf{F}_{20} + \mathbf{A}_{23} \cdot \mathbf{F}_{30} \quad (17)$$

$$\mathbf{A}_{22} = \left[ \begin{array}{c|c|c} -1 & 0 & 0 \\ 0 & -1 & 0 \end{array} \right]^T \quad (18)$$

$$\mathbf{F}_{20} = \left[ X_{20} \mid Y_{20} \right]^T \quad (19)$$

$$\mathbf{A}_{23} = \left[ \begin{array}{c|c|c} 1 & 0 & -p_{2y} \\ 0 & 1 & p_{2x} \end{array} \right]^T \quad (20)$$

$$\mathbf{F}_{30} = \left[ X_{30} \mid Y_{30} \right]^T \quad (21)$$

$$p_{2x} = x_{O_3} - x_{O_2} \quad (22)$$

$$p_{2y} = y_{O_3} - y_{O_2} \quad (23)$$

$$\boldsymbol{\tau}_{O_3}^{c} = \mathbf{A}_{33} \cdot \mathbf{F}_{30} + \mathbf{A}_{34} \cdot \mathbf{F}_{40} \quad (24)$$

$$\boldsymbol{\tau}_{O_3}^{c} = \left[ -X_{30} \mid -Y_{30} \mid 0 \right]^T + \left[ X_{40} \mid Y_{40} \mid -p_{3y} \cdot X_{40} + p_{3x} \cdot Y_{40} \right]^T \quad (25)$$

$$\mathbf{A}_{33} = \left[ \begin{array}{c|c|c} -1 & 0 & 0 \\ 0 & -1 & 0 \end{array} \right]^T \quad (26)$$

$$\mathbf{F}_{30} = \left[ X_{30} \mid Y_{30} \right]^T \quad (27)$$

$$\mathbf{A}_{34} = \left[ \begin{array}{c|c|c} 1 & 0 & -p_{3y} \\ 0 & 1 & p_{3x} \end{array} \right]^T \quad (28)$$

$$\mathbf{F}_{40} = \left[ X_{40} \mid Y_{40} \right]^T \quad (29)$$

$$p_{3x} = x_{O_4} - x_{O_3} \quad (30)$$

$$p_{3y} = y_{O_4} - y_{O_3} \quad (31)$$

$$x_{O_4} = L_4 = const. \quad (32)$$

$$y_{O_4} = 0 \quad (33)$$

Using the expressions (9), (17) and (24), the matrix expression of the principle of virtual work (1) becomes:

$$\begin{aligned} &\boldsymbol{\tau}^{cT} \cdot \mathbf{v} = \\ &= \mathbf{F}_{10}^T \cdot \mathbf{A}_{11}^T \cdot \mathbf{v}_1 + \mathbf{F}_{20}^T \cdot \mathbf{A}_{12}^T \cdot \mathbf{v}_1 + \\ &+ \mathbf{F}_{20}^T \cdot \mathbf{A}_{22}^T \cdot \mathbf{v}_2 + \mathbf{F}_{30}^T \cdot \mathbf{A}_{23}^T \cdot \mathbf{v}_2 + \\ &+ \mathbf{F}_{30}^T \cdot \mathbf{A}_{33}^T \cdot \mathbf{v}_3 + \mathbf{F}_{40}^T \cdot \mathbf{A}_{34}^T \cdot \mathbf{v}_3 = 0 \end{aligned} \quad (34)$$

By performing the calculations we will obtain:

$$\begin{aligned} &\boldsymbol{\tau}^{cT} \cdot \mathbf{v} = \\ &= \mathbf{F}_{10}^T \cdot \mathbf{A}_{11}^T \cdot \mathbf{v}_1 + \\ &+ \mathbf{F}_{20}^T \cdot \left( \mathbf{A}_{12}^T \cdot \mathbf{v}_1 + \mathbf{A}_{22}^T \cdot \mathbf{v}_2 \right) + \\ &+ \mathbf{F}_{30}^T \cdot \left( \mathbf{A}_{23}^T \cdot \mathbf{v}_2 + \mathbf{A}_{33}^T \cdot \mathbf{v}_3 \right) + \\ &+ \mathbf{F}_{40}^T \cdot \mathbf{A}_{34}^T \cdot \mathbf{v}_3 = 0 \end{aligned} \quad (35)$$

The mathematical expression (35) can be written in the

following equivalent form:

$$\boldsymbol{\tau}^{c^T} \cdot \mathbf{v} = \mathbf{F}_0^T \cdot \mathbf{A}^T \cdot \mathbf{v} = 0 \tag{36}$$

$$\mathbf{F}_0 = \left[\mathbf{F}_{10}^T \,\vdots\, \mathbf{F}_{20}^T \,\vdots\, \mathbf{F}_{30}^T \,\vdots\, \mathbf{F}_{40}^T\right]^T \tag{37}$$

$$\mathbf{A}^T = \left[\begin{array}{c:c:c} \mathbf{A}_{11}^T & \underbrace{\mathbf{0}}_{2\times 3} & \underbrace{\mathbf{0}}_{2\times 3} \\ \hdashline \mathbf{A}_{12}^T & \mathbf{A}_{22}^T & \underbrace{\mathbf{0}}_{2\times 3} \\ \hdashline \underbrace{\mathbf{0}}_{2\times 3} & \mathbf{A}_{23}^T & \mathbf{A}_{33}^T \\ \hdashline \underbrace{\mathbf{0}}_{2\times 3} & \underbrace{\mathbf{0}}_{2\times 3} & \mathbf{A}_{34}^T \end{array}\right] \tag{38}$$

From the relation (36) we can easily deduce the expression of the constraint forces torque:

$$\boldsymbol{\tau}^c = \mathbf{A} \cdot \mathbf{F}_0 \tag{39}$$

In the relation (39) the expression of the matrix $\mathbf{A}$ is given by the relation (38) and the expression of the column matrix $\mathbf{F}_0$ is given by the relation (37).The link relationship between the first order kinematical parameters of the mechanism elements can be deduced from the relation (36):

$$\mathbf{A}^T \cdot \mathbf{v} = \underbrace{\mathbf{0}}_{8\times 1} \tag{40}$$

The matrix relationship (40) is equivalent to eight scalar relationships. The following equation can be added to the relationship (40):

$$\omega_{1z} = \omega_1 = const. \tag{41}$$

The relationships (40) and (41) can be written together in matrix form as follows:

$$\mathbf{D} \cdot \mathbf{v} = \mathbf{C} \cdot \omega_1 \tag{42}$$

$$\mathbf{D} = \left[A \,\vdots\, \mathbf{B}^T\right]^T \tag{43}$$

$$\mathbf{B} = \underbrace{\left[0 \,\vdots\, 0 \,\vdots\, 1 \,\vdots\, 0 \,\vdots\, \cdots \,\vdots\, 0\right]}_{9\times 1} \tag{44}$$

$$\mathbf{C} = \underbrace{\left[0 \,\vdots\, 0 \,\vdots\, 0 \,\vdots\, \cdots \,\vdots\, 0 \,\vdots\, 1\right]^T}_{1\times 9} \tag{45}$$

In conclusion the matrix $\mathbf{D}$ will have the following expression:

$$\mathbf{D} = \left[\begin{array}{c:c:c} \mathbf{A}_{11}^T & \underbrace{\mathbf{0}}_{2\times 3} & \underbrace{\mathbf{0}}_{2\times 3} \\ \hdashline \mathbf{A}_{12}^T & \mathbf{A}_{22}^T & \underbrace{\mathbf{0}}_{2\times 3} \\ \hdashline \underbrace{\mathbf{0}}_{2\times 3} & \mathbf{A}_{23}^T & \mathbf{A}_{33}^T \\ \hdashline \underbrace{\mathbf{0}}_{2\times 3} & \underbrace{\mathbf{0}}_{2\times 3} & \mathbf{A}_{34}^T \\ \hdashline \mathbf{B}_1 & \mathbf{B}_2 & \mathbf{B}_2 \end{array}\right] \tag{46}$$

$$\mathbf{B}_1 = \left[0 \,\vdots\, 0 \,\vdots\, 1\right] \tag{47}$$

$$\mathbf{B}_2 = \mathbf{B}_3 = \left[0 \,\vdots\, 0 \,\vdots\, 0\right] \tag{48}$$

In the next paragraph the differential equations characterizing from the kinematical point of view the movement of the articulated quadrilateral mechanism will be established.

## 3. ESTABLISHING DIFFERENTIAL EQUATIONS CHARACTERIZING THE MOTION OF THE ARTICULATED QUADRILATERAL MECHANISM

In order to determine the differential equations describing cinematically the movement of the articulated quadrilateral mechanism, the relation (42) will be derived twice in relation to the time and it will be obtained:

$$\mathbf{D} \cdot \ddot{\mathbf{v}} + 2 \cdot \dot{\mathbf{D}} \cdot \dot{\mathbf{v}} + \ddot{\mathbf{D}} \cdot \mathbf{v} = \underbrace{\mathbf{0}}_{9\times 1} \tag{49}$$

$$\dot{\mathbf{D}} = \left[\begin{array}{c:c:c} \dot{\mathbf{A}}_{11}^T & \underbrace{\mathbf{0}}_{2\times 3} & \underbrace{\mathbf{0}}_{2\times 3} \\ \hdashline \dot{\mathbf{A}}_{12}^T & \dot{\mathbf{A}}_{22}^T & \underbrace{\mathbf{0}}_{2\times 3} \\ \hdashline \underbrace{\mathbf{0}}_{2\times 3} & \dot{\mathbf{A}}_{23}^T & \dot{\mathbf{A}}_{33}^T \\ \hdashline \underbrace{\mathbf{0}}_{2\times 3} & \underbrace{\mathbf{0}}_{2\times 3} & \dot{\mathbf{A}}_{34}^T \\ \hdashline \underbrace{\mathbf{0}}_{1\times 3} & \underbrace{\mathbf{0}}_{1\times 3} & \underbrace{\mathbf{0}}_{1\times 3} \end{array}\right] \tag{50}$$

$$\ddot{\mathbf{D}} = \begin{bmatrix} \ddot{\mathbf{A}}_{11}^T & \underset{2\times3}{\mathbf{0}} & \underset{2\times3}{\mathbf{0}} \\ \ddot{\mathbf{A}}_{12}^T & \ddot{\mathbf{A}}_{22}^T & \underset{2\times3}{\mathbf{0}} \\ \underset{2\times3}{\mathbf{0}} & \ddot{\mathbf{A}}_{23}^T & \ddot{\mathbf{A}}_{33}^T \\ \underset{2\times3}{\mathbf{0}} & \underset{2\times3}{\mathbf{0}} & \ddot{\mathbf{A}}_{34}^T \\ \underset{1\times3}{\mathbf{0}} & \underset{1\times3}{\mathbf{0}} & \underset{1\times3}{\mathbf{0}} \end{bmatrix} \tag{51}$$

$$\dot{\mathbf{A}}_{11}^T = \left[\begin{array}{c|c|c} 0 & 0 & 0 \\ \hline 0 & 0 & 0 \end{array}\right] \tag{52}$$

$$\dot{\mathbf{A}}_{12}^T = \left[\begin{array}{c|c|c} 0 & 0 & -\dot{p}_{1y} \\ \hline 0 & 0 & \dot{p}_{1x} \end{array}\right] \tag{53}$$

$$\dot{\mathbf{A}}_{22}^T = \left[\begin{array}{c|c|c} 0 & 0 & 0 \\ \hline 0 & 0 & 0 \end{array}\right] \tag{54}$$

$$\dot{p}_{1x} = \dot{x}_{O_2} - \dot{x}_{O_1} = v_{O_2x} - v_{O_1y} \tag{55}$$

$$\dot{p}_{1y} = \dot{y}_{O_2} - \dot{y}_{O_1} = v_{O_2y} - v_{O_1y} \tag{56}$$

$$\dot{\mathbf{A}}_{23}^T = \left[\begin{array}{c|c|c} 0 & 0 & -\dot{p}_{2y} \\ \hline 0 & 0 & \dot{p}_{2x} \end{array}\right] \tag{57}$$

$$\dot{\mathbf{A}}_{33}^T = \left[\begin{array}{c|c|c} 0 & 0 & 0 \\ \hline 0 & 0 & 0 \end{array}\right] \tag{58}$$

$$\dot{\mathbf{A}}_{34}^T = \left[\begin{array}{c|c|c} 0 & 0 & -\dot{p}_{3y} \\ \hline 0 & 0 & \dot{p}_{3x} \end{array}\right] \tag{59}$$

$$\dot{p}_{2x} = \dot{x}_{O_3} - \dot{x}_{O_2} = v_{O_3x} - v_{O_2x} \tag{60}$$

$$\dot{p}_{2y} = \dot{y}_{O_3} - \dot{y}_{O_2} = v_{O_3y} - v_{O_2y} \tag{61}$$

$$\dot{p}_{3x} = \dot{x}_{O_4} - \dot{x}_{O_3} = -v_{O_3x} \tag{62}$$

$$\dot{p}_{3y} = \dot{y}_{O_4} - \dot{y}_{O_3} = -v_{O_3y} \tag{63}$$

$$\ddot{\mathbf{A}}_{11}^T = \left[\begin{array}{c|c|c} 0 & 0 & 0 \\ \hline 0 & 0 & 0 \end{array}\right] \tag{64}$$

$$\ddot{\mathbf{A}}_{12}^T = \left[\begin{array}{c|c|c} 0 & 0 & -\ddot{p}_{1y} \\ \hline 0 & 0 & \ddot{p}_{1x} \end{array}\right] \tag{65}$$

$$\ddot{\mathbf{A}}_{22}^T = \left[\begin{array}{c|c|c} 0 & 0 & 0 \\ \hline 0 & 0 & 0 \end{array}\right] \tag{66}$$

$$\ddot{p}_{1x} = \dot{v}_{O_2x} - \dot{v}_{O_1y} = a_{O_2x} - a_{O_1x} \tag{67}$$

$$\ddot{p}_{1y} = \dot{v}_{O_2y} - \dot{v}_{O_1y} = a_{O_2y} - a_{O_1y} \tag{68}$$

$$\ddot{\mathbf{A}}_{23}^T = \left[\begin{array}{c|c|c} 0 & 0 & -\ddot{p}_{2y} \\ \hline 0 & 0 & \ddot{p}_{2x} \end{array}\right] \tag{69}$$

$$\ddot{\mathbf{A}}_{33}^T = \left[\begin{array}{c|c|c} 0 & 0 & 0 \\ \hline 0 & 0 & 0 \end{array}\right] \tag{70}$$

$$\ddot{\mathbf{A}}_{34}^T = \left[\begin{array}{c|c|c} 0 & 0 & -\ddot{p}_{3y} \\ \hline 0 & 0 & \ddot{p}_{3x} \end{array}\right] \tag{71}$$

$$\ddot{p}_{2x} = \dot{v}_{O_3x} - \dot{v}_{O_2x} = a_{O_3x} - a_{O_2x} \tag{72}$$

$$\ddot{p}_{2y} = \dot{v}_{O_3y} - \dot{v}_{O_2y} = a_{O_3y} - a_{O_2y} \tag{73}$$

$$\ddot{p}_{3x} = \dot{v}_{O_4x} - \dot{v}_{O_3x} = -a_{O_3x} \tag{74}$$

$$\ddot{p}_{3y} = \dot{v}_{O_4y} - \dot{v}_{O_3y} = -a_{O_3y} \tag{75}$$

$$\dot{\mathbf{v}} = \mathbf{a} = \left[\dot{\mathbf{v}}_1^T \;\vdots\; \dot{\mathbf{v}}_2^T \;\vdots\; \dot{\mathbf{v}}_3^T\right]^T \tag{76}$$

$$\dot{\mathbf{v}} = \mathbf{a} = \left[\mathbf{a}_1^T \;\vdots\; \mathbf{a}_2^T \;\vdots\; \mathbf{a}_3^T\right]^T \tag{77}$$

$$\dot{\mathbf{v}}_1 = \mathbf{a}_1 = \left[\dot{v}_{O_1x} \;\vdots\; \dot{v}_{O_1y} \;\vdots\; \dot{\omega}_{1z}\right]^T \tag{78}$$

$$\dot{\mathbf{v}}_1 = \mathbf{a}_1 = \left[a_{O_1x} \;\vdots\; a_{O_1y} \;\vdots\; \varepsilon_{1z}\right]^T \tag{79}$$

$$\dot{\mathbf{v}}_2 = \mathbf{a}_2 = \left[\dot{v}_{O_2x} \;\vdots\; \dot{v}_{O_2y} \;\vdots\; \dot{\omega}_{2z}\right]^T \tag{80}$$

$$\dot{\mathbf{v}}_2 = \mathbf{a}_2 = \left[a_{O_2x} \;\vdots\; a_{O_2y} \;\vdots\; \varepsilon_{2z}\right]^T \tag{81}$$

$$\dot{\mathbf{v}}_3 = \mathbf{a}_3 = \left[\dot{v}_{O_3x} \;\vdots\; \dot{v}_{O_3y} \;\vdots\; \dot{\omega}_{3z}\right]^T \tag{82}$$

$$\dot{\mathbf{v}}_3 = \mathbf{a}_3 = \left[a_{O_3x} \;\vdots\; a_{O_3y} \;\vdots\; \varepsilon_{3z}\right]^T \tag{83}$$

The matrix relation (49) represents a system of second order differential equations written in matrix form. It will be transformed into a system of eighteen differential equations of the first order. In order to do this, the following substitution will be made:

$$\dot{\mathbf{v}} = \mathbf{a} \tag{84}$$

The relationship (84) will be replaced in the relation (49) and it will be obtained:

$$\mathbf{D}\cdot\dot{\mathbf{a}} + 2\cdot\dot{\mathbf{D}}\cdot\mathbf{a} + \ddot{\mathbf{D}}\cdot\mathbf{v} = \underset{9\times1}{\mathbf{0}} \tag{85}$$

$$\dot{\mathbf{a}} = \left[\dot{\mathbf{a}}_1^T \mid \dot{\mathbf{a}}_2^T \mid \dot{\mathbf{a}}_3^T\right]^T \tag{86}$$

$$\dot{\mathbf{a}}_1 = \left[\dot{a}_{O_1x} \mid \dot{a}_{O_1y} \mid \dot{\varepsilon}_{1z}\right]^T \tag{87}$$

$$\dot{\mathbf{a}}_2 = \left[\dot{a}_{O_2x} \mid \dot{a}_{O_2y} \mid \dot{\varepsilon}_{2z}\right]^T \tag{88}$$

$$\dot{\mathbf{a}}_3 = \left[\dot{a}_{O_3x} \mid \dot{a}_{O_3y} \mid \dot{\varepsilon}_{3z}\right]^T \tag{89}$$

The terms appearing in the relationship (85) are generally dependent on the position parameters that are unknown. Between the position kinematical parameters and the velocities (kinematical parameters of the first order) the following matrix relationship can be written:

$$\dot{\mathbf{x}} = \mathbf{v} \tag{90}$$

$$\dot{\mathbf{x}} = \left[\dot{\mathbf{x}}_1 \mid \dot{\mathbf{x}}_2 \mid \dot{\mathbf{x}}_2\right]^T \tag{91}$$

$$\dot{\mathbf{x}}_1 = \left[\dot{x}_{O_1} \mid \dot{y}_{O_1} \mid \dot{\varphi}_1\right]^T \tag{92}$$

$$\dot{\mathbf{x}}_2 = \left[\dot{x}_{O_2} \mid \dot{y}_{O_2} \mid \dot{\varphi}_2\right]^T \tag{93}$$

$$\dot{\mathbf{x}}_3 = \left[\dot{x}_{O_3} \mid \dot{y}_{O_3} \mid \dot{\varphi}_3\right]^T \tag{94}$$

Matrix relationships (84), (85) and (90) form a system of twenty-seven differential equations of the first order with twenty-seven unknowns. This system will be solved using numerical integration methods.

## 4. SOLVING THE SYSTEM OF DIFFERENTIAL EQUATIONS AND OBTAINING RESULTS

The numerical solving of a twenty-seven differential equations system is quite difficult. For this reason, a computing program was developed using MATLAB software. The following input data are required to run the program:

$$l_1 = 1\,[meters] \tag{95}$$

$$l_2 = 3\,[meters] \tag{96}$$

$$l_3 = 4\,[meters] \tag{97}$$

$$l_4 = 5\,[meters] \tag{98}$$

$$\omega_1 = 10[radians/\sec.] \tag{99}$$

The following initial conditions are also required:

$$x_{O_1}^0 = y_{O_1}^0 = 0[meters] \tag{100}$$

$$\varphi_1^0 = 0[radians] \tag{101}$$

$$x_{O_2}^0 = l_1 = 1[meters] \tag{102}$$

$$y_{O_2}^0 = 0[meters] \tag{103}$$

$$\varphi_2^0 = 1.1864[radians] \tag{104}$$

$$x_{O_3}^0 = 2.125[meters] \tag{105}$$

$$y_{O_3}^0 = 2.7810744[meters] \tag{106}$$

$$\varphi_3^0 = -0.7688[radians] \tag{107}$$

$$v_{O_1x}^0 = v_{O_1y}^0 = 0[meters/\sec.] \tag{108}$$

$$\omega_{1z}^0 = 10[radians/\sec.] \tag{109}$$

$$v_{O_2x}^0 = 0[meters/\sec.] \tag{110}$$

$$v_{O_2y}^0 = 10[meters/\sec.] \tag{111}$$

$$\omega_{2z}^0 = -2.5[radians/\sec.] \tag{112}$$

$$v_{O_3x}^0 = 6.29568[meters/\sec.] \tag{113}$$

$$v_{O_3y}^0 = 7.1875[meters/\sec.] \tag{114}$$

$$\omega_{3z}^0 = -2.5[radians/\sec.] \tag{115}$$

$$a_{O_1x}^0 = a_{O_1y}^0 = 0[meters/\sec^2] \tag{116}$$

$$\varepsilon_{1z}^0 = 0[radians/\sec^2] \tag{117}$$

$$a_{O_2x}^0 = -100[meters/\sec^2] \tag{118}$$

$$a_{O_2y}^0 = 0[meters/\sec^2] \tag{119}$$

$$\varepsilon_{2z}^0 = -32.30541[radians/\sec^2] \tag{120}$$

$$a_{O_3x}^0 = -17.1875[meters/\sec^2] \tag{121}$$

$$a_{O_3y}^0 = -53.7253[meters/\sec^2] \tag{122}$$

$$\varepsilon_{3z}^0 = 12.6412[radians/\sec^2] \tag{123}$$

Coordinates, velocity and acceleration of the $O_4$ point of the mechanism are obviously equal to zero for the entire duration of the movement because it is fixed. The

computing program is running taking into account the input data and initial conditions and the results presented in the figures below (Fig.3-Fig.5) will be obtained. The angular velocity of the leading element "1" is considered constant throughout the movement. For this reason, the variation of the magnitude of the $\varphi_1$ angle relative to time is linear and its angular velocity is constant is equal to zero all the time of the mechanism movement.

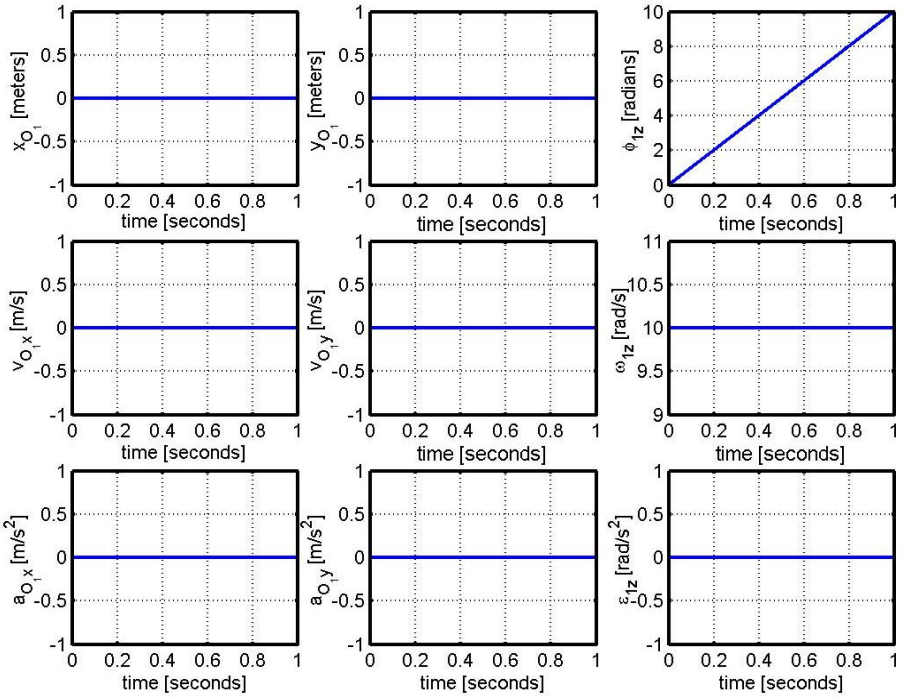


**Figure 3. Movement of the "1" element of the mechanism in relation to time**

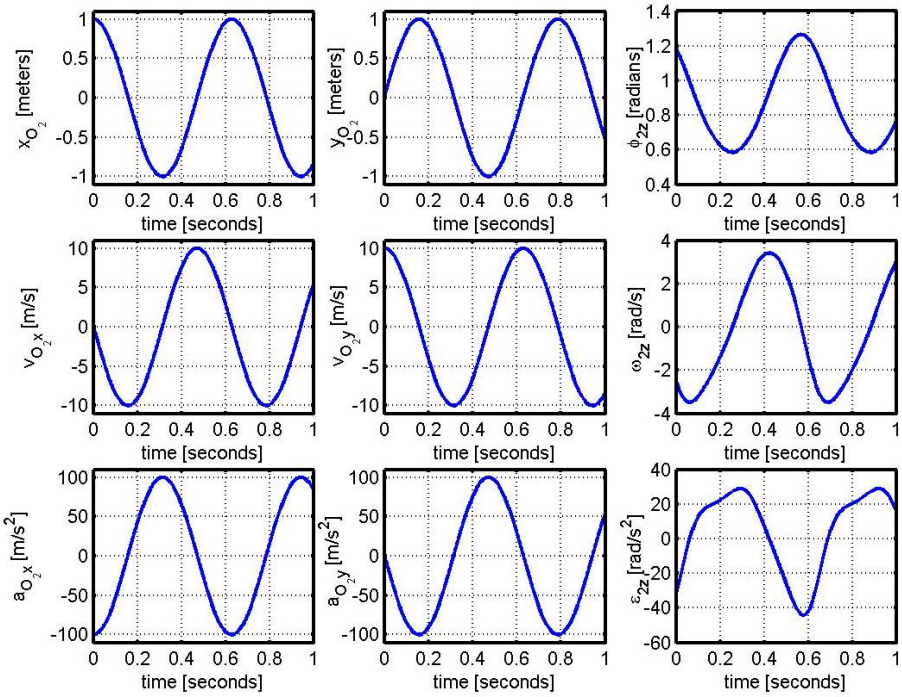


**Figure 4. Movement of the "2" element of the mechanism in relation to time**

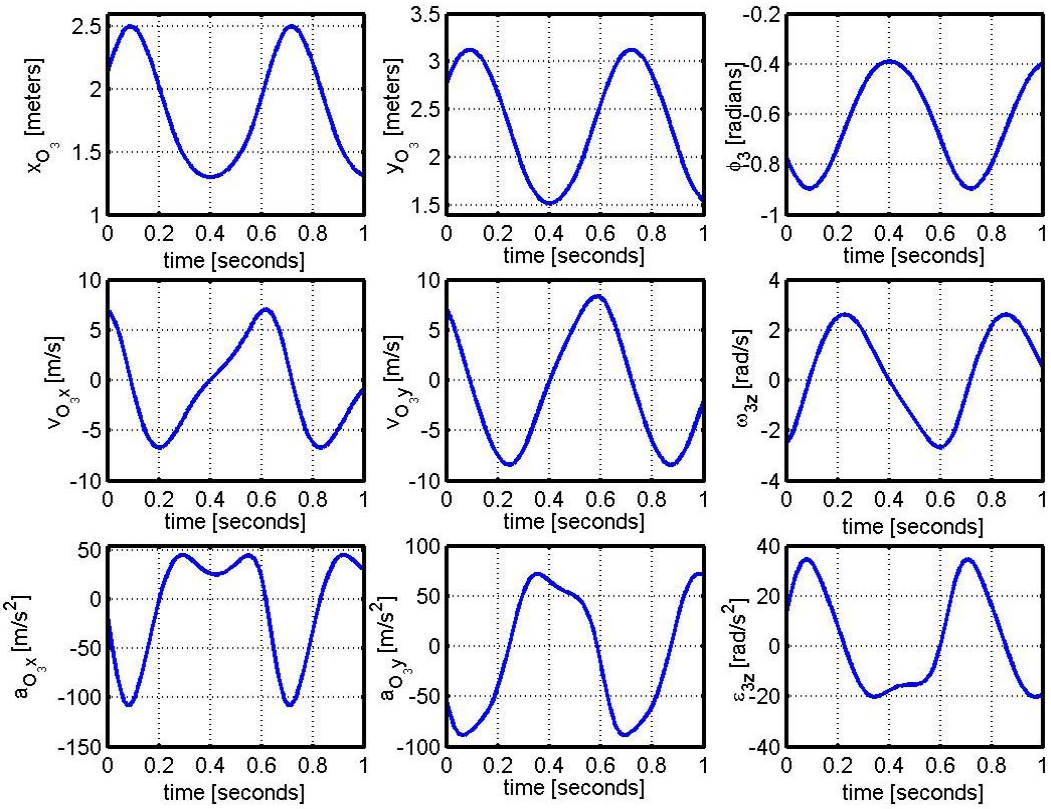


**Figure 5. Movement of the "3" element of the mechanism in relation to time**

## 5. CONCLUSIONS

A mathematical model was developed in the paper, with which the complete kinematics analysis of the articulated quadrilateral mechanism was performed.

Relationships between kinematical parameters of the elements of the mechanism were established using the principle of virtual mechanical work.

Using the kinematical analysis method presented in the paper, one can determine the position, velocity and acceleration of any point that belongs to any element of the mechanism.

## REFERENCES

[1] Vâlcovici V., Bălan Şt., Voinea R., Mecanica Teoretică, Bucureşti: Editura Tehnică, 1968

[2] Viorel Handra Luca, Ion Aurel Stoica, Introducere în teoria mecanismelor, Cluj-Napoca: Editura Dacia, 1982, pp.84

[3] Christian Pelecudi, Dezideriu Maroş, Vasile Merticaru, Nicolae Pandrea, Ion Simionescu, Mecanisme, Bucureşti: Editura Tehnică, 1983, pp. 206-208

[4] Voinea R., Stroe I., A general method for kinematics pair synthesis, Mechanism and Machine Theory, Elsevier 1995; 30(3), pp. 461-470.

[5] Ştefan Staicu, Mecanica Teoretică, Bucureşti:Editura Didactică şi Pedagogică R.A., 1998

[6] Florin Bauşic, Mecanica Teoretică.Cinematica, Bucureşti: Editura Conspres, 2004

[7] Staicu S., Kinematics of translation-rotation hybrid parallel robot, Romanian Journal of Technical Sciences-Applied Mechanics, 2015; 60, pp. 171-183.

[8] Tătaru V.D., Tătaru M.B., Incremental numerical method used for the cinematic analysis of the four-bar linkage mechanism, Romanian Journal of Technical Sciences-Applied Mechanics, 2016; 61(3), pp. 222-231.

The Scientific Bulletin of VALAHIA University
MATERIALS and MECHANICS –Vol. 17, No. 16

DOI 10.2478/bsmm-2019-0008

# UNFOLDINGS OF THE CIRCULAR CYLINDERS HAVING NON-COMPETITIVE AXLES

**Carmen POPA[1*], Violeta Anghelina[1], Octavian MUNTEANU[2]**

[1] Valahia University of Targoviste, Faculty of Materials Engineering and Mechanics, 13 Aleea Sinaia Street, Targoviste, Romania, [2] KPD Construction Software, Halen, Belgium

E-mail: * carmenpopa2001@yahoo.com

**Abstract**: *The descriptive geometry constitues the foundation of the engineering sciences, so necessary to the specialists of this field. The aim of this paper is to establish the intersection curve between two cylinders and their unfoldings, by using the programmes:AutoCAD and Mathematica. We used the classical method and we first establish the intersection curve and then the cylinders unfoldings. To do this, we used the AutoCAD program. The same unfoldings can be obtained by introducing directly the curve equations (which are inferred) in Mathematica program.*

**Keywords:** *unfolding, intersection curve, generator*

## 1. THE CLASSIC METHOD OF DETERMINING THE CYLINDERS UNFOLDINGS

The calculation of the cylinders unfoldings has many practical applications, especially in the connecting of the pipes of equal or different diameters. Thus in the Figure 1 is represented the intersection curve between the $C_1$ (D = 40 mm) and $C_2$ (d = 14 mm)cylinders [1-3].

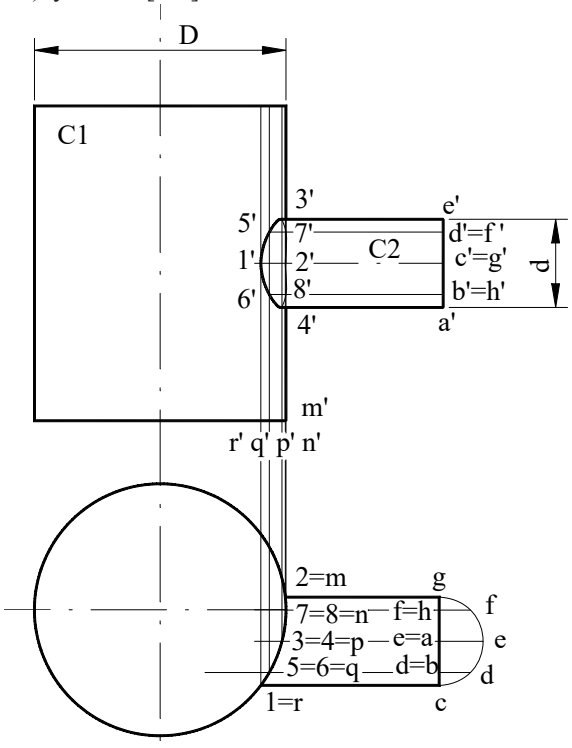


**Figure 1. The intersection curve between the cylinders**

The intersection curve is determined at the intersection of the generators from the A, B, ..., H and M, N, ..., R points. The elements required to construct the unfolding are in real-time purge because the cylinder generators are parallel to the projection planes.

The unfolding of the $C_1$ cylinder (Figure 2) is a rectangle whose sides are the length of the cylinder base circle, $\pi \cdot D$ and the length of the generator.

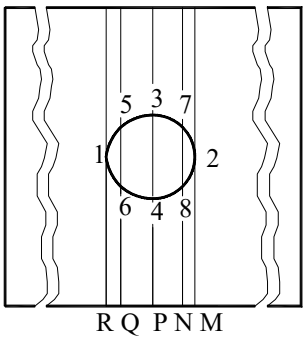


**Figure 2. The unfolding of the $C_1$ cylinder**

For transposing on the cylinder unfolding of the intersection curve, the generators from the R, Q, P, N, and M points are represented on the unfolding, measuring on the side equal with the length of the base circle, RQ = rq, QP = qp, ... , NM = nm.

On the perpendiculars of these points (cylinders generators) are the 1,2, ..., 8 points belonging to the intersection curve, measuring on the vertical projection the segments r'1 '= R1, q'6' = Q6, ...

The C2 cylinder unfolding starts by drawing the base circle that is unfolding π·d (Figure 3).

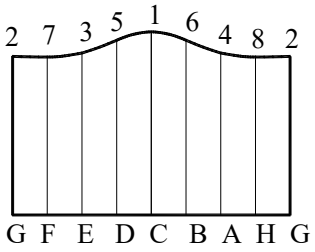


**Figure 3. The $C_2$ cylinder unfolding**

After dividing this segment into equal parts, because for the representation of the generators the base circle was also divided into equal parts, from the repeating points rises perpendiculars to which the g'2 '= G2, f'7' = F7, ..., a'4 '= A4 segments are measured.

By joining these points, the second cylinder unfolding is developed.

## 2. ANALYTICAL METHOD FOR DETERMINING THE INTERSECTION CURVES OF THE CYLINDERS

Ox and Oz axes are considered as coordinate axes for the vertical projection like in Figure 4 [4,5].
Unfolding designing involves the following phases:
- enumeration of the curve equations resulting from the intersections of the unfolded surfaces;
- enumeration of the equations of the transformations through the unfolding of the intersection curves.

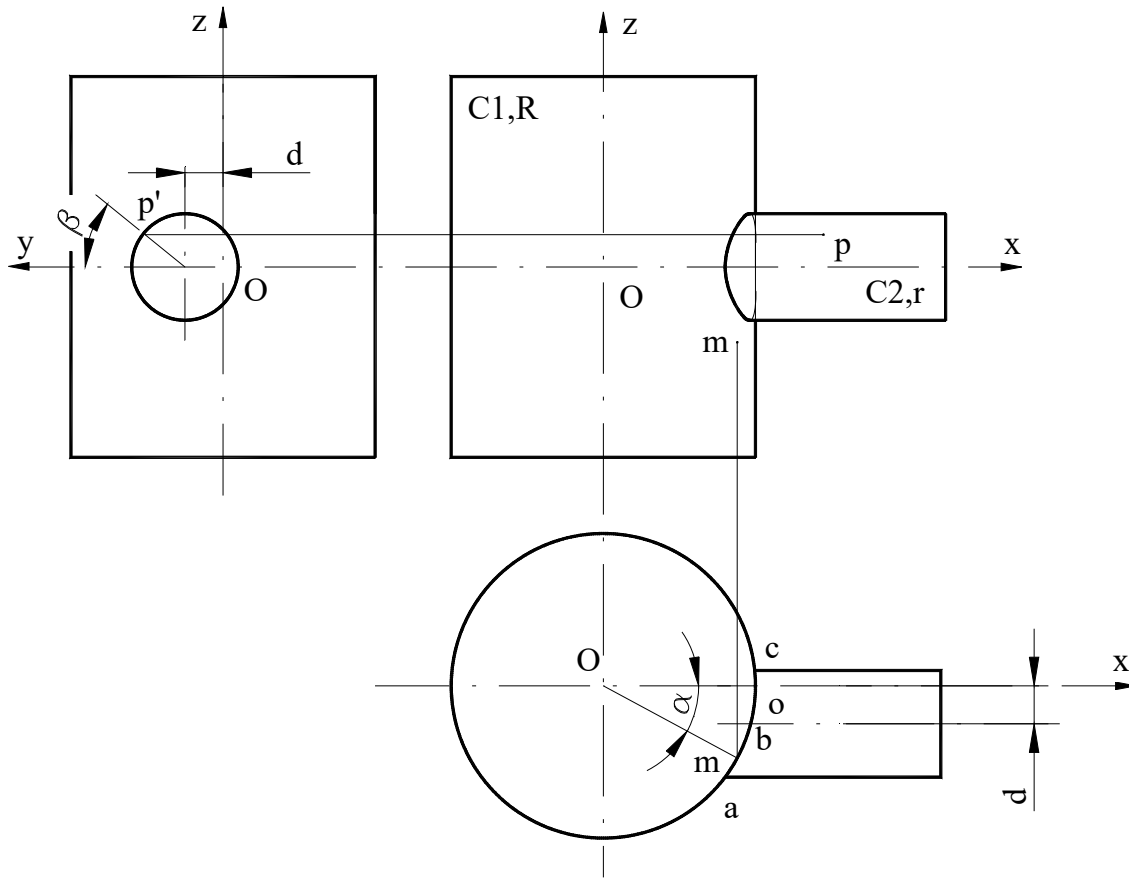


**Figure 4. The vertical projection**

### 2.1. The calculation of the intersection curve of the $C_1$ cylinder

Be a M (m, m ') point of coordinates x, y in the purge and $x_d$, $z_d$ in unfolding. The transformation of the vertical projection equation of the curve drawn on the cylinder, in the unfolded curve equation can be done by expressing the x and z coordinates of $x_d$ and $z_d$.

$$x = R \cdot \cos\alpha = R \cdot \cos\frac{x_d}{R} \quad (1)$$

$$z = z_d \quad (2)$$

The equations of the cylinders, expressed in the reference systems chosen, are:

$$C_1 : x^2 + y^2 = R^2, \quad (3)$$

$$C_2 : z^2 + (y-d)^2 = r^2. \quad (4)$$

Taking the P (p, p ') point of coordinates x and z in the purge and xd and zd in unfolding, we will have:

$$z_d = \pm\sqrt{r^2 - (R \cdot \sin\frac{x_d}{R} - d)^2} \quad (7)$$

where:

$$x_d \in \left[-arc\ oc, arc\ ao\right], \quad (8)$$

so:

$$x_d \in \left[-R\,arctg\,(d-r)/R, R\arcsin(d+r)/R\right]. \quad (9)$$

By replacing the cylinder data, we obtain the following curve (Figure 5).

```
Show[Plot[Sqrt[49 – (20 * Sin[x / 20] – 5)^2],
– Sqrt[49 – (20 * Sin[x / 20] – 5)^2]},
{x,–20 * ArcTan[1 / 5],20 * ArcSin[3 / 5]}]
AspectRatio → Automatic
```

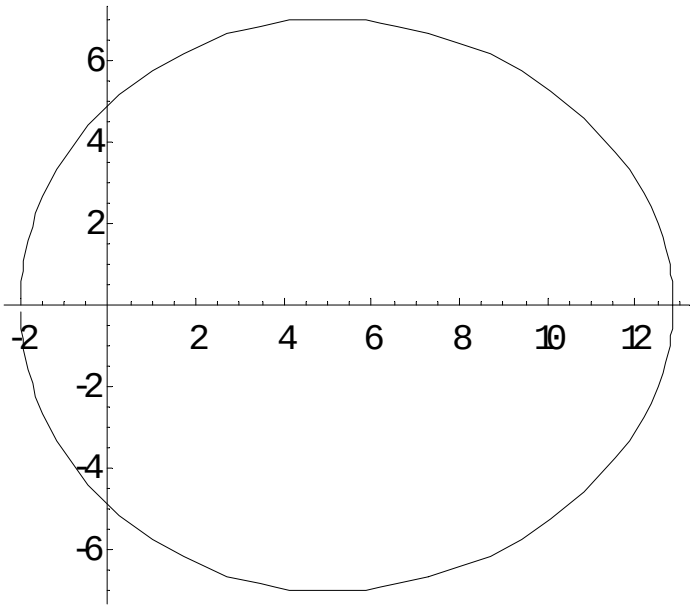


**Figure 5. The unfolding of the $C_1$ cylinder**

### 2.2. The calculation of the unfolding of the intersection curve of the $C_2$ cylinder

The equation of the intersection curve of the $C_1$ cylinder is obtained by applying the equations (1, 2) to the equation (5):

$$z_d^2 + (R \cdot \cos x_d \ \ /R)^2 - r^2 = 0 \quad (6)$$

$$x = x_d, \quad (10)$$

$$z = r \cdot \sin\beta = r \cdot \sin z_d / r. \quad (11)$$

The equation of the unfolding curve of the $C_2$ cylinder is obtained by applying the (10, 11) relations to the (5) equation:

$$x_d = \pm\sqrt{R^2 - (r \cdot \cos\frac{z_d}{r} + d)^2}\ , \qquad (12)$$

where:

$$z_d \in \left[-\pi r, \pi r\right]. \qquad (13)$$

By replacing with the cylinder data we will obtain the curve from Figure 6.

*ShowPlot*[{*Sqrt*[400 – (7 ∗ *Cos*[*z* / 7] + 5)^2,
– *Sqrt*[400 – (7 ∗ *Cos*[*z* / 7] + 5)^2]},
{*z*,–7 ∗ *Pi*,7 ∗ *Pi*}], *AspectRatio* → *Automatic*]

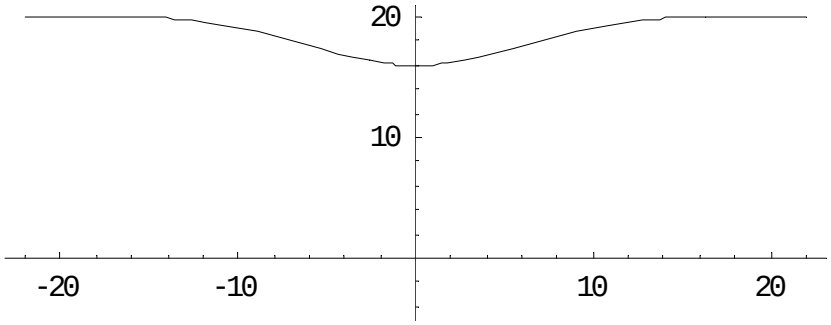


**Figure 6. The unfolding of the $C_2$ cylinder**

## 3. CONCLUSIONS

By applying the two methods, namely descriptive geometry and mathematical calculus, we get about the same curves. The mathematical computation is much more accurate.

## REFERENCES

[1] Moncea, J., Desfăşurarea suprafeţelor, Editura Tehnică, Bucureşti, 1989.

[2] Mănescu, M., Geometrie descriptivă. Aplicaţii, Editura Didactică şi Pedagogică, Bucureşti, 1995.

[3] Ivănceanu, T., Geometrie descriptivă şi desen tehnic, Editura Didactică şi Pedagogică, Bucureşti, 1979.

[4] Popa, Carmen,The classical analytical and numerical methods of establishing the oblique cylinders unfoldings, International Conference on Manufacturing Systems ICMaS, Bucureşti, 2002, tome 47, p. 553, ISBN 973-27-0932-4, ISSN 0035-4074.

[5] Popa, Carmen, Metode analitice de determinare a desfăşuratelor cilindrilor, The 27-th Annual ARA Congress, Oradea, 2002, vol. II, pag. 808, ISBN 2-553-01024-9.

The Scientific Bulletin of VALAHIA University
MATERIALS and MECHANICS –Vol. 17, No. 16

DOI 10.2478/bsmm-2019-0009

# DIRECT / REVERSE ANALOGY BETWEEN MECHANICAL SYSTEM AND RLC SERIES / PARALEL ALTERNATIVE CURRENT CIRCUITS - AC

**Cornel MARIN*, Ion Florin POPA****

Valahia University of Targoviste, Faculty of Materials Engineering and Mechanics, 13 Aleea Sinaia Street, Targoviste, Romania

Email: * marin_cor@yahoo.com , ** p.florin.ro@gmail.com

**Abstract:** *There is a direct analogy between the mechanical and electrical phenomena related to vibrations and electromagnetic oscillations in the RLC series AC circuits and an inverse analogy to the electromagnetic oscillations in the RLC parallel alternative current (AC) circuits. Direct analogy RLC series AC circuit refers to the connection between complex velocity and complex electrical intensity, mechanical impedance and electrical impedance, etc. Reverse analogy RLC parallel AC circuits refers to the connection between complex velocity and complex electrical voltage, mechanical impedance and electrical admission, etc.*

**Keywords:** *vibrations of mechanical systems, electromagnetic oscillations, direct and reverse analogy AC circuits*

## 1. DIRECT ANALOGY

### 1.1. General relationships of intensity and voltage in the RLC series AC circuits

The RLC series AC circuit contain resistive element, capacitive element (capacitor) and inductive element (coil) connected in series, being powered by a voltage source $U_0 \cdot cos(\omega t)$ (Figure 1).

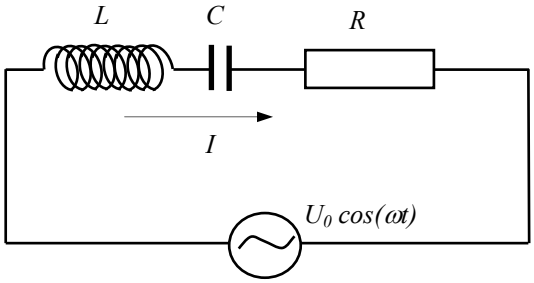


**Figure 1.**

The RLC series AC circuit behaves similarly to the VOIGT KELVIN mechanical system containing a NEWTON dissipative element $c$ and a HOOKE elastic member with stiffness $k$ bound in parallel to an inertial mass element $m$, under the action of a harmonic disturbing force $F_0 \cdot cos(\omega t)$ (Figure 2).

The RLC series AC circuit consists of a resistor with electrical resistance $R$, a coil having the inductance $L$ and a capacitor having the capacitance $C$, being fed to a voltage source of the alternating current: $U(t)=U_0 \cdot cos(\omega t)$ (Figure 1).

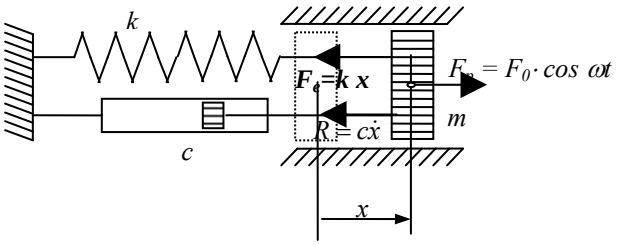


**Figure 2.**

Take into account the existing relationships between the current intensity $I(t)$ and the voltage drops for the three elements above:

$$U_R(t) = R \cdot I(t);$$
$$U_L(t) = -\frac{d\Phi}{dt} = L \cdot \frac{dI(t)}{dt}; \quad (1)$$
$$U_C(t) = \frac{Q(t)}{C} = \frac{1}{C} \cdot \int I(t)dt$$

From relations (1) are deduced the properties of the current intensity in the RLC circuit:

1. The current intensity $I(t)$ is the ratio between the voltage at the resistor terminals and the resistance $R$;

2. The current intensity derivative *I(t)* is calculate as the ratio between the voltage measured at the coil terminals and the inductance *L*;

3. The integral of the intensity current *I(t)* is equal to the product of the electric charge on the capacitor plates *Q(t)* and the capacitance *C*; the intensity of the electric current is therefore derived in relation to the time of the electrical charge in the capacitor:

$$I(t)=\frac{dQ(t)}{dt} \tag{2}$$

Applying Kirchhoff's Theorem II, to the RLC circuit of Figure 1:

$$U_0(t)=U_L(t)+U_C(t)+U_R(t) \tag{3}$$

and replacing the voltage drops on the three elements (1):

$$L\cdot\frac{dI(t)}{dt}+\frac{1}{C}\cdot\int I(t)dt+R\cdot I(t)=U_0\cdot cos(\omega t) \tag{4}$$

The differential current equation in the RLC series AC circuit was obtained.

Taking into account the current intensity property in the series RLC circuit (2) and deriving the differential equation (4) we obtain the differential equation of the electric charge Q (t) from an AC series circuit:

$$L\cdot\ddot{Q}(t)+R\cdot\dot{Q}(t)+\frac{1}{C}Q(t)=U_0\cdot cos(\omega t) \tag{5}$$

### 1.2 The complex calculus of current and voltage voltages of the RLC series AC circuit

Using the complex calculation, the differential equation of the electric charge (5) is written:

$$L\cdot\ddot{q}(t)+R\cdot\dot{q}(t)+\frac{1}{C}q(t)=U_0\cdot e^{j\omega t} \tag{6}$$

where $q(t)=q_0\cdot e^{j\omega t}$ is *the complex electric charge*

Replacing complex electrical charge derivatives

$\dot{q}(t)=q_0\cdot j\omega\cdot e^{j\omega t}$; $\ddot{q}(t)=-q_0\cdot\omega^2\cdot e^{j\omega t}$

in equation (6), the complex amplitude of the electrical charge is immediately obtained:

$$q_0=\frac{U_0}{\left(\frac{1}{C}-L\cdot\omega^2\right)+j\omega\cdot R} \tag{7}$$

***a)*** the complex electrical charge varies according a harmonic law of form:

$$q(t)=\frac{U_0\cdot e^{j\omega t}}{\left(\frac{1}{C}-L\cdot\omega^2\right)+j\cdot R\cdot\omega} \tag{8}$$

$$q(t)=Q_0\cdot e^{j(\omega t-\theta)}$$

where:

$$Q_0=\frac{U_0}{\sqrt{\left(\frac{1}{C}-L\cdot\omega^2\right)^2+R^2\omega^2}}; \tag{9}$$

$$tan\,\theta=\frac{R}{\frac{1}{C\cdot\omega}-L\cdot\omega}$$

*b) the complex intensity of the electric current* ***i(t)*** is derived in relation to the time of complex electrical charge *q(t)*:

$$i(t)=\frac{dq(t)}{dt}=\frac{U_0\cdot e^{j\omega t}}{R-j\left(\frac{1}{C\cdot\omega}-L\cdot\omega\right)} \tag{10}$$

$$i(t)=I_0\cdot e^{j(\omega t+\varphi)}$$

where:

$$I_0=\frac{U_0}{\sqrt{R^2+\left(L\cdot\omega-\frac{1}{C\cdot\omega}\right)^2}} \tag{11}$$

$$tan\,\varphi=\frac{\frac{1}{C\cdot\omega}-L\cdot\omega}{R}$$

We note the *capacitor reactance* $X_C$:

$$X_C=\frac{1}{C\omega} \tag{12}$$

*and coil reactance* $X_L$: $\quad X_L=L\omega$ (13)

*c) the electrical impedance* $Z$ of the RLC AC circuit is written:

$$Z=R-j\left(\frac{1}{C\cdot\omega}-L\cdot\omega\right); \tag{14}$$

$$|Z|=\sqrt{(X_C-X_L)^2+R^2}$$

The electrical charge of the capacitor *Q(t)* and the electric power *I(t)* have the expressions:

$$Q(t)=Q_0\cdot cos(\omega t-\theta) \tag{15}$$

$$I(t)=\omega\cdot Q_0\cdot cos\left(\omega t-\theta+\frac{\pi}{2}\right) \tag{16}$$

where:

$$Q_0=\frac{U_0}{\omega\cdot|Z|};\quad I_0=\frac{U_0}{|Z|};\quad \varphi=\frac{\pi}{2}-\theta \tag{16}$$

### 1.3. Phasor representation of current and voltages in the RLC series AC circuit

*a) the complex voltage* $u(t)=U_0\cdot e^{j\omega t}$ is represented in the complex plane by a phasor $U_0$ rotating in the trigonometric sense with the angular velocity $\omega$. At moment t the phasor $U_0$ makes the angle $\omega t$ with the real axis; the real voltage $U_0\cdot cos\omega t$ represents the projection of the phasor $U_0$ on the real axis and the

complex voltage $j \cdot U_0 \cdot \sin\omega t$ the projection on the imaginary axis (Fig.3). The expression of the complex supply voltage $u_0(t)$ is:

$$u_0(t) = U_0 \cdot \cos(\omega t) + j \cdot U_0 \cdot \sin(\omega t)$$
$$u_0(t) = U_0 \cdot e^{j\omega t} \quad (17)$$

*b) the complex intensity i(t)* given by the relation (10) is represented in the complex plane by a phasor $I_0$ which rotates with the phasor $U_0$ in the trigonometric sense with the same angular velocity $\omega$, being phased in front of the phasor $U_0$ with the angle $\varphi$ (Figure 3):

$$i(t) = I_0 \cdot e^{j(\omega t+\varphi)}; \qquad I_0 = \frac{U_0}{|Z|};$$
$$|Z| = \sqrt{(X_C - X_L)^2 + R^2}; \qquad tan\varphi = \frac{X_C - X_L}{R} \quad (18)$$

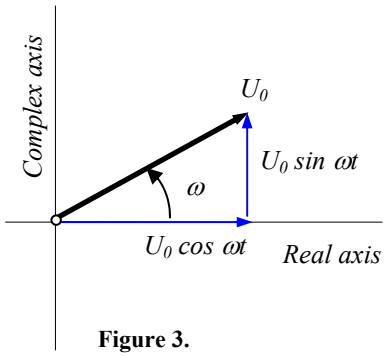


**Figure 3.**

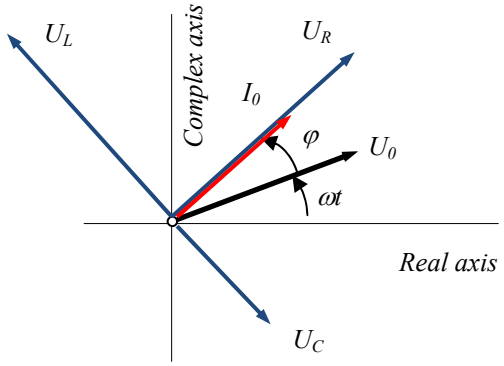


**Figure 4.**

Writing Kirchhoff's theorem II (2) into the complex and replacing the expressions of the complex derivative and integrative *i(t),* is obtained the same expression of complex intensity *i(t)*:

$$L \cdot \frac{di(t)}{dt} + \frac{1}{C} \cdot \int i(t)dt + R \cdot i(t) = U_0 \cdot e^{j\omega t}$$
$$\frac{di(t)}{dt} = j \cdot \omega \cdot I_0 \cdot e^{j(\omega t+\varphi)};$$
$$\int i(t)dt = \frac{I_0 \cdot e^{j(\omega t+\varphi)}}{j \cdot \omega} \Rightarrow i(t) = \frac{U_0 \cdot e^{j\omega t}}{Z};$$

$$Z = R - j\left(\frac{1}{C \cdot \omega} - L \cdot \omega\right) \quad (19)$$

*c) the complex voltage at resistor $u_R$ (t)* is the product of complex intensity *i(t)* and resistance *R*; this is represented in the complex plane by a $U_R$ phasor rotating in the trigonometric sense with angular velocity ω being in phase with the phasor $I_0$ (fig.4):

$$u_R(t) = R \cdot I_0 \cdot e^{j(\omega t+\varphi)} \quad (20)$$

*d. The complex voltage on the capacitor $u_C(t)$* is the ratio between the complex intensity integral and the capacity of the capacitor *C* and is represented in the complex plane by a phasor $U_C$ rotating in the trigonometric sense with the same angular velocity $\omega$ being following the intensity phasor $I_0$ being phased in behind with $\pi/2$ radians (figure 4):

$$u_C(t) = \frac{1}{C}\int i(t) \cdot dt = \frac{I_0}{j \cdot \omega \cdot C} e^{j(\omega t+\varphi)}$$
$$\Rightarrow u_C(t) = \frac{I_0}{\omega \cdot C} e^{j\left(\omega t+\varphi-\frac{\pi}{2}\right)} \quad (21)$$

*e. The complex voltage at the coil terminals $u_L(t)$* is the product of the inductance L of the coil and the complex intensity derivative *i(t)* and is represented in the complex plane by a $U_L$ phasor rotating in the trigonometric sense with the same angular velocity $\omega$ being offset in front of intensity phasor $I_0$ and $U_R$ being phased in front with $\pi/2$ radians (Figure 4):

$$u_L(t) = L \cdot \frac{di(t)}{dt} = I_0 \cdot j \cdot L\omega \cdot e^{j(\omega t+\varphi)}$$
$$\Rightarrow u_L(t) = I_0 \cdot L\omega \cdot e^{j\left(\omega t+\varphi+\frac{\pi}{2}\right)} \quad (22)$$

### 1.4. The electrical impedance of the RLC series AC circuit

In the case of the RLC series, the electric impedance *Z*, is equal to the ratio between the complex supply voltage $u_0(t)$ and the complex intensity *i(t)*:

$$Z = \frac{u_0(t)}{i(t)} = \frac{U_0}{I_0} \cdot e^{-j\varphi} \quad (23)$$

The study of electromagnetic oscillations in the RLC series circuit AC with the electric impedance *Z* allows an intensity analysis due to applied harmonic voltages.

The impedance method is based on:

- the *resistive impedance R*, according to the relation (20), a real number that does not depend on the frequency of the supply voltage:

$$Z_R = \frac{u_R(t)}{i(t)} = R \quad (24)$$

- the *capacitive impedance $X_C$,* according to the relation (21), a complex number depending inversely proportional to the frequency of the supply voltage:

$$Z_C = \frac{u_C(t)}{i(t)} = \frac{1}{j \cdot C \cdot \omega} = -j \cdot X_C \quad (25)$$

- the *inductive impedance* $X_L$ according to the relation (22) which is a complex number that depends directly on the frequency of the supply voltage:

$$Z_L = \frac{u_L(t)}{i(t)} = j \cdot L \cdot \omega = j \cdot X_L \quad (26)$$

*The electrical impedance of the RLC series AC is* calculated by the sum of the impedances of the three elements, since the complex relationship of the voltages (3) can also be written:

$$u_L(t) + u_R(t) + u_C(t) = u_0(t)$$
$$\Rightarrow Z_L \cdot i(t) + Z_R \cdot i(t) + Z_C \cdot i(t) = Z \cdot i(t) \quad (27)$$
$$\Rightarrow Z = Z_L + Z_L + Z_L$$

*The electrical impedance of the RLC series AC is:*

$$Z = R - j\left(\frac{1}{C \cdot \omega} - L \cdot \omega\right) = R - j(X_C - X_L);$$
$$Z = |Z| \cdot (\cos\varphi - j \cdot \sin\varphi)$$
$$|Z| = \sqrt{(X_C - X_L)^2 + R^2}; \quad (28)$$
$$\tan\varphi = \frac{X_C - X_L}{R}$$

If the complex phases, the phasors $U_R$, $U_L$, $U_C$, $I_0$ and $U_0$ are represented so that $I_0$ and $U_R$ coincide with the real axis, the constructions of Figure 5 are obtained:

- for $U_L < U_C$ (Fig. 5.a), the current $I_0$ is in front of the supply voltage $U_0$ with the angle $\varphi$ and we have a capacitive RLC circuit;
- for $U_L > U_C$ (Fig. 5.b), the current $I_0$ is behind of the supply voltage $U_0$ with the angle $\varphi$ and we have an inductive series RLC circuit;
- for $U_L = U_C$ (Fig. 5.c), the current $I_0$ is in phase with the supply voltage $U_0$ - the circuit is resonant and we have a resistive RLC circuit

The condition for resonance is imposed by equality:

$X_L = X_C$:

$$L \cdot \omega = \frac{1}{C \cdot \omega} \Rightarrow \omega_r = \frac{1}{\sqrt{L \cdot C}} \quad (29)$$

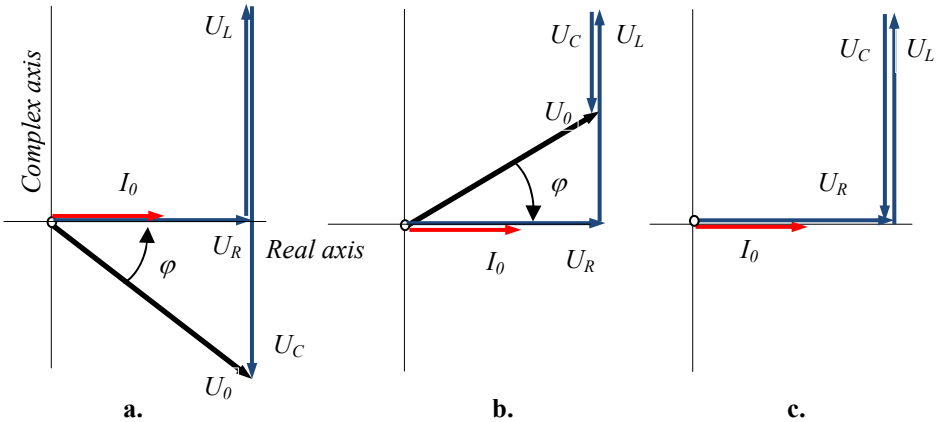


**Figure 5.**

### 1.5. Active and reactive electrical power in the RLC circuit AC

The actual value of a harmonic magnitude *x(t)* is:

$$x_{ef} = \sqrt{\frac{1}{T}\int_0^T x_0 \cdot \cos(\omega t) \cdot dt} = \frac{\sqrt{2}}{2} x_0 \quad (30)$$

The complex instantaneous power is the product of the complex effective voltage $u_{0ef}$ and the complex effective intensity $i_{ef}$:

$$N_{inst} = \frac{\sqrt{2}}{2} u_0 \cdot \frac{\sqrt{2}}{2} i_0$$
$$N_{inst} = \frac{1}{2} U_0 \cdot I_0 \cdot (\cos\varphi + j \cdot \sin\varphi) \quad (31)$$

The complex instantaneous power is represented in the complex plane by a phasor $N_0$ that makes the angle $\varphi$ with the real axis (Figure 6):

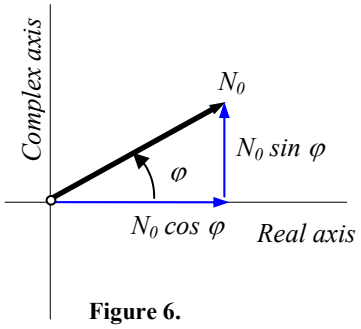


**Figure 6.**

The real power component of the instantaneous power (31) corresponding to the resistive element is called active electrical power:

$$N_{act} = \frac{1}{2} U_0 \cdot I_0 \cdot \cos\varphi$$
$$N_{act} = \frac{1}{2} \frac{U_0 \cdot I_0 \cdot R}{\sqrt{(X_L - X_C)^2 + R^2}} \quad (32)$$

The complex component of the instantaneous power (31) corresponding to the capacitive and inductive

$$N_{react} = \frac{1}{2} U_0 \cdot I_0 \cdot \sin\varphi$$
$$N_{react} = \frac{1}{2} \frac{U_0 \cdot I_0 \cdot (X_C - X_L)}{\sqrt{(X_L - X_C)^2 + R^2}} \quad (33)$$

In Table 1 we can see the direct analogy between the mechanical and electrical quantities corresponding to the mechanical vibrations

**Table 1.**

| VOIGT KELVIN Vibration Differential Vibration Equation/ complex solution | | Differential Equation of electromagnetic oscillations in the RLC circuit AC series/ complex solution |
|---|---|---|
| $m \cdot \ddot{x}(t) + c \cdot \dot{x}(t) + k \cdot x(t) = F_0 \cdot \cos(\omega t)$ | | $L \cdot \ddot{Q}(t) + R \cdot \dot{Q}(t) + \frac{1}{C} Q(t) = U_0 \cdot \cos(\omega t)$ |
| $m \cdot \ddot{z}(t) + c \cdot \dot{z}(t) + k \cdot z(t) = F_0 \cdot e^{j \cdot \omega t}$ | | $L \cdot \ddot{q}(t) + R \cdot \dot{q}(t) + \frac{1}{C} q(t) = U_0 \cdot e^{j \cdot \omega t}$ |
| $z(t) = \frac{F_0 \cdot e^{j\omega t}}{\left(k - m \cdot \omega^2\right) + j \cdot \omega \cdot c}$ | | $q(t) = \frac{U_0 \cdot e^{j\omega t}}{\left(\frac{1}{C} - L \cdot \omega^2\right) + j \cdot \omega \cdot R}$ |
| The excitation harmonic force : $F(t) = F_0 \cdot \cos(\omega t)$ | | The electrical supply voltage: $U(t) = U_0 \cdot \cos(\omega t)$ |
| The complex displacement: $z(t)$ | | The complex charge: $q(t)$ |
| The mass: $m$ | | The inductance of coil: $L$ |
| The damping coefficient: $c$ | | The resistance of resistive element: $R$ |
| The stiffness of elastic element: $1/k$ | | The capacitance of capacitive element: C |
| The impedance of mass: $Z_m = j\omega \cdot m$ | | The impedance of coil: $Z_L = j \cdot L\omega$ |
| The impedance of damping element: $Z_c = c$ | | The impedance of resistance element: $Z_R = R$ |
| The impedance of elastic element: $Z_k = -j \cdot \frac{k}{\omega}$ | | The impedance of capacitive element: $Z_L = -j \cdot \frac{1}{C\omega}$ |
| The complex displacement : $z(t) = \frac{F_0 \cdot e^{j\omega t}}{\left(k - m \cdot \omega^2\right) + j \cdot \omega \cdot c}$ | | The complex electric charge: $q(t) = \frac{U_0 \cdot e^{j\omega t}}{\left(\frac{1}{C} - L \cdot \omega^2\right) + j \cdot \omega \cdot R}$ |
| The complex velocity: $v(t) = \frac{dz(t)}{dt} = \frac{F_0}{c + j\left(m \cdot \omega - \frac{k}{\omega}\right)} \cdot e^{j\omega t}$ | | The complex electric intensity: $i(t) = \frac{dq(t)}{dt} = \frac{U_0 \cdot e^{j\omega t}}{R + j\left(L \cdot \omega - \frac{1}{C \cdot \omega}\right)}$ |

| | | |
|---|---|---|
| The complex acceleration: $a(t)=\frac{dv(t)}{dt}=\frac{F_0}{\left(m-\frac{k}{\omega^2}\right)-j\frac{c}{\omega}}\cdot e^{j\omega t}$ | | The complex electric voltage: $\frac{u_L(t)}{L}=\frac{di(t)}{dt}=\frac{U_0\cdot e^{j\omega t}}{\left(L-\frac{1}{C\cdot\omega^2}\right)-j\frac{R}{\omega}}$ |
| The impedance of mechanical systems with VOIGT KELVIN damping : $Z=c+j\left(m\cdot\omega-\frac{k}{\omega}\right)$ | | The impedance of RLC circuit AC series: $Z=R+j\left(L\cdot\omega-\frac{1}{C\cdot\omega}\right)$ |
| The impedance size of mechanical systems with VOIGT KELVIN damping : $\lvert Z\rvert=\sqrt{c^2+\left(m\cdot\omega-\frac{k}{\omega}\right)^2}$ | | The impedance size of RLC circuit AC series: $\lvert Z\rvert=\sqrt{R^2+\left(L\cdot\omega-\frac{1}{C\cdot\omega}\right)^2}$ |
| The phase between the velocity and the force of the excitation: $tan\varphi=\frac{\frac{k}{\omega}-m\cdot\omega}{c}$ | | The phase between the intensity and the voltage AC supply: $tan\varphi=\frac{\frac{1}{C\cdot\omega}-L\cdot\omega}{R}$ |
| The real and complex component of instantaneous complex mechanical power: $N_{act}=\frac{1}{2}F_0\cdot v_0\cdot cos\varphi$ $N_{react}=\frac{1}{2}F_0\cdot v_0\cdot sin\varphi$ | | The real and complex component of instantaneous complex electrical power: $N_{act}=\frac{1}{2}U_0\cdot I_0\cdot cos\varphi$ $N_{react}=\frac{1}{2}U_0\cdot I_0\cdot sin\varphi$ |

### 1.6. Conclusion to direct analogy

The direct analogy between the mechanical phenomena of vibrations of the elastic mechanical system VOIGT KELVIN and the electromagnetic field oscillations in the RLC series AC refers to the connection between:

- the complex body displacement and complex electrical charge in the capacitor plates,
- the complex body velocity and complex resistor intensity,
- the complex body acceleration and complex electrical voltage in the coil,
- the mechanical impedance of the mass and the electrical impedance of the coil,
- the mechanical impedance of the damper and the electrical impedance of the resistor,
- the mechanical impedance of the spring and the electrical impedance of the capacitor,
- the mechanical impedance of the VOIGT KELVIN system and the electric impedance of the RLC series electric circuit,
- the phase between the velocity and the excitation force, the phase shift between the electrical and voltage,
- the active and reactive mechanical power and active and reactive electrical power.

## 2. REVERSE ANALOGY

### 2.1. General relationships of intensity and voltage in the RLC parallel AC circuits

The RLC parallel AC circuit contain resistive element, capacitive element (capacitor) and inductive element (coil) connected in parallel, being powered by a voltage source $U_0\cdot cos(\omega t)$ (Figure 7).

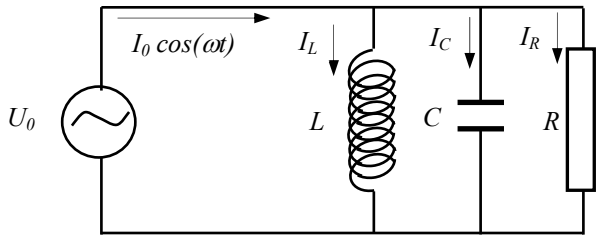


**Figure 7.**

Take into account the existing relationships between the current voltage $U(t)$ and the current intensity for the three elements above, according to first Kirchhoff's theorem the following relation can be written:

$$I_R(t)+I_L(t)+I_C(t)=I(t) \qquad (34)$$

$$U(t)=R\cdot I_R(t) \qquad \Rightarrow I_R(t)=\frac{U(t)}{R}$$

$$U(t)=L\cdot\frac{dI_L(t)}{dt} \qquad \Rightarrow I_L(t)=\frac{1}{L}\cdot\int U(t)dt \qquad (35)$$

$$U(t)=\frac{1}{C}\cdot\int I_C(t)dt \quad \Rightarrow I_C(t)=C\cdot\frac{dU(t)}{dt}$$

$$\frac{U(t)}{R}+\frac{1}{L}\cdot\int U(t)dt+C\frac{dU(t)}{dt}=I(t) \qquad (36)$$

We obtain the differential voltage relationship according to the intensity *I(t)* in the parallel AC RLC circuit. If derivate the differential equation (36) the differential equation of voltage U(t) is obtained:

$$C\cdot\ddot{U}(t)+\frac{1}{R}\dot{U}(t)+\frac{1}{L}U(t)=\frac{dI}{dt} \qquad (37)$$

### 2.2. The complex calculus of current and voltage voltages of the RLC parallel AC circuit

Using the complex calculation, the differential equation of the electric voltage (37) is written:

$$i(t)=I_0\cdot e^{j\omega t} \qquad (38)$$

$$C\cdot\ddot{u}(t)+\frac{1}{R}\dot{u}(t)+\frac{1}{L}u(t)=I_0\cdot j\omega\cdot e^{j\omega t} \qquad (39)$$

where $u(t)=u_0\cdot e^{j\omega t}$ (40)

Replacing complex electrical voltage derivatives:

$$\dot{u}(t)=u_0\cdot j\omega\cdot e^{j\omega t};$$
$$\ddot{u}(t)=-u_0\cdot\omega^2\cdot e^{j\omega t} \qquad (41)$$

in equation (39), the complex amplitude of the electrical voltage is immediately obtained:

$$u(t)=\frac{I_0\cdot e^{j\omega t}}{A}=U_0\cdot e^{j(\omega t-\varphi)} \qquad (42)$$

where *A* is electrical admittance:

$$A=\frac{1}{R}+j\left(C\cdot\omega-\frac{1}{L\cdot\omega}\right) \qquad (43)$$

$$U_0=\frac{I_0}{|A|};\ |A|=\sqrt{\frac{1}{R^2}+\left(C\cdot\omega-\frac{1}{L\cdot\omega}\right)^2}; \qquad (44)$$

$$tan\varphi=\frac{C\cdot\omega-\frac{1}{L\cdot\omega}}{\frac{1}{R}};$$

The real solution to the differential equation (37) is:

$$U(t)=U_0\cdot cos(\omega t-\varphi) \qquad (45)$$

The size of electrical admittance *A* and phase between voltage and current can also be written:

$$|A|=\sqrt{\frac{1}{R^2}+\left(\frac{1}{X_C}-\frac{1}{X_L}\right)^2} \qquad (46)$$

$$tan\varphi=\frac{\frac{1}{X_C}-\frac{1}{X_L}}{\frac{1}{R}} \qquad (47)$$

Where the *electrical* admittance of capacitive and inductive element are:

$$\frac{1}{X_C}=C\cdot\omega \qquad (48)$$

$$\frac{1}{X_L}=\frac{1}{L\cdot\omega} \qquad (49)$$

### 2.3. Phasor representation of current and voltages in the RLC series AC circuit

*a) the complex intensity* $i(t)=I_0\cdot e^{j\omega t}$ is represented in the complex plane by a phasor $I_0$ rotating in the trigonometric sense with the angular velocity $\omega$. At moment t the phasor $I_0$ makes the angle $\omega t$ with the real axis; the real intensity $I_0\cdot cos\omega t$ represents the projection of the phasor $I_0$ on the real axis and the complex intensity $j\cdot I_0\cdot sin\omega t$ the projection on the imaginary axis (Figure 8).

The expression of the complex intensity $u_0(t)$ is:

$$i_0(t)=I_0\cdot cos(\omega t)+j\cdot I_0\cdot sin(\omega t)$$
$$i_0(t)=I_0\cdot e^{j\omega t} \qquad (50)$$

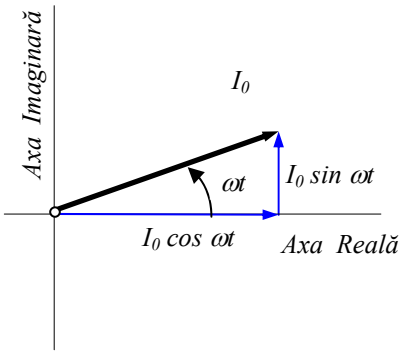


**Figure 8.**

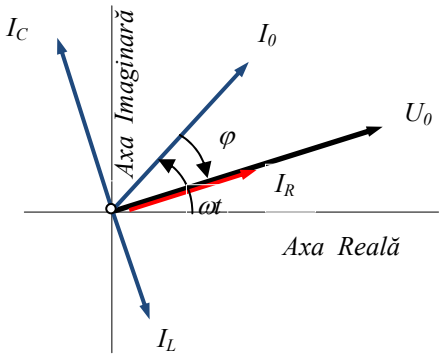


**Figure 9.**

*b) the complex voltage u(t)* given by the relation (42) is represented in the complex plane by a phasor $U_0$ which rotates with the phasor $I_0$ in the trigonometric sense with the same angular velocity $\omega$, being phased behind of the phasor $I_0$ with the angle $\varphi$ (Figure 9).

The complex voltage amplitude $u_0$ results from the first Kirchhoff's theorem (34) written in the complex:

$$\frac{u_0 \cdot e^{j\omega t}}{R} + \frac{1}{L} \cdot \frac{u_0 \cdot e^{j\omega t}}{j\omega} + C \cdot u_0 \cdot j\omega \cdot e^{j\omega t} = I_0 \cdot e^{j\cdot\omega t}$$
$$\Rightarrow u_0 = \frac{I_0}{A}; \quad unde: \quad A = \frac{1}{R} + j\left(C \cdot \omega - \frac{1}{L \cdot \omega}\right) \tag{51}$$

The complex voltage *u(t)* can be written:

$$u(t) = U_0 \cdot e^{j(\omega t - \varphi)} \tag{52}$$

where:

$$U_0 = \frac{I_0}{|A|}; \quad |A| = \sqrt{\frac{1}{R^2} + \left(\frac{1}{X_C} - \frac{1}{X_L}\right)^2} \tag{53}$$

$$tan\varphi = \frac{\frac{1}{X_C} - \frac{1}{X_L}}{\frac{1}{R}} \tag{54}$$

*c. the complexity intensity through the resistor $i_R(t)$* is the ratio between the complex voltage *u(t)* and the resistance $R$ and is represented in the complex plane by an $I_R$ phasor which rotates with the phases $U_0$ and $I_0$ at the same angular velocity $\omega$ being in phase with the phasor $I_0$ (Figure 9):

$$i_R(t) = \frac{u(t)}{R}$$
$$i_R(t) = \frac{U_0}{R} \cdot e^{j(\omega t - \varphi)} \tag{55}$$

*d. The complex intensity of the capacitor $i_C(t)$* is the product of the complex voltage derivative and the capacity of the capacitor $C$ ; they is represented in the complex plane by a phasor $I_C$ which rotates with the phases $U_0$ and $I_0$ at the same angular velocity $\omega$ in front of the beam $I_0$ with the angle $\pi/2$ radians (Figure 9):

$$i_C(t) = C \cdot \frac{du(t)}{dt} = C \cdot U_0 \cdot j \cdot \omega \cdot e^{j(\omega t - \varphi)}$$
$$i_C(t) = C \cdot U_0 \cdot \omega \cdot e^{j\left(\omega t - \varphi + \frac{\pi}{2}\right)} \tag{56}$$

*e) the complex intensity through the coil $i_L(t)$* is the ratio between the integral of the complex voltage *u(t)* and the inductance $L$ of the coil, and is represented in the complex plane by a phasor $I_L$ which rotates with the phases $U_0$ and $I_0$ at the same angular velocity $\omega$, being phased behind the phasor $I_0$ with the angle $\pi/2$ radians (Figure 9):

$$i_L(t) = \frac{1}{L} \cdot \int u(t)dt = \frac{U_0}{L \cdot j\omega} \cdot e^{j(\omega t - \varphi)}$$
$$i_L(t) = \frac{U_0}{L \cdot \omega} \cdot e^{j\left(\omega t - \varphi - \frac{\pi}{2}\right)} \tag{57}$$

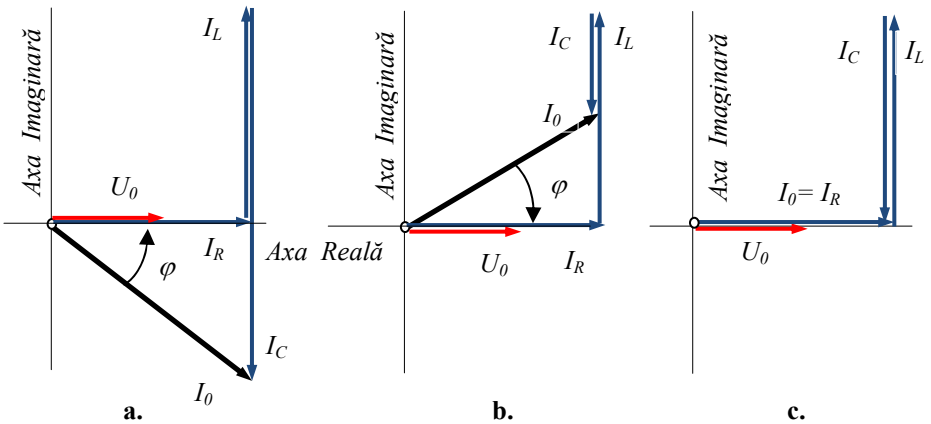


**Figure 10.**

### 2.4. The electrical admittance of the RLC parallel AC circuit

In the case of the RLC parallel, the electric admitance *A*, is equal to the ratio between the complex intensity *i(t)* and the complex supply voltage $u_0(t)$ (51):

$$A = \frac{1}{R} + j\left(C\cdot\omega - \frac{1}{L\cdot\omega}\right) \tag{58}$$

The study of electromagnetic oscillations in the RLC parallel circuit AC with the electric admittance *A* allows a voltage analysis and they is based on:

- the resistive admittance according to the relation (55) is a constant number, which does not depend on the frequency of the current:

$$A_R = \frac{i_R(t)}{u(t)} = \frac{1}{R} \tag{59}$$

- the capacitive admittance according to the relation (56) is a complex number that depends directly on the frequency of the supply voltage:

$$A_C = \frac{i_C(t)}{u(t)} = j\cdot C\cdot\omega = \frac{j}{X_C} \tag{60}$$

- the inductive admittance according to the relation (57) is a complex number that depends inversely proportional to the frequency of the supply voltage:

$$A_L = \frac{i_L(t)}{u(t)} = \frac{1}{j\cdot L\cdot\omega} = -\frac{j}{X_L} \tag{61}$$

The electrical admittance of the parallel RLC circuit is calculated by the sum of the admittances of the three elements, because the complex relation of the intensities can be written:

$$\begin{aligned} &i_L(t) + i_R(t) + i_C(t) = i(t) \\ &\Rightarrow A_L\cdot u(t) + A_R\cdot u(t) + A_C\cdot u(t) = A\cdot u(t) \\ &\Rightarrow A = A_L + A_L + A_L \end{aligned} \tag{62}$$

$$\Rightarrow A = \frac{1}{R} + j\left(C\cdot\omega - \frac{1}{L\cdot\omega}\right)$$

$$\Rightarrow A = \frac{1}{R} + j\left(\frac{1}{X_C} - \frac{1}{X_L}\right);$$

$$|A| = \sqrt{\frac{1}{R^2} + \left(\frac{1}{X_C} - \frac{1}{X_L}\right)^2} \tag{63}$$

If the phasors $I_L$ , $I_C$ , $U_R$ and $I_0$ are represented so that $I_0$ and $U_R$ are in phase and coincide with the real axis, is obtained figure 10, which shows:

- for $I_L < I_C$ (Fig. 10.a), the current I0 is offset in front of the supply voltage U0 with the angle $\varphi$ and we say that we have a capacitive parallel RLC circuit;
- for $I_L > I_C$ (Figure 10.b), the current I0 is broken down from the supply voltage $U_0$ with the angle $\varphi$ and we say that we have an inductive parallel RLC circuit;
- for $I_L = I_C$ (Figure 10c), the current $I_0$ is in phase with the supply voltage U0 is equal to the current in the IR resistor and we say that the circuit is resonant. The condition for achieving the resonance is imposed by the equality $A_L = A_C$:

$$C\cdot\omega = \frac{1}{L\cdot\omega} \Rightarrow \omega_r = \frac{1}{\sqrt{L\cdot C}} \tag{64}$$

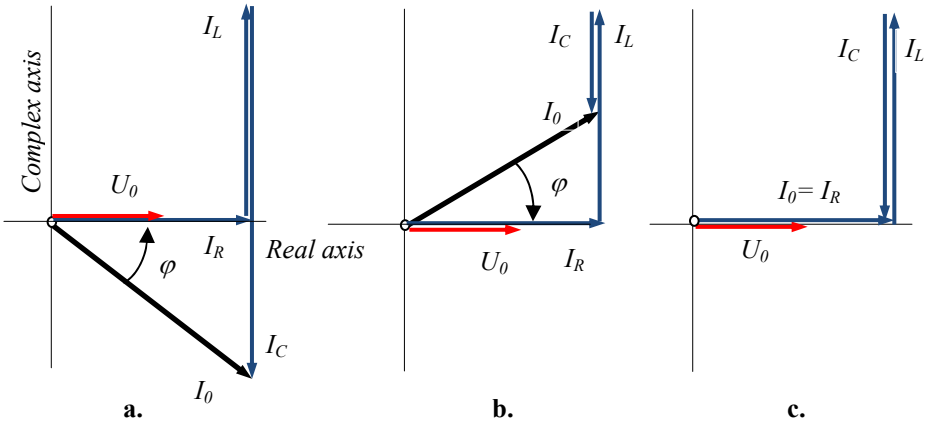


**Figure 11.**

### 2.5. Active and reactive electrical power in the RLC parallel circuit AC

The complex instantaneous power is the product of the complex effective voltage $u_{0ef}$ and the complex effective intensity $i_{ef}$:

$$N_{inst} = \frac{\sqrt{2}}{2} u_0 \cdot \frac{\sqrt{2}}{2} i_0$$
$$N_{inst} = \frac{1}{2} U_0 \cdot I_0 \cdot (\cos\varphi + j \cdot \sin\varphi) \quad (65)$$

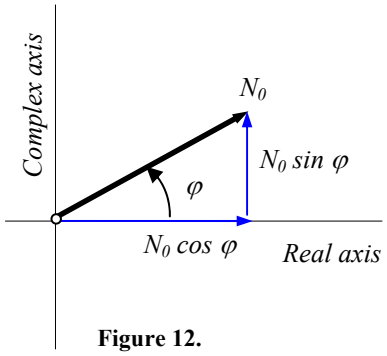


**Figure 12.**

The complex instantaneous power is represented in the complex plane by a phasor $N_0$ that makes the angle $\varphi$ with the real axis (Figure 12).

The real power component of the instantaneous power (65) corresponding to the resistive element is called active electrical power:

$$N_{act} = \frac{1}{2} U_0 \cdot I_0 \cdot \cos\varphi$$
$$N_{act} = \frac{1}{2} U_0 \cdot I_0 \cdot \frac{\frac{1}{R}}{|A|}; \quad (66)$$
$$|A| = \sqrt{\frac{1}{R^2} + \left(\frac{1}{X_C} - \frac{1}{X_L}\right)^2}$$

The complex component of the instantaneous power (65) corresponding to the capacitive and inductive

$$N_{react} = \frac{1}{2} U_0 \cdot I_0 \cdot \sin\varphi$$
$$N_{react} = \frac{1}{2} U_0 \cdot I_0 \cdot \frac{\frac{1}{X_C} \frac{1}{X_L}}{|A|}; \quad (67)$$
$$|A| = \sqrt{\frac{1}{R^2} + \left(\frac{1}{X_C} - \frac{1}{X_L}\right)^2}$$

Table 2 shows the inverse analogy between mechanical and electrical quantities corresponding to mechanical vibrations and electromagnetic oscillations in parallel RLC circuit AC.

**Table 2.**

| VOIGT KELVIN Vibration Differential Vibration Equation/ complex solution | | Differential Equation of electromagnetic oscillations in the RLC circuit AC series/ complex solution |
|---|---|---|
| $m \cdot \ddot{x}(t) + c \cdot \dot{x}(t) + k \cdot x(t) = F_0 \cdot \cos(\omega t)$ | | $C \cdot \ddot{U}(t) + \frac{1}{R}\dot{U}(t) + \frac{1}{L}U(t) = -I_0 \cdot \omega \cdot \sin(\omega t)$ |
| $m \cdot \ddot{z}(t) + c \cdot \dot{z}(t) + k \cdot z(t) = F_0 \cdot e^{j\omega t}$ | | $C \cdot \ddot{u}(t) + \frac{1}{R}\dot{u}(t) + \frac{1}{L}u(t) = I_0 \cdot j\omega \cdot e^{j\omega t}$ |
| $v(t) = \frac{dz(t)}{dt} = \frac{F_0 \cdot e^{j\omega t}}{c + j\left(\omega \cdot m - \frac{k}{\omega}\right)}$ | | $u(t) = \frac{I_0 \cdot e^{j\omega t}}{\frac{1}{R} + j\left(C \cdot \omega - \frac{1}{\omega \cdot L}\right)}$ |
| The excitation harmonic force: $F(t) = F_0 \cdot \cos(\omega t)$ | | The electrical intensity derivative: $\frac{dI(t)}{dt}$ |
| The complex displacement: $z(t)$ | | The complex voltage: $u(t)$ |
| The mass: $m$ | | The capacitance of capacitive element: $C$ |
| The damping coefficient: $c$ | | The resistance of resistive element: $1/R$ |
| The reverse of stiffness element: $1/k$ | | The inductance of coil: $L$ |
| The impedance of mass: | | The admittance of capacitive element: |

| | | |
|---|---|---|
| $Z_m = j\omega \cdot m$ | | $A_L = \frac{1}{Z_L} = j \cdot C \cdot \omega$ |
| The impedance of damping element: $Z_c = c$ | | The admittance of resistive element: $A_R = \frac{1}{R}$ |
| The impedance of elastic element: $Z_k = -j \cdot \frac{k}{\omega}$ | | The admittance of coil: $A_L = \frac{1}{Z_L} = -j \cdot \frac{1}{L \cdot \omega}$ |
| The complex displacement : $z(t) = \frac{F_0 \cdot e^{j\omega t}}{\left(k - m\omega^2\right) + j \cdot c\omega}$ | | The complex electric intensity: $L \cdot i_L(t) = \int u(t)dt = \frac{I_0 \cdot e^{j\omega t}}{\left(\frac{1}{L} - C \cdot \omega^2\right) + \frac{j\omega}{R}}$ |
| The complex velocity: $v(t) = \frac{dz(t)}{dt} = \frac{F_0 \cdot e^{j\omega t}}{c + j\left(\omega \cdot m - \frac{k}{\omega}\right)}$ | | The complex electric voltage: $u(t) = \frac{I_0 \cdot e^{j\omega t}}{\frac{1}{R} + j\left(C \cdot \omega - \frac{1}{\omega L}\right)}$ |
| The complex acceleration: $a(t) = \frac{dv(t)}{dt} = \frac{F_0 \cdot e^{j\omega t}}{\left(m - \frac{k}{\omega^2}\right) - j\frac{c}{\omega}}$ | | The complex electric intensity: $\frac{i_C(t)}{C} = \frac{du(t)}{dt} = \frac{I_0 \cdot e^{j\omega t}}{\left(C - \frac{1}{\omega^2 \cdot L}\right) - \frac{j}{R \cdot \omega}}$ |
| The impedance of mechanical systems with VOIGT KELVIN damping : $Z = c + j\left(\omega \cdot m - \frac{k}{\omega}\right)$ | | The admittance of RLC circuit AC parallel: $A = \frac{1}{R} + j\left(C \cdot \omega - \frac{1}{L \cdot \omega}\right)$ |
| The impedance size of mechanical systems with VOIGT KELVIN damping : $\lvert Z \rvert = \sqrt{c^2 + \left(m \cdot \omega - \frac{k}{\omega}\right)^2}$ | | The admittance size of RLC circuit AC parallel: $\lvert A \rvert = \sqrt{\frac{1}{R^2} + \left(C \cdot \omega - \frac{1}{L \cdot \omega}\right)^2}$ |
| The phase between the velocity and the force of the excitation: $tan\varphi = \frac{\omega \cdot m - \frac{k}{\omega}}{c}$ | | The phase between the intensity and the voltage AC supply: $tan\varphi = \frac{C \cdot \omega - \frac{1}{L \cdot \omega}}{\frac{1}{R}}$ |
| The real and complex component of instantaneous complex mechanical power: $N_{act} = \frac{1}{2} F_0 \cdot v_0 \cdot cos\varphi$ $N_{react} = \frac{1}{2} F_0 \cdot v_0 \cdot sin\varphi$ | | The real and complex component of instantaneous complex electrical power: $N_{act} = \frac{1}{2} U_0 \cdot I_0 \cdot cos\varphi$ $N_{react} = \frac{1}{2} U_0 \cdot I_0 \cdot sin\varphi$ |

**2.6. Conclusion to reverse analogy**

The reverse analogy between the mechanical phenomena of vibrations of the elastic mechanical system VOIGT KELVIN and the electromagnetic field oscillations in the RLC parallel AC circuit refers to the connection between:

- the complex body displacement and complex electrical intensity in the coil,
- the complex body velocity and complex voltage supply,
- the complex body acceleration and complex intensity of capacitive element,
- the mechanical impedance of the mass and the electrical admittance of capacitive element,
- the mechanical impedance of the damper and the electrical admittance of resistor,

- the mechanical impedance of the spring and the electrical admittance of coil,
-
- the mechanical impedance of the VOIGT KELVIN system and the electric admittance of the RLC parallel electric circuit,
- the phase between the velocity and the excitation force, the phase between the electrical and voltage,
- the active and reactive mechanical power and active and reactive electrical power.

Direct analogue circuit RLC series AC circuits and reverse analogue RLC parallel AC circuits refers to the connection between complex speed and complex voltage, between mechanical impedance and electrical admission.

## REFERENCES


[1] Bratu, P.P. - IZOLAREA ŞI AMORTIZAREA VIBRAŢIILOR LA UTILAJE DE CONSTRUCŢII. Editura INCERC, Bucureşti 1982

[2] Buzdugan, Gh. Fetcu, L. Radeş, M.– VIBRAŢII MECANICE. Ed. Did. şi Pedagogică Bucureşti, 1982

[3] Bratu, P.P., Drăgan, D. - VIBRAŢIILE MECANICE. TEORIE. APLICAŢII TEHNICE. Editura Impuls, Bucureşti, 1998

[4] Bratu, P.P., Drăgan, D. - VIBRAŢIILE MECANICE.. APLICAŢII. Editura Impuls, Bucureşti, 1998

[5] Bratu, P. P. - VIBRAŢIILE STRUCTURILOR MECANICE. Editura Tehnică, 2000

[6] Voinea, R., Bratosin, D. – ELEMENTE DE MECANICA MEDIILOR CONTINUE. Editura EX PONTO, Constanţa, 2000.

[7] Silaș, Gh., Rădoi, M. s.a. – Culegere de probleme de vibrații mecanice, vol.1, Editura Tehnică București, 1967

[8] Cornel Marin, Ion Florin Popa – CONTROLUL VIBRAŢIILOR ȘI DIAGNOZA VIBVROACUSTICĂ A SISTEMELOR MECANICE, Editura Valahia University Press, 2018, ISBN 978-606-603-194-3

[9] Cornel Marin - VIBRAŢIILE STRUCTURILOR MECANICE - Editura IMPULS Bucureşti, 2003, ISBN 973-8132-43-6.

[10] Cornel MARIN - VIBRAŢII MECANICE. APLICAŢII. PROBLEME, Editura Bibliotheca Târgovişte, 2008, ISBN 978-973-712-397-8

[11] Cornel MARIN, Polidor BRATU , RESEARCH TRENDS IN MECHANICS, Vol. III Chapter 11: DYNAMICAL BEHAVIOUR OF THE STRUCTURES SUBJECTED TO MECHANICAL SHOCKS, Editura Academiei Române, Bucureşti 2009, ISBN 978-973-27-1816-2

[12] Gheorghe ENE, Cornel MARIN CALCULUL ŞI CONSTRUCTIA MAŞINILOR VIBRATOARE, Editura PRINTECH, Bucureşti, 2009 ISBN 978-606-521-429-3

[13] Cornel MARIN, Popa Florin, Ardeleanu Mihăiţă - Expression of energy in the case of forced vibrations with elasto – viscous damping. Determination damping factor of elasto – viscous shells - OPROTEH 2003 - Optimum Technologies, Technologic Systems and Materials in the Machines Building Field TSTM –9, Bacău 2003, p. 142-147

[14] Cornel MARIN, Florin Popa, Mihăiţă Ardeleanu - Expression of average, instantaneous, real and reactive power in case of forced vibrations with elastic-viscous damping. Influence of damping factor on real and reactive power - OPROTEH 2003 - Optimum Technologies, Technologic Systems and Materials in the Machines Building Field TSTM –9 , Bacău 2003, p. 148-153.

[15] Cornel MARIN, Popa Ion Florin, Ardeleanu Mihăiţă - Some practical aspects regarding passive ant vibration isolation using elasto-viscous damping covers – In Annals of the ORADEA UNIVERSITY, Fascicle of Management and Technological Engineering CD-ROM Edition Vol. II (XII) 2003, ISSN 1583-0691, p. 18-19.

[16] Cornel MARIN, Florin Popa - The simulation of flood and relaxation of materials using VOIGT-KELVIN visco-elastic model Al III lea Simpozion Internaţional „Mecatronică, Microtehnologii şi materiale noi" Targoviste 18 -19 noiembrie 2005, Supliment la Rev. Română de Mecanică Fină, Optică şi Mecatronică, Nr. 28/2005, pp.107-116.

[17] Cornel MARIN, Florin Popa - Simularea comportării în regim armonic a elementelor de izolare antivibratilă a maşinilor folosind modelele vâscoelastice VOIGT-KELVIN şi ZENER. Simpozionul ştiinţific cu participare internaţională de Mecanică Fină şi Mecatronică: „Produse/Tehnologii şi Servicii româneşti competitive şi complementare pentru U.E." Bucureşti 28-29 .11. 2005.

The Scientific Bulletin of VALAHIA University
MATERIALS and MECHANICS –Vol. 17, No. 16

DOI 10.2478/bsmm-2019-0010

# ADDITIVE MANUFACTURING AS AN IMPORTANT INDUSTRY PLAYER FOR THE NEXT DECADES

**Nastase-Dan CIOBOTA[1*], Gheorghe Ion GHEORGHE[2], Veronica DESPA[2]**

[1] National Institute of Research and Development in Mechatronics and Measurement Technique (INCDMTM), 6-8 Sos. Pantelimon, Bucharest

[2]Valahia University of Targoviste, Faculty of Materials Engineering and Mechanics, 13 Aleea Sinaia Street,Targoviste, Romania

E-mail:* dan_ciobota@yahoo.com

**Abstract:** *Additive Manufacturing (AM) concerns all classes of materials – polymers, metals, ceramics and glasses as well. For this reason, AM is in the focus of material scientists from all branches. Leaders of the industry realize that the possibilities of 3D printing are endless, and that these possibilities need ways and means to be taken full advantage of. Today, aerospace engineers are using the fused deposition modeling (FDM) method for rapid prototyping, part manufacturing, and tooling. They are followed by leaders and engineers from industry (industrial machines, motor vehicles, consumer products, medical/dental) but also from academic institutions and government/military.*

**Keywords:** *Additive Manufacturing (AM), 3D printing*

## 1. INTRODUCTION

3D geometry parametric design of osteo-articular joints, mechanical parameters design and analysis, FEM – Finite Element Method Analysis, computer-assisted design and quantitative/quality analysis of functional prototypes, with wide applicability in cranio-maxillo-facial aesthetic surgery, neurosurgery and transdisciplinary domains such as aerospace, innovative materials, products and processes, information technology and communications, biotechnology and textiles.

The human body has a highly complex geometry and its aesthetic plays an important role in social integration. Customized implants, which take into account the individuality of every person, are highly demanded on the market, tending to replace the standard implants, and most of them are very aesthetic. These new approaches will coordinate the research work to produce such implants via Additive Manufacturing technologies, which can be used in a wide range of surgical specialties, like orthopedics, neurosurgery, cranio-maxillo-facial surgery, orthopedy-traumatology, external ortheses (various surgical corsets, hearing aids, parts of exoskeleton), etc.

AM is very important for external orthopedics (orthesis) in contact with the body. It allows to involve a wider choice of materials than these only validated for implants.

The industry focus now change, from substractive technologies to additive technologies, which mean eco-friendly designed machines, with a lot of electronics embedded, and ready for the Industry 4.0 revolution. They are followed by leaders and engineers from industry (industrial machines, motor vehicles, consumer products, medical/dental) but also from academic institutions and government/military.

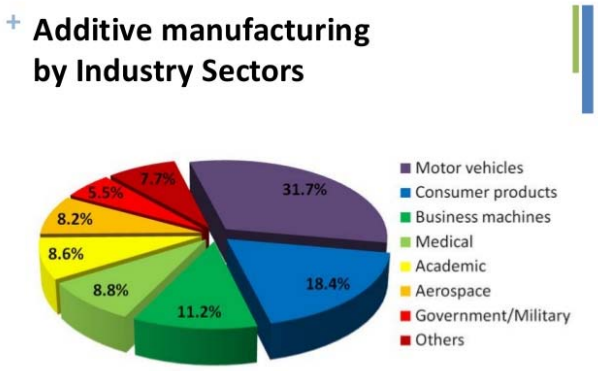


**Figure 1. Additive manufacturing by Industry Sectors (%)**

All the parts designed in CAD can be produced in short time, with less man power, and in an automatic way. The complexity isn't an issue any more, even very complex design can be created with a very high precision and accuracy. [1]

Additive Manufacturing empower the creativity of the engineers, being the right tool to bring to life new concepts, functional assemblies, ready to be tested in a real-world scenario

## 2. RELEVANCE AND TIMELINESS

The approached research area is one of the most exciting research areas at international level.
The list below provides only a few of the top domain level users of the e-Manufacturing technologies: NASA - National Aeronautics and Space Administration, Boeing, ESA – European Space Agency, Toyota, Ford, Cambridge University, MIT University, Materialise NV, DuPont, Zimmer and many others.
Every single top technology entity is starting to use this technology, and most importantly, the aforementioned top domain level users come from a wide range of economic sectors. [2]

Since the emerging of the Additive Manufacturing technologies, they evolved rapidly, fast-paced and continuously adapting to market demands. Thus, a promising new era of digital environment arise.
Tightly related to the manufacturing which is digitally connected now, also known as "Industry 4.0", they encompass a large variety of technologies, ranging from 3D printing to bioprinting, new materials development and enhanced production systems.
In the European Parliament, one of the largest legislative body in the world, there are meetings debating the future influence of the Additive Manufacturing and 3D Printing. According to the conclusions of these meetings, it is a must for european leaders and industry factors, together with academia and research to develop and advance additive manufacturing technologies and to implement them in SMEs. [3]

It is necessary to have a common strategy, combined with the involvement of all stakeholders, to create critical mass of specialists, researchers, technology and knowledge to create the impetus necessary for the healthy development of this fieldAdvanced technologies for manufacturing , which include additive manufacturing and 3D printing, are becoming globally recognized as a force to be reckoned with, presenting the potential to reduce supply chain cost, increase sustainability (by saving materials and energy waste), and fundamentally alter how we produce both commercial and industrial goods.
Recognizing this, Europe has proven to be a leader in certain AM-related fields, including metal 3D printing. However, if Europe wants to remain competitive—particularly since regions like USA, China, and Japan rapidly advance—it must establish a unified, comprehensive strategy to ensure "steady, long-lasting, and consistent development" of 3D printing technology within its borders.

**Figure 2. Additive Manufacturing Could Disrupt A Lot of Aerospace Markets**

There are many opinions that over the next decades 3D will virtually be able to print anything at a very low cost and in less time than would be achieved by conventional technology, some applications of aditive manufacturing being absolutely unbelievable. Obviously, once AM technology evolves and becomes mature, as in the case of robotics development, there will be major societal changes where the traditional plants in the form we now know will turn into fully automated factories, where the robots will ensure the flow of the production of additive manufactured parts and, why not, even at the level of cosmic space, by placing on the surface of some planets of interest (eg Mars) of such equipment, facilitating less colonization costly and faster way.

## 3. INNOVATION POTENTIAL

AM combines wide-spread methods – and they are still under development.
The state of development is quite different as far as the different classes of materials are considered. In case of polymers and metals, AM has already attained production level, whereas for ceramics, glasses or hard metals the development is right at the beginning. This can be emphasized by the Gartner Hype curve (see Figure 3), where AM for ceramics is at the beginning of the first slope.

**Figure 3. Hype-Cycle-for-Emerging-Tech-2018**

The reason for these differences can be seen in the complexity of the shaping technology of ceramics.

Polymers and metals can be molten either in a nozzle or under exposure to a laser or electron beam. The Electron Beam Technology is already used for the production of complex parts for medical and aerospace applications (Lima Corporate and AvioAero-GE Aviation).
After the AM process, the parts are ready to use or be machined in any way, can be polished and even coated if required. Ceramic technology however also implies powder technology.
For the shaping of ceramic parts, polymers acting as a temporary binder are needed. After shaping, the thermoplastic component has to be burnt out and the ceramic component must be sintered for attaining the final properties. For that reason, a ceramic part made by AM is only a semi-finished component. Another difficulty can be seen in the large variety of ceramic materials – some contain a glassy phase, others are sintered only by solid state sintering processes. Some powders are dark and absorb visible light, others appear to be translucent.
Some powders decompose under a laser beam, others start melting. This is the reason why the ceramic powder makes the rules for its treatment. Many AM technologies, powder- and suspension-based methods, have been developed so far. Each method is suited for a certain group of ceramic materials and allows obtaining certain materials showing peculiar properties, like dense or porous ceramic parts. The layer-wise manufacturing is very challenging for the subsequent debinding and sintering process of ceramic components due to failure or defect initiation.

The advantage of the technology AM is that it can be obtained in experimental models or prototypes of metal with mechanical properties higher weights less and geometries more complex than the same component obtained by the conventional methods, all in a short time and manufacturing cost than especially by eliminating the need for molds, tools and other SDVs. For these reasons, leading companies in the automotive, energy and aerospace already using AM technology for mass production of components, the trend is that in the end can be achieved by AM and critical components or assemblies whole (engine, turbine , etc.) with high performance and in a very short time. For example, in the case of turbines, whether they are used in the energy or aerospace industry, additive manufacturing is the most "hot" research direction in this field. Knowing that the efficiency of the turbomachines is given by the power / weight ratio and operating temperatures, it has been constantly pursued in recent years to improve both the geometry of the components and the materials from which they are manufactured. Besides the appearance of superalloys with nickel base, a step forward in increasing the operating temperatures of turbo engines was the development of cooling passages inside the turbine blades. But this development has stalled in the absence of viable manufacturing methods to replace vacuum precision casting method, which showed certain limitations as design concepts cooling channels have evolved and increasingly sophisticated geometries required. To achieve this goal, "Additive Manufacturing" is the solution, and in this sense, the first results have already emerged worldwide. For example, GE Power (USA) announced that the energy efficiency of its facilities combined cycle increased by 64% using AM that allowed components with complex geometry best, impossible so far by manufacturing methods current GE Aviation manufactured the injectors from the LEAP 1A engine using the AM technology used on the A320 NEO and the examples can continue.

**Figure 4. New manufacturing milestone: 30,000 additive fuel nozzles**

Although there is a particular interest in the development and widespread use of additive manufacturing with metallic materials, this technology still has a number of features that at least for the time being prevents the use of the additive manufactured without further mechanical processing and / or the application of other methods post-processing (thermal treatments, hot isostatic pressing, surface hardening, etc.) in order to reduce the anisotropic character of the materials induced by the manufacturing method.

Maybe the most relevant fact that convinced us that additive manufacturing is the future of manufacturing, is the fact that the most advanced and research-intensive entities from the aerospace area use it. GE Aviation, one of the large integrated manufacturers, uses it extensively. With 3D-printed materials lighter yet stronger parts can be obtained with respect to "traditional" manufacturing techniques.

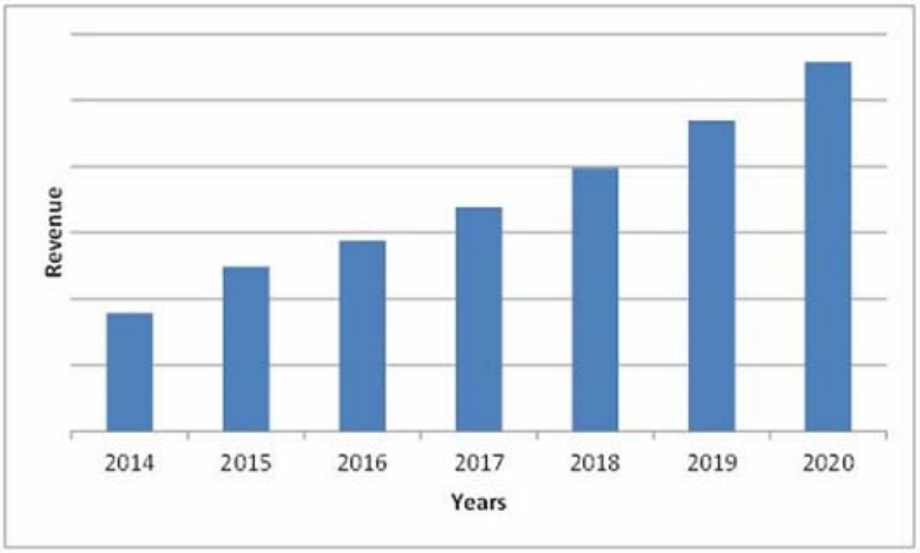


**Figure 5. Additive Manufacturing Revenue by Years – from MarketandMarkets**

## 4. CONCLUSIONS

The AM approach showed advantages over conventional subtractive or formative methods, which are clearly illustrated by the great design freedom that can be achieved, such as the possibility of producing customized geometries or topologically optimized geometries for lightweight components. [5] The effectiveness of the AM process has been largely demonstrated: low production volume if compared with high pressure die casting, improving the supply chain in the reduction of lead time and the total cost, a reduction of the buy-to-fly ratio for the aero engine if compared with machining.

3D printing can be not only used to produce new parts, but also to repair existing parts. [6] Hybrid technologies combining conventional machining and especially directed energy deposition (DED)-type technologies are being intensively studied, especially when related to aerospace and military sectors.

From the materials side, ceramics appear to be an interesting group of materials, especially for harsh environments e.g. with very high temperatures. Ultra-high temperature ceramics (UHTC) such as $ZrB_2$ and ZrC can stand extremely high temperatures (>2000°C) and have a very high potential when thinking of applications like hypersonic flight systems and rocket propulsion systems.

## REFERENCES:

[1] Materials for 3D printing in medicine: Metals, polymers, ceramics, hydrogels - Poologasundarampillai G, Nommeots-Nomm A - 3D Printing in Medicine (2017) pp. 43-71

[2] 3D Systems' Technology Overview and New Applications in Manufacturing, Engineering, Science, and Education - Snyder T, Andrews M, Weislogel M, Moeck P, Stone-Sundberg J, Birkes D, Hoffert M, Lindeman A, Morrill J - 3D Printing and Additive Manufacturing, vol. 1, issue 3 (2014) pp. 169-176

[3] Additive Manufacturing Trends in Aerospace - Joe Hiemenz - Additive Manufacturing (2013) p. 6

[4] Global Engineering and Additive Manufacturing - Bandyopadhyay A, Gualtieri T, Bose S - Additive Manufacturing, vol. 10 (2015) pp. 1-18 Published by CRC Press

[5] Anatomic modeling using 3D printing: quality assurance and optimization - Leng S, McGee K, Morris J, Alexander A, Kuhlmann J, Vrieze T, McCollough C, Matsumoto J - 3D Printing in Medicine, vol. 3, issue 1 (2017) p. 6

[6] 3D printing with biomaterials: Towards a sustainable and circular economy - van Wijk A, van Wijk I - 3D Printing with Biomaterials: Towards a Sustainable and Circular Economy (2015) pp. 1-85 Published by IOS Press